Copyright
by
Pei-Hsin Kuo
2015

The Dissertation Committee for Pei-Hsin Kuo
certifies that this is the approved version of the following dissertation:

Bio-inspired Robotic Joint and Manipulator: from Biomechanical Experimentation and Modeling to Human-like Compliant Finger Design and Control

Committee:

Ashish D. Deshpande, Supervisor

Ronald Barr

Richard Neptune

Raul Longoria

Jonathan Dingwell

Bio-inspired Robotic Joint and Manipulator: from Biomechanical Experimentation and Modeling to Human-like Compliant Finger Design and Control

by

Pei-Hsin Kuo, B.S., M.S.

DISSERTATION

Presented to the Faculty of the Graduate School of

The University of Texas at Austin

in Partial Fulfillment

of the Requirements

for the Degree of

DOCTOR OF PHILOSOPHY

THE UNIVERSITY OF TEXAS AT AUSTIN

May 2015

Acknowledgments

I would like to first thank my advisor, Dr. Ashsih Dehspnde, for his support, guidance, and patience. Dr. Dehspnde has given me his support and guidance from when I first applied and was accepted into the Mechanical Engineering PhD program at the University of Maine Orono. Dr. Dehspndes support, guidance, and patience continued through the transfer we both made to The University of Texas Austin and through the culmination of this process. Dr. Dehspnde has given me a lot of his time and encouragement for which I am grateful.

To my Committee Members Dr. Ronald Barr, the coordinator, Dr. Rick Neptune, Dr. Raul Longoria, and Dr. Jonathan Dingwell. I would like to express my appreciation and many thanks for all of your comments and suggestions. Many thanks go to Dr. Benito R. Fernandez for all his helpful suggestions with modeling and control, and Dr. Scott Fish for allowing me to use his 3D printer and his assistance with the design and manufacturing process.

I would also like to thank James Debaker and Tess Hellebrehkers who worked with me on the material test, fabrication, and finger design. I appreciate all of your help over this past year. The UT ReNeu robotic Lab members who have given me so much encouragement, technical suggestions, and cooperation, I really have enjoyed and appreciate all of you.

To my wife, Caron and our daughter, Lauren I will be forever grateful for all the sacrifices, encouragement, and patience you both have given me. Knowing I always had two people who believed in me sometimes more than I believed in myself gave me the peace of mind I needed to overcome any and all challenges I faced.

Bio-inspired Robotic Joint and Manipulator: from Biomechanical Experimentation and Modeling to Human-like Compliant Finger Design and Control

Publication No. _____

Pei-Hsin Kuo, Ph.D.
The University of Texas at Austin, 2015

Supervisor: Ashish D. Deshpande

One of the greatest challenges in controlling robotic hands is grasping and manipulating objects in unstructured and uncertain environments. Robotic hands are typically too rigid to react against unexpected impacts and disturbances in order to prevent damage. The human hands have great versatility and robustness due, in part, to the passive compliance and damping. Designing mechanical elements that are inspired by the nonlinear joint compliance of human hands is a promising solution to achieve human-like grasping and manipulation. However, the exact role of biomechanical elements in realizing joint stiffness is unknown. We conducted a series of experiments to investigate nonlinear stiffness and damping of the metacarpophalangeal (MCP) joint at the index finger. We designed a custom-made mechanism to integrate electromyography sensors (EMGs) and a motion capture system to collect data from 19 subjects. We investigated the relative contributions of muscle-tendon units and the MCP capsule ligament complex to joint stiffness with

subject-specific modeling. The results show that the muscle-tendon units provide limited contribution to the passive joint compliance. This findings indicate that the parallel compliance, in the form of the capsule-ligament complex, is significant in defining the passive properties of the hand. To identify the passive damping, we used the hysteresis loops to investigate the energy dissipation function. We used symbolic regression and principal component analysis to derive and interpret the damping models. The results show that the nonlinear viscous damping depends on the cyclic frequency, and fluid and structural types of damping also exist at the MCP joint.

Inspired by the nonlinear stiffness of the MCP joint, we developed a miniaturized mechanism that uses pouring liquid plastic to design energy storing elements. The key innovations in this design are: a) a set of nonlinear elasticity of compliant materials, b) variable pulley configurations to tune the stiffness profile, and c) pretension mechanism to scale the stiffness profile. The design exhibits human-like passive compliance. By taking advantage of miniaturized joint size and additive manufacturing, we incorporated the novel joint design in a novel robotic manipulator with six series elastic actuators (SEA). The robotic manipulator has passive joint compliance with the intrinsic property of human hands. To validate the system, we investigated the Cartesian stiffness of grasping with low-level force control. The results show that that the overall system performs a great force tracking with position feedback. The parallel compliance decreases the motor efforts and can stabilize the system.

Table of Contents

List of Tables

List of Figures

Chapter 1

Introduction

Human-robot interactions are common in humanoid and rehabilitation robots (Accoto et al., 2012; Carpino et al., 2011; Huang et al., 2011; Gouaillier et al., 2008). As humans and robots begin to interact more closely, it is important that the interactions are safe while maintaining a high level of performance. A robot which can quickly adjust its compliance based on tasks or environments has a potential to achieve the safety and performance objectives. Robotic hands, end effectors for most humanoid robots, have been designed to safely interact with environments and contact with uncertain objects.

One of the greatest challenges in robotic hands is grasping and manipulating objects in unstructured and uncertain environments (Grebenstein et al., 2011; Wolf and Hirzinger, 2008). Without compliance, the robotic hands are too rigid to deal with unexpected impact and disturbance, so the damage is usually inevitably. Although the compliance can be achieved by tuning the stiffness through impedance control of the actuators based on real-time feedback from sensors (Haddadin et al., 2007), the trade-offs such as overweight and oversize, and high cost pose a challenge. Also the sensing is costly and often prone to error. Implementing human-like passive compliance has the potential to improve the abilities of the robotic hands.

Passive compliance has been implemented in various robotic designs (Marques et al., 2010; Pfeifer et al., 2012; Kim et al., 2006, 2008), but there exist only a few examples of robotic fingers with

passive compliance. These include the SDM Hand (Dollar et al., 2010), SPRING Hand (Carrozza et al., 2004), UB Hand 3 (Lotti et al., 2005), Karlsruhe hand (Pylatiuk et al., 2004; Kargov et al., 2007), and the DLR Hand (Grebenstein and van der Smagt, 2008; Grebenstein et al., 2010). The compliance in the robotic hands is typically invariant of the configuration, and is designed to achieve limited robustness during position control. In many cases, the passive invariant compliance is deemed detrimental to achieving good position control.

Most of the robotic hands have anthropometric structure, and some have tendon-driven system, as they are designed to accomplish tasks similar to those performed by the human hands. Mimicking mechanical structure and properties of the human hands is a major challenge in robotic hand design (Deshpande et al., 2010, 2008). Human hands have unique passive compliance and damping based on the nonlinear passive properties of soft tissues. In order to design a passive variable compliance that mimics the intrinsic properties of human hands, understanding the biomechanical insight of human hands is critical.

Each finger of the human hand has three joints with four degrees of freedom in each finger, in sequence from proximal to distal: metacarpophalangeal (MCP), proximal interphalangeal (PIP) and distal interphalangeal (DIP) joints. There are two types of muscles: the extrinsic muscles originate primarily in forearm, while the intrinsic muscles originate primarily in the palm. The extrinsic muscles divided into extensors and flexors across multiple joints in the fingers dominate the extension and flexion motion, respectively. The intrinsic muscles dominate the abduction and adduction motion. Collateral ligaments and volar plates (palmar ligaments) connect with bones and limit the hyperextension to stabilize the articular cartilages of the joints. Those components contribute to the passive joint stiffness structurally, and critically affects the hand function, and joint stability (Shrivastava et al., 2003; Minami et al., 1985; Tamai et al., 1988). However, the

exact role of biomechanical elements realizing joint stiffness is unknown. This leads to the first specific aim, which is to understand the relative contributions of the musculotendons, ligaments, and cartilages in human fingers to joint stiffness.

The passive damping stabilizes the active control of limb motions (Gielen and Houk, 1984; Esteki and Mansour, 1996; Wu et al., 1990). Understanding its role during limb movements is critical for clinical diagnoses (Lee et al., 2004; Hsieh et al., 2010; Oatis et al., 2013), physical rehabilitation (Oatis, 1993; Page, 2012), biomechanical modeling (Amankwah et al., 2004; Deshpande et al., 2012) and design of robotic devices (Carpino et al., 2011; Laffranchi et al., 2011). Most studies have attributed passive damping solely to viscosity while ignoring other damping effects (Wright and Johns, 1961). However, damping is a result of tissue viscosity, internal friction (Gleghorn and Bonassar, 2008), and thixotropic fluids in joint complex. So there is a need for development of a more sophisticated model of passive damping in human hand movements where low inertia of phalanges lead to dominant damping effects. The second aim of this thesis is to identify the model of nonlinear damping of human hand joints through the human experiment, and symbolic regression, and interpret the important damping types through the principal component analysis.

Given the background in biomechanical properties of the human hands, designing mechanical elements that are inspired by the nonlinear joint compliance of the human hands is a promising solution to achieve a human-like compliance. Some rotary designs with cam shape profiles have successfully incorporated passive compliant elements with variable torsional elasticity without additional actuators to regulate the joint stiffness (Accoto et al., 2012; Carpino et al., 2011; Kuo and Deshpande, 2013; Kim and Deshpande, 2014). Although using linear spring to integrate with cam of changing radius gives nonlinear stiffness, such a design depends on commercially available springs. Custom-made springs can be designed, but still the size and weight are too high for an

implementation in robotic hands. Therefore, adopting an alternative energy storing element is necessary. In this thesis, we introduce rubber-type of materials, and develop a miniaturized compliant joint in which the passive joint properties match those derived from the human experiments. To investigate the effect of passive nonlinear parallel compliance, we incorporate this design into a novel manipulator integrated with muscle-like actuator.

1.1 Thesis Overview

In this thesis, there are six chapters including the introduction chapter. We present the models of the passive nonlinear stiffness and damping of the MCP joint in Chapter 2 and Chapter 3. Chapter 4 presents a design that incorporates the biological information (nonlinear stiffness) into a purely mechanical design (miniaturized robotic joint). Chapter 5 presents a compliant manipulator integrated with human-like joint compliance and an SEA to investigate the effectiveness of joint compliance in grasping and manipulation. Chapter 6 provides a summary of the entire work and discusses applications and limitations of the results as well as directions of future work.

Chapter 2

Muscle-Tendon Units Provide Limited Contributions to the Passive Stiffness of the Index Finger Metacarpophalangeal Joint

2.1 Introduction

Intrinsic, passive joint stiffness of the fingers critically affects the hand functions and joint stability (Shrivastava et al., 2003; Minami et al., 1985; Tamai et al., 1988), however, the exact role of biomechanical elements realizing joint stiffness is unknown. Because of its prominent role in many hand functions, a number of studies have focused on investigating the joint stiffness of the index finger metacarpophalangeal (MCP) joint (Minami et al., 1985; Esteki and Mansour, 1996; Knutson et al., 2000; Kamper et al., 2002; Qin et al., 2010). The muscle-tendon units (MTUs) contribute to the passive MCP joint stiffness by generating resistive forces when stretched (Qin et al., 2010; Dennerlein, 2005). In addition to the MTUs, the capsule-ligament complex (CLC) at the joint provides resistance, especially to prevent joint instability (Minami et al., 1985; Tamai et al., 1988).

Parts of the chapter is published at the Journal of Biomechanics (Kuo and Deshpande, 2012). The co-author Ashish. D. Deshpande contributed parts of data analysis and technical writing to the published paper.

Parts of the chapter is published at the Journal of Mechanism and Robotics (Kuo et al., 2015). The co-author Jerad Hayes contributed parts of mechatronics design and fabrication to the research. The co-author Ashish. D. Deshpande contributed parts of data analysis and technical writing to the published paper.

However, a quantitative analysis to determine the relative contributions of MTUs and CLC to the passive joint stiffness, in various finger configurations, has not been carried out, which is the goal of this paper. Quantification of the relative contributions of the MTUs to the total joint stiffness is valuable for providing novel insights for the design of implants and arthroplasty (Elhassan et al., 2006; Beevers and Seedhom, 1999; Fowler and Nicol, 2002), developing clinical guidelines for the diagnosis and treatment of finger joint injuries (Werner et al., 2003; Fowler and Nicol, 2001), and developing more detailed models of hand biomechanics (Sueda et al., 2008; Wu et al., 2008; Fok and Chou, 2010).

It has been established through a number of previous studies that the resistive moment generated at the MCP joint due to the joint stiffness has a double exponential dependency on the joint angle (Esteki and Mansour, 1996; Knutson et al., 2000). A number of previous studies assume, either explicitly or implicitly, that this joint stiffness is strictly due to the passive forces from the stretching of muscles and tendons, and that the effect of CLC can be ignored (Qin et al., 2010; Dennerlein, 2005). However, this assumption is not substantiated by a quantitative analysis of passive moment generation. In a previous study it has been shown that the ligaments at the MCP joint contribute to the joint stiffness with a double exponential dependency (Minami et al., 1985). In another study contributions of extrinsic tissues (extrinsic muscles) and intrinsic tissues (intrinsic muscles and CLC element) have been determined (Knutson et al., 2000), but the extrinsic contribution is estimated based on the effects of wrist position, which does not account for the MTUs contributions correctly.

Given that the index finger is controlled by a network of long, stiff tendons, and that the MTUs are stretched by considerable lengths through the range of finger motions, the passive forces due the MTUs might affect the joint passive torque considerably. Therefore, we hypothesize that

the seven MTUs are the main contributors to the total moment and work due to passive stiffness at the MCP joint. By testing the hypothesis through mathematical modeling of total joint stiffness and the effect of stiffness due to muscles and tendons, our goal is to determine the relative contributions of the MTUs and CLC, and will support or deny the validity of the assumption common in the literature. Another goal is to separate the contributions to the joint stiffness due to the intrinsic and extrinsic muscles.

2.2 Method

In this section, we firstly introduce a customer-made mechanism that allowed us to collect passive force and kinematic data from human subjects. Secondly, we describe information of experiment participants and experimental design in details. Finally, we demonstrate a subject-specific musculoskeletal modeling and data analysis.

2.2.1 Mechanism Design

We present a design of a mechanism to measure the passive moments of the MCP joint of the index finger during static and dynamic tests (Fig. 2.1). Here are the key features of the mechanism:

1. **Precision of the forces sensing**: Attaching force/torque sensors directly on the measured fingers includes significant error caused by the local deformations of the soft tissues. Even with the braces, the sliding between the braces and the fingers increases the difficulty to measure reliable force under dynamic conditions. We designed a flushed contact mechanism with force sensors and extended linkages, which allows us to estimate the overall passive torque of measured joint and resolve the issue raised by the skin deformation and sliding.

2. **Accuracy of the joint kinematics**: The center of rotation of the human articular joint does not have a fixed point. Therefore, it is problematic to measure joint angle and torque by attaching sensors directly on the joint. Infrared motion capture is an non-invasive method for estimating joint rotations accurately. The mechanism is carefully designed to integrate with the customized reflective markers and infrared motion capture system.

3. **Customizability of the device**: Subject specific design is considered in the mechanism. We have designed a test panel and driving arm that can be easily adjusted to fit different sizes of the human hands. The mechanism can collect the data for different finger joints with various wrist postures by changing the configuration of moving clamps and different sizes of finger braces. The mechanism is able to collect wider range of motion for the MCP joint compared with previous studies.

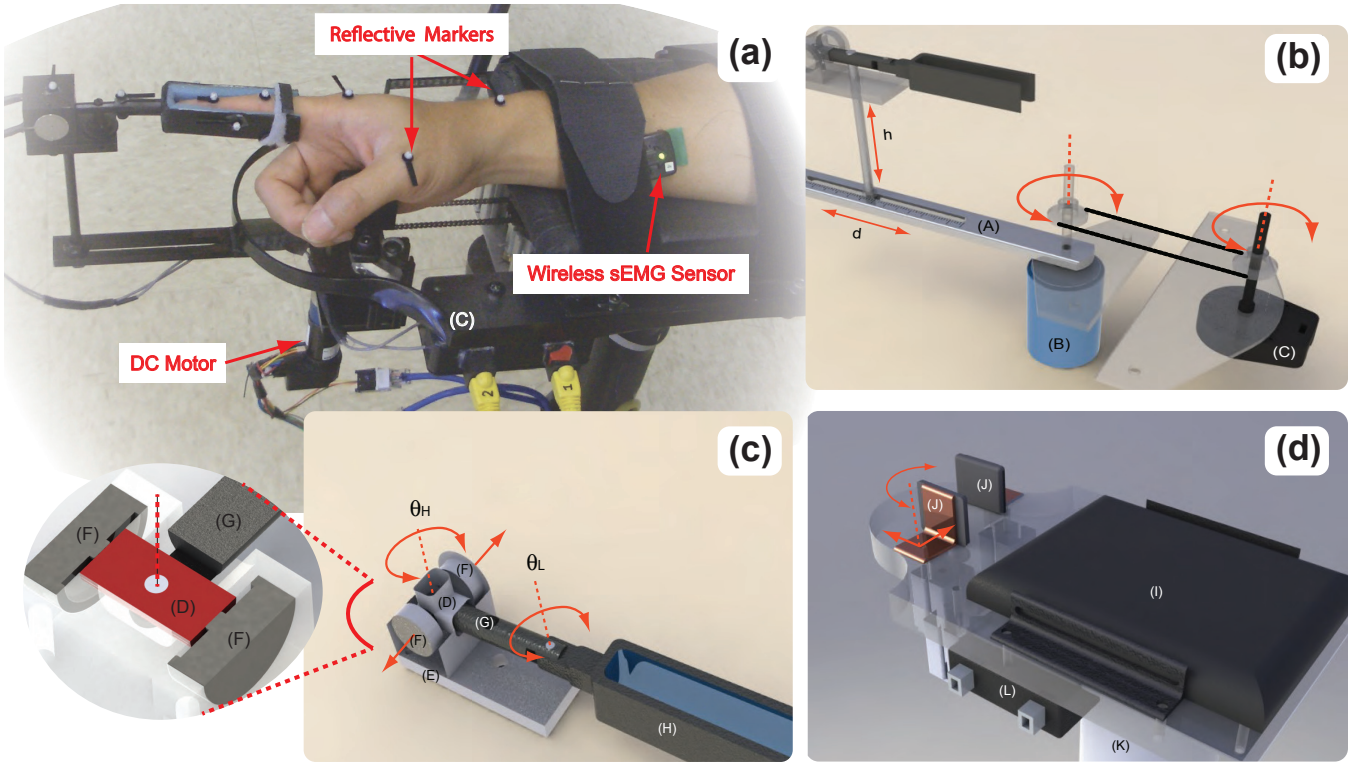

Figure 2.1: **(a) Rest position of the subject's hand and the full setup of the mechanism**. First, we attached the markers and EMG sensors on the subject's forearm and aligned the MCP joint with the shaft of the DC motor. Then, we fixed the forearm on the testing panel with the velcro straps and the arm rest, and adjusted the palm holders to fixed the hand at the zero position. Finally, we adjusted the driving arm to fit the index figner into the splint. After we secured the subject's hand on the meahcnism, we manually moved the driving arm to test the setup. **(b) Design of the driving arm and its sub parts**. The load cell holder attached on the moment arm (A) can be adjusted with the height (h) and the distance (d) to fit the different hand sizes. The DC motor (B) and the encoder (G) is connected by a chain and sprocket drive. **(c) Design of a load cells holder and splint linkage**. A piece called the "hammer" (D) achieves a flush contact between the splint mechanism and the load cell throughout the range of motion of the finger. The arrows indicate the sliding direction of the hammer. The hammer and the cylinder have a size tolerance 0.1 mm so that the hammer can slide along the cylinder. The hinge joint in the hammer allows a relative rotation between the hammer and linkage expending out from the holder. The subplot shows a section view of the hammer design. **(d) Design of the testing panel and adjustable stand**. The palm holders(J) can be moved and fixed to the desired direction and rotate for 360° through the two slots on the testing panel. The palm holder can fix the palm in place for all subjects.

2.2.2 Human Subjects and Experimental Procedure

A total of ten right-handed healthy subjects (6 males, 4 females) ranging in age 23 ($\pm$3.7) years were recruited for this study. The anthropometric data of the index fingers was measured for each subject (Table 2.1).

Table 2.1: Measurements of the anthropometric parameters (in mm) averaged across 10 subjects. It is assumed that the finger segment has an uniform rectangle shape with rectangular cross-section. Each subject signed an informed consent form in agreement with the university's human subject policy.

	Length	Breadth	Thickness	Joint Thickness
Proximal	45.0(3.5)	14.8(1.1)	14.5(1.1)	21.6(4.9)
Intermediate	25.3(1.7)	13.7(1.1)	11.6(1.2)	13.9(1.3)
Distal	23.6(1.8)	11.5(1.2)	8.7(0.7)	10.2(0.8)

The subject's hand was placed into a custom-designed device for the experiments (Fig. 2.1). The device fixed the subject's index finger and allowed other fingers to be relaxed so that the index finger could rotate freely in the horizontal plane. Each subject performed the maximal isometric index finger flexion and extension for sEMG normalization and scaling purposes. The device drove the subject's index finger with 10° increments from the neutral position, defined by the encoder, to the direction of full extension and reversed the direction of finger rotation to full flexion for two cycles. The device held each finger position for 30 seconds during which the forces reached a steady state due to the muscle relaxation (Esteki and Mansour, 1996). The limit of the range of motion (RoM) was decided for each subject when the subject started to feel uncomfortable close to the extremity of the rotation. To monitor the muscle relaxation for the subjects, we attached four wireless electromyographic sensors on the subject's flexor digitorum superficialis (FDS), extensor digitorum communis (EDC), biceps and triceps to monitor the muscle relaxation (Trigno, DelSys, Inc.). For EDC, we placed an electrode at the mid-forearm on a line drawn from the lateral

epicondyle to the ulna styloid process; for FDS, an electrode was placed around the center point on the line joining the medial epicondyle to the ulna styloid process (Danion et al., 2002). We placed the electrode on the bulk of the biceps in mid-arm and four fingerbreadths distal to the posterior axillary fold of the triceps (long head) (Perotto and Delagi, 2005). A motion capture system (Vicon Inc.) with six infrared cameras (500 Hz) and 18 reflective markers (diameter: 4.17 mm) was used to collect the three-dimensional kinematic data of the MCP joint during the experiment in order to precisely determine the MCP joint angle during movements. Each subject performed two repetitions of full range of flexion-extension motion. The forces at the finger tip, EMG signal, and the finger's kinematic data were collected simultaneously during the experiments.

2.2.3 Data Analysis

The kinematic data of the markers was filtered and synchronized with the EMG signals (Nexus 1.7.1, Vicon Inc.). Using the marker data, the location of the instant center of rotation (iCoR) and the MCP flexion-extension angle were determined through an optimization process (Halvorsen et al., 1999; Kuo et al., 2011). We defined the MCP angle to be zero along the line joining the wrist and MCP joint centers, positive in flexion and negative in extension. We normalized the EMG signals of each muscle by measuring the EMG signals from the maximal voluntary isometric contraction test before proceeding with the experiment. We processed the raw EMG signals with a 4^{th} order bandpass Butterworth filter ($20 \sim 500$ Hz), performed full-wave rectification, and then passed it through a low pass filter with a cut-off frequency of 5 Hz to derive the linear envelop EMGs. We adopted the average of the linear envelop EMG as 100% effort of muscle activations. The data from a trial was eliminated when either one of four EMG signals exceeded the thresholds with 5% of the determinations from the maximal voluntary isometric contraction

test (Nordez et al., 2008).

2.2.3.1 Total Elastic Moment (τ_{total})

The total passive moment due to joint stiffness is given by: $\tau_{total} = l_{tip} \times F_{tip}$, where l_{tip} is the distance between the location of the force sensor and the iCoR of the MCP joint. A double exponential model, given in Eq. 2.1, was employed to describe the relationship between the total passive elastic moment and the MCP joint angle (Esteki and Mansour, 1996; Knutson et al., 2000; Silder et al., 2007):

$$\tau_{total}(\theta_m) = A(e^{-B(\theta_m - E)} - 1) - C(e^{D(\theta_m - F)} - 1), \tag{2.1}$$

where θ_m is the angle of the MCP joint, and A to F are the parameters of the fitting model. We estimated the seven model parameters for each subject by using a nonlinear least squares method that minimizes the sum of square differences between the measured moment and fitting model in Matlab (Mathworks Inc.). The slack angle (θ_{ms}), defined as the relaxed position of the index finger, was determined in the fitting model at which τ_{total} was equal to zero (Kamper et al., 2002).

2.2.3.2 Elastic Moment from MTUs (τ_M)

The net elastic moment by the seven MTUs that cross the MCP joint (Table 2.2), $\tau_{MTU}(\theta_m)$, varies with the MCP joint angle and is given by Eq. 2.2:

$$\tau_{MTU}(\theta_m) \;=\; \sum_{i=1}^{7} R_i(\theta_m) \cdot F_{pi}(\theta_m), \qquad i = 1, ..., 7 \tag{2.2}$$

where $R(\theta_m)$ is the vector of the moment arms of the seven MTUs with respect to the MCP joint angle and $F_p(\theta_m)$ is the vector of passive forces generated by the seven MTUs in response to the stretch due to change in θ_m. The moment arms for the seven MTUs vary as θ_m changes

Table 2.2: Results of scaled parameters for the seven muscles (n= 10).

Muscle	Abbreviation	$F_{mo}(N)$	l_{mo} (mm)	l_s (mm)	$\alpha(^\circ)$
Extensor digitorum communis	EDC	18.9 ± 3.2	61.9 ± 4.4	289.9 ± 20.9	3
	EDC[a]	(18.26)	(70)	(322)	
Extensor indicis	EI	22.5 ± 3.8	52.1 ± 3.7	167.7 ± 12	6
	EI[a]	(21.7)	(58.9)	(186)	
First palmar interosseous	PI[b]	18.3	30.7	25	6.3
Flexor digitorum profundus	FDP	75.9 ± 17.9	67.2 ± 7	265.2 ± 19.1	7
	FDP[a]	(68.3)	(74.9)	(293.5)	
First lumbrical	LU[b]	2.7	68	55.4	1.2
Flexor digitorum superficialis	FDS	68.1 ± 16.1	72.7 ± 3.9	247.5 ± 18	6
	FDS[a]	(61.24)	(83.5)	(275)	
First dorsal interosseous	DI[b]	36.6	38.9	31.7	9.2

Note: $()^a$ show the generic values of four extrinsics from (Lieber et al., 1990; Holzbaur et al., 2005) and $()^b$ show the constant values of three intrinsics adopted from (Jacobson et al., 1992; Wu et al., 2008).

Table 2.3: Scaling factors of the moment arm (r_v), l_{mto} (r_V), and F_{mo} (r_f and r_e) for ten subjects.

Factor	1	2	3	4	5	6	7	8	9	10
r_v	0.68	1.26	0.85	0.84	0.87	0.88	0.80	0.98	0.84	0.62
r_V	0.43	0.79	0.53	0.53	0.55	0.55	0.50	0.62	0.53	0.39
r_f	1.50	1	1.21	1.19	0.64	1.25	1.29	1.12	1.22	0.71
r_e	1.22	1	1.09	0.93	0.97	1.35	1.02	1.05	1.04	0.69

and we used the model derived for the ACT Hand MCP joint to determine the values of moment arms (Deshpande et al., 2010). We assumed that the moment arms are proportional to the volume of index finger (Kociolek and Keir, 2011) and calculated the subject-specific moment arms of the seven MTUs by scaling the ACT hand moment arms with a ratio of the volume of subject's index finger (v) to the ACT hand index finger (V):($r_v = \frac{v}{V}$, Table 2.3). The scaled moment arms were also used to calculate the length change of MTUs (l_{mt}) due to change in θ_m as: $\Delta l_{mt_i}(\theta_m) = R_i \times \theta_m$, where $i = 1...7$ refers to the number of the MTU.

To determine the passive stiffness generated by these seven MTUs as the MCP joint is moved passively through its full range of motion, the MTUs are assumed to be composed of two nonlinear springs, representing the muscle and tendon, connected in series as shown in Fig. 2.2. Four parameters define the static passive force-length relationships in the Hill-type MTU model, namely, the maximal isometric force (F_{mo}), optimal muscle fiber length (l_{mo}), tendon slack length (l_{ts}), and pennation angle (α^m) (Gonzalez et al., 1997; Delp, 1990; Zajac, 1989). Values for these parameters have been determined in the previous works through cadaver studies and modeling techniques (Jacobson et al., 1992; Lieber et al., 1990; Greiner, 1991; Manal and Buchanan, 2004; Holzbaur et al., 2005; Delp et al., 2007), and in this study we adapted the F_{mo}, l_{mo}, and l_{ts} values for each subject. Because of small pennation angles for the seven muscles (Lieber et al., 1990; Jacobson et al., 1992), we maintained same values of pennation angles for all of the subjects.

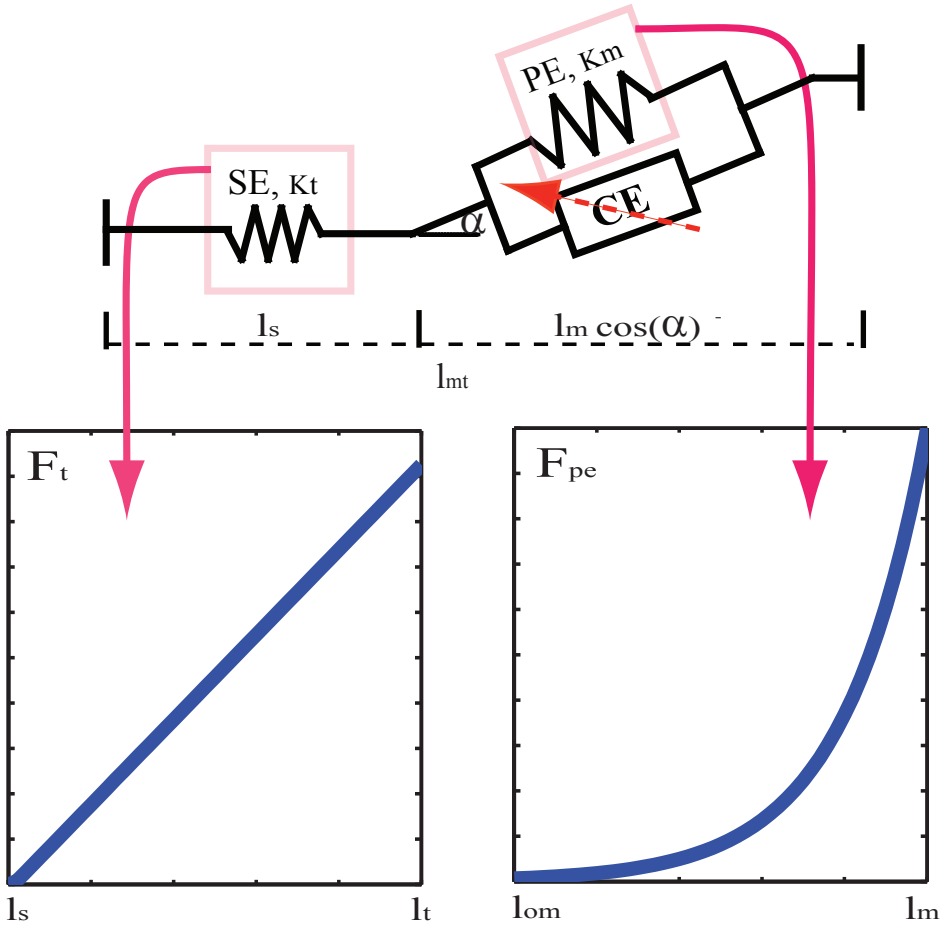

Figure 2.2: A schematic showing the muscle and tendon element of the Hill-type model. Each MTU is modeled as two nonlinear springs connected in series. The force generated by the MTU for the given change in length is calculated by using the passive force-length relationships for the muscles and tendon. The passive force-length relationship in the muscle is given by $f_m(\widetilde{l}_m) = \frac{e^{10(\widetilde{l}_m - 1)}}{e^5}$, $F_m = F_{mo} f_m \cos(\alpha_m)$, where $\widetilde{l}_m = \frac{\Delta l_m}{l_{mo}}$. The passive force-length relationship in the tendon is given by $f_t(\epsilon_t) = 0$ when $\epsilon_t \leq 0$, $f_t(\epsilon_t) = 1480.3{\epsilon_t}^2$ when $0 < \epsilon_t < 0.0127$, $f_t(\epsilon_t) = 37.5\epsilon_t - 0.2375$ when $\epsilon_t \geq 0.0127$, $F_t = F_{mo} \cdot f_t$, where $\epsilon_t = \frac{\Delta l_t}{l_{ts}}$. With two nonlinear springs in series the force generated by the two is equal: $F_m = F_t$ and the total length change is sum of the length changes: $\Delta l_{mt} = \Delta l_m + \Delta l_t$ (Kuo and Deshpande, 2010).

The voltages generated by the EMG signals from the maximal voluntary isometric contraction (MVC) were used to scale F_{mo} values for the four extrinsic muscles. First, we identified a subject (Subject 2) whose index finger volume matches closely (79.08%) with the model presented by Holzbaur (Holzbaur et al., 2005), and we assigned the F_{mo} values of the extrinsic muscles (FDP, FDS, EDC and EI) from Holzbaur's model to Subject 2's model. Then we calculated the ratio of the EMG value from MVC in flexion and extension for each subject and Subject 2. The EMG ratios in flexion and extension were used to scale the F_{mo} of the two flexors and two extensors between subjects (r_f and r_e in Table 2.3).

We calculated the subject specific nominal MTU lengths, l_{mto}, by linearly scaling the l_{mto} values from Holzbaur's model with the volume ratio (r_V) for each subject (Table 2.3) (Kociolek and Keir, 2011). The tendon slack lengths (l_{ts}) were functionally adjusted for each subject by implementing the numerical optimization method described in a previous study (Manal and Buchanan, 2004). The muscle fiber lengths (l_m) were randomly selected as inputs in the fully flexed, fully extended and relaxed positions. The optimal muscle length values were then calculated for each subject as: $l_{mo} = l_{mto} - l_{ts}$ at the relaxed position after the tendon slack lengths were updated. Table 2.2 shows the statistical results of the scaling parameters.

2.2.3.3 MTUs Contribution

The total passive joint moment (τ_{total}) at the MCP joint is assumed to be composed of the elastic moment from the stretching of the seven MTUs (τ_{MTU}) and the passive moment from the CLC (τ_{CLC}). Values for τ_{total} and τ_{MTU} are determined by following the steps explained above and τ_{CLC} is estimated from Eq. (2.3).

$$\tau_C = \tau_T - \tau_M \tag{2.3}$$

To evaluate the contributions of the MTUs to the joint stiffness, we computed the mechanical work of the passive moments at the MCP joint using Eq. 2.4.

$$\begin{aligned} W &= W_f + W_e \\ &= \left| \int_{\theta_{ms}}^{\theta_{mf}} \tau(\theta) d\theta \right| + \left| \int_{\theta_{ms}}^{\theta_{me}} \tau(\theta) d\theta \right| \end{aligned} \tag{2.4}$$

where, θ_{me} and θ_{mf} are the values of the MCP angle in full extension and full flexion, respectively, θ_{ms} is the slack angle, and W_f and W_e represent work done in flexion and extension, respectively. We calculated the work done by τ_{total} and τ_{MTU} as W_{MTU} and W_{total}, respectively using Eq. 2.4 and then computed the contribution: $\eta = \frac{W_{MTU}}{W_{total}} \times 100$. We also calculated the MTU contribution to the total work in flexion: $\eta_f = \frac{W_{MTU_f}}{W_{total_f}} \times 100$ and also in extension: $\eta_e = \frac{W_{MTU_e}}{W_{total_e}} \times 100$. One sample t-test and the power analysis were used to test our hypothesis as a post hoc ($\alpha = 0.05$ and $power = 0.8$).

2.3 Results

2.3.1 Model of Total Passive Moment

For all the subjects, the slack angle, θ_{ms} is located at $\theta_m > 0^\circ$ (Table 2.4). The total passive moment in full extension (τ_{total_e}) is larger (438.1 ± 184.61 N-mm) than that in full flexion ($\tau_{total_f}, 288.41 \pm 71.41$ N-mm). The double exponential model defined by the parameters given in Table 2.4 closely fits each subject's passive moment-angle data, with the R^2 value greater than 0.9 and RMSE value smaller than 50 N-mm. The fit between the experimental data and the model for Subject 7 is shown in Fig. 2.3.

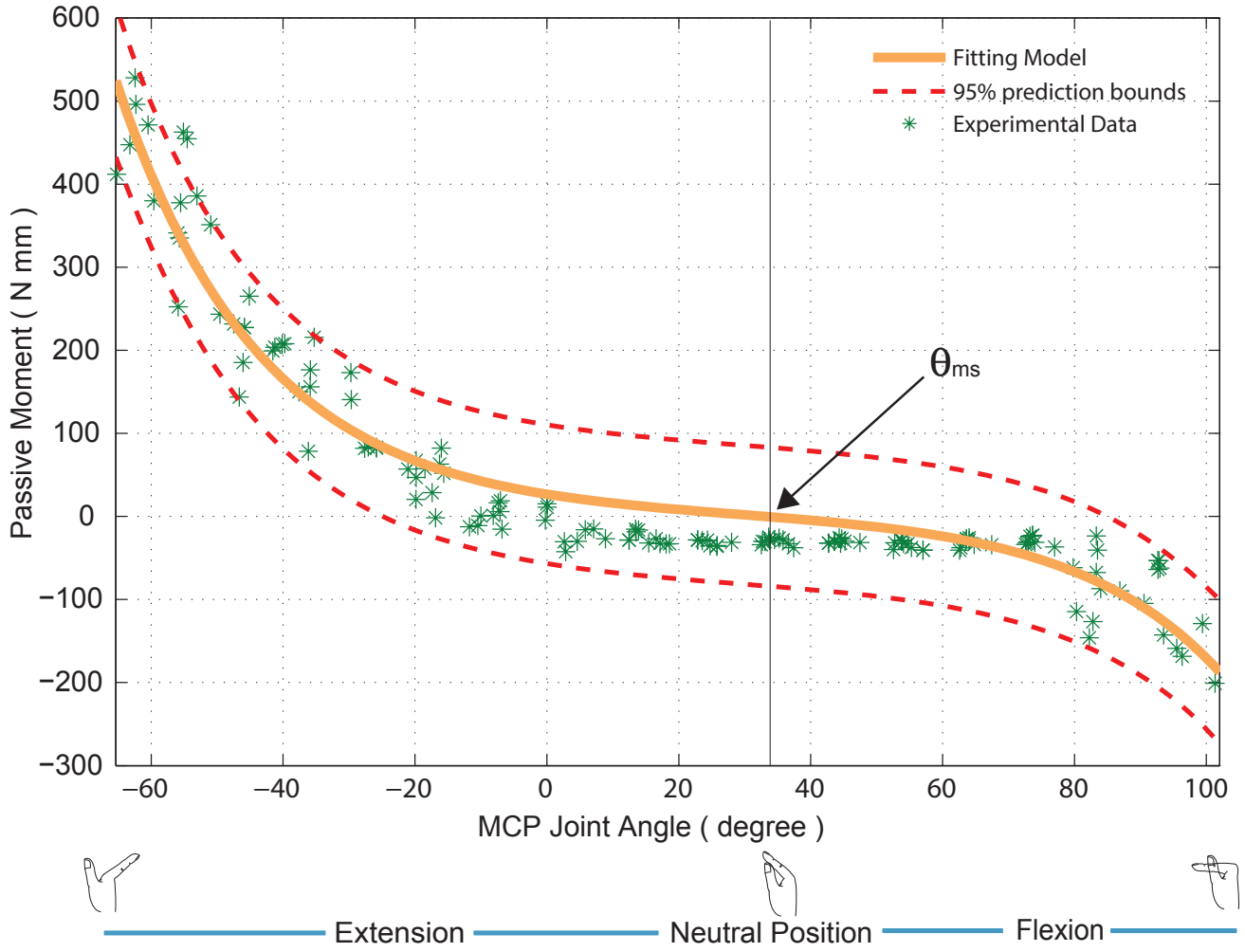

Figure 2.3: Experimental data and the double exponential fitting model for Subject 7. The 95% confidence interval predicts the mean total moment of the MCP joint from the experimental data. The slack angle (θ_{ms}) determines the relative contributions of the extensors and flexors to the MTU passive moment. A high positive value of θ_{ms} means a larger range of extension than that with a low positive value of θ_{ms}, leading to larger stretch and passive moments by the flexors (FDS and FDP).

Table 2.4: Results from fitting the double exponential model of the MCP joint moment and angle data. The ranges of the MCP joint angles and the passive moments recorded from the experiment and the coefficients of the fitting model for the ten subjects are given. The MCP angle is measured from the line joining the wrist and MCP joint centers, θ_{ms} is the slack angle of the MCP joint, $\theta_m \in [\theta_{me} \quad \theta_{mf}]$ is the range of motion, τ_{total_e} and τ_{total_f} represent the maximal passive joint moment in full extension and full flexion.

	Experimental Results					Fitting Model							
Subject	θ_{me} (deg)	θ_{ms} (deg)	θ_{mf} (deg)	τ_{total_e} (N-mm)	τ_{total_f} (N-mm)	A	B	C	D	E	F	$RMSE$	R^2
1	-59.22	11.79	97.21	573.00	-292.20	0.27	0.06	13.28	0.03	72.83	-6.74	23.86	0.93
2	-57.30	21.24	102.48	334.70	-278.10	0.01	0.08	4.11	0.05	73.95	16.32	15.71	0.9
3	-68.55	9.02	108.54	372.10	-222.00	0.19	0.05	23.82	0.02	73.55	-1.42	15.12	0.94
4	-79.45	26.77	98.79	381.90	-259.90	5.54	0.03	1.71	0.07	74.51	15.34	36.74	0.74
5	-69.43	9.20	98.44	470.70	-209.58	3.00	0.04	28.22	0.02	70.18	-18.27	29.25	0.9
6	-59.24	11.96	98.79	682.50	-433.70	3.60	0.05	2.28	0.03	47.43	-51.86	29.18	0.92
7	-65.36	32.97	102.65	558.10	-329.70	1.01	0.05	3.39	0.05	70.96	13.68	17.62	0.95
8	-55.72	8.75	93.25	477.36	-280.31	0.53	0.05	15.83	0.03	73.51	-11.43	36.81	0.93
9	-67.41	23.60	103.11	609.79	-213.63	4.54	0.03	22.32	0.02	75.49	-5.73	32.89	0.94
10	-64.73	19.45	101.63	358.93	-364.99	1.44	0.05	16.72	0.03	71.23	-4.65	41.43	0.93

2.3.2 Model of Passive Moment from MTUs

The passive forces generated by the extrinsic MTUs, including the flexors (FDP and FDS) and extensors (EDC and EI), increase exponentially with the stretching length, and the resulting moment has an exponential dependency on the joint angle (Fig 2.4(a) and 2.4(c)). The passive muscle moment is zero for flexors in flexion and extensors in extension. The passive forces generated by the intrinsic MTUs have non-monotonic dependencies on the stretch in the length and the resulting joint moments are non-monotonic with respect to the MCP angle change (Fig 2.4(b) and 2.4(d)).

The extrinsic MTUs stretched by longer lengths and generated higher passive forces than the intrinsic MTUs. For example, in the case of Subject 7 the extrinsic MTUs generated passive forces ranging from 2 N to 15 N with stretching lengths over 14 mm (Fig. 2.4(e) and 2.4(f)). On the other hand, intrinsic MTUs showed the limited length excursions and force generation capacity. Even for the strongest intrinsic muscle DI, the maximal value of stretching length and passive force is only 2.34 mm and 0.267 N, respectively.

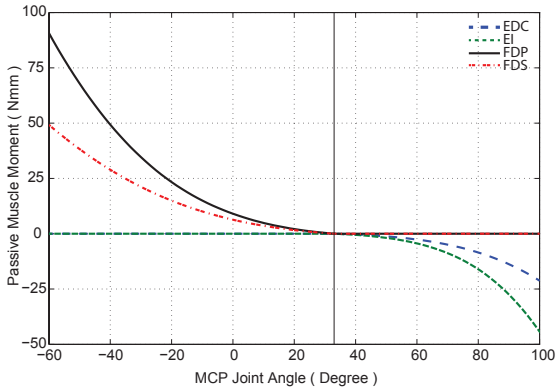

(a) Extrinsic MTU moments w.r.t. MCP joint angle

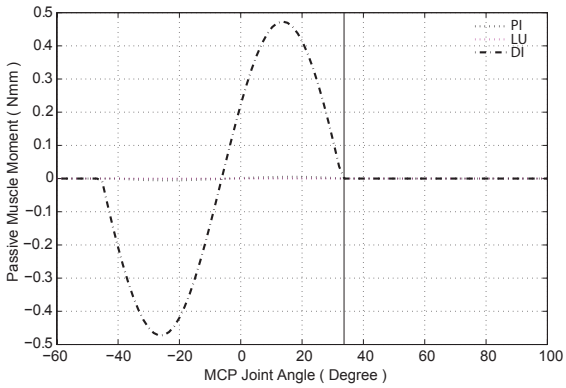

(b) Intrinsic MTU moments w.r.t. MCP joint angle

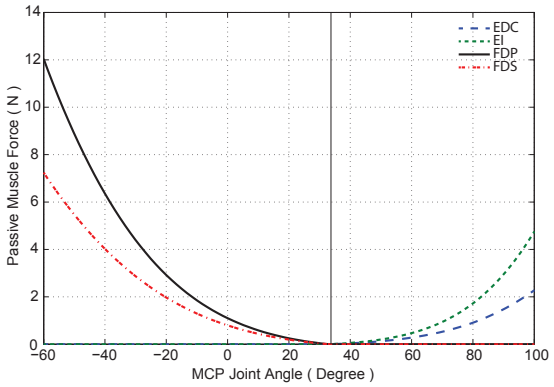

(c) Extrinsic MTU forces w.r.t. MCP joint angle

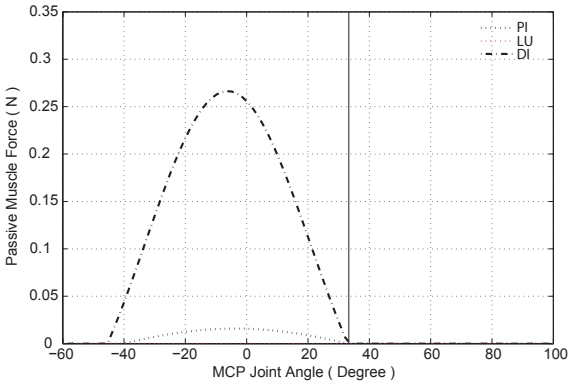

(d) Intrinsic MTU forces w.r.t. MCP joint angle

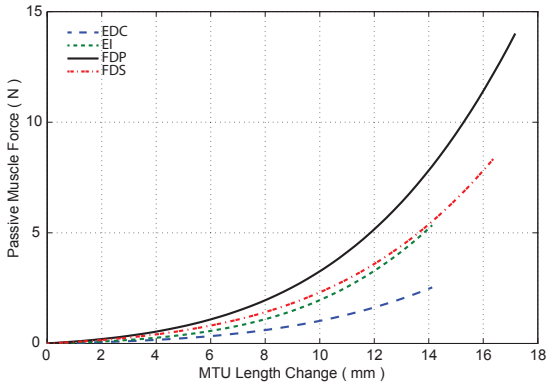

(e) Extrinsic MTU forces w.r.t. muscle excursions

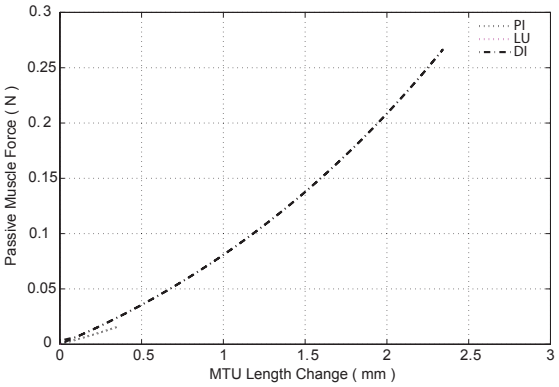

(f) Intrinsic MTU forces w.r.t. muscle excursions

Figure 2.4: Passive moments and forces of the extrinsic MTUs ((a), (c) and (e)) and the intrinsic MTUs ((b), (d) and (f)) for Subject 7.

A comparison of the maximal forces calculated by using the MTUs model presented in this study and a previous model based on cadaver hand data (Ranney et al., 1987) shows that the maximal force values predicted from our model were smaller than the predicted values from the cadaver model, except in the case of the EDC and EI muscles for several subjects (Fig. 2.5). For this comparison, the maximal muscle stretch values from the MTUs model were used to determine the muscle forces with the cadaver hand model.

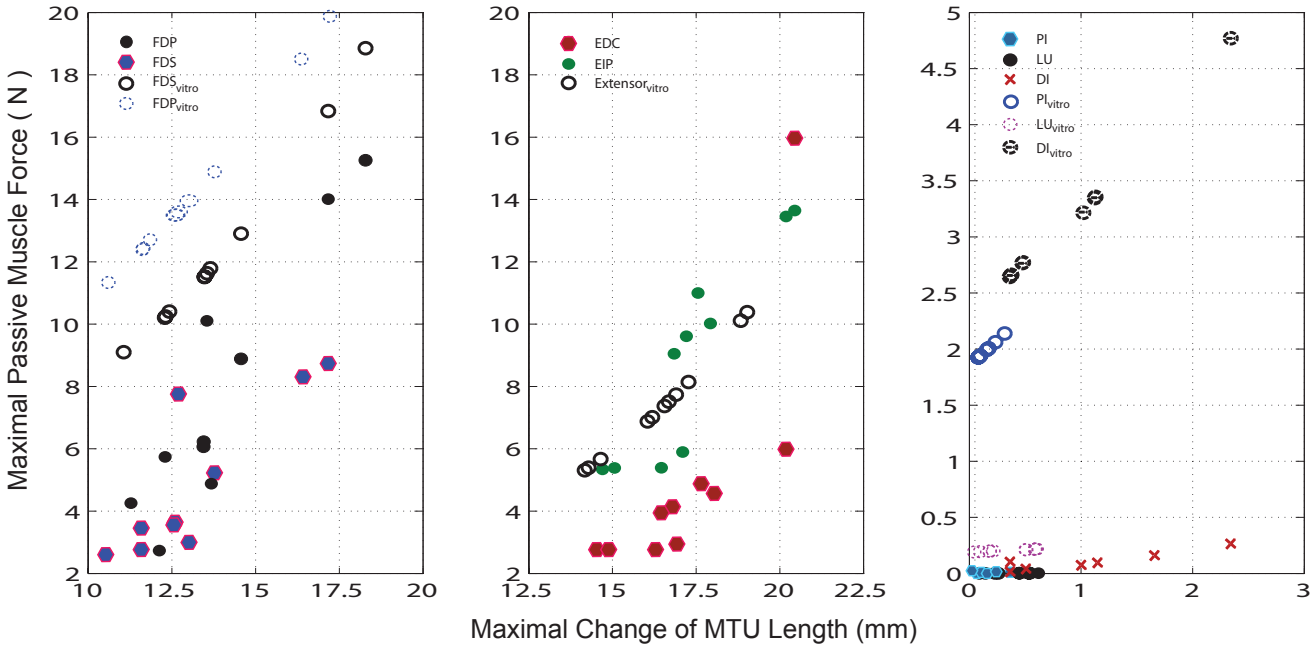

Figure 2.5: The maximal MTU passive force and maximal MTU stretch derived from the subject-specific models (dots) and previously developed model from cadaver data (circles) (Ranney et al., 1987). For the sake of comparison, we adopted the values of the maximal MTU excursion (Δl_{mt}) from the ten subjects as inputs to the passive force-length equation given in (Ranney et al., 1987): $F_p = \beta_1 e^{\beta_2 \cdot \Delta l_{mt}}$, and the values for the two parameters β_1 and β_2 were adopted from (Ranney et al., 1987).

2.3.3 Relative Contributions of MTUs and CLC

For all the subjects, the sum of the passive moments due to the stretching of the MTUs increases exponentially as the MCP joint is flexed or extended. The increase in the passive moment due to the stretch in the MTUs in flexion and extension of the MCP joint (τ_{MTU}) is significantly lower ($p < .001$) than the total increase in passive moment (τ_{total}), leading to a large value of passive moment due to the CLC (τ_{CLC}) (Fig. 2.6). The passive moment due to the CLC also increases exponentially as the MCP joint is flexed or extended.

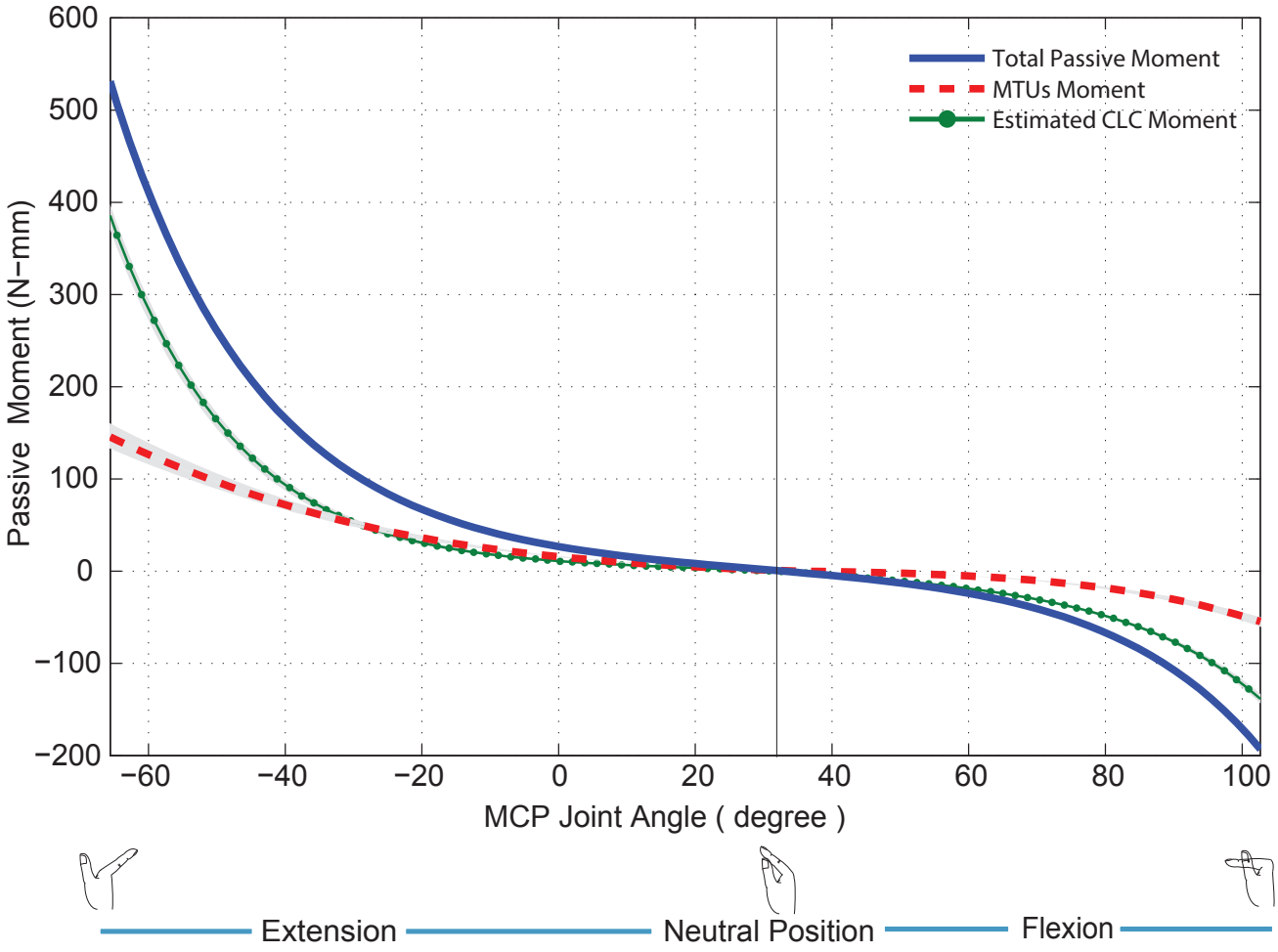

Figure 2.6: Variations in the total passive moment τ_{total}, the passive moments due to the MTUs τ_{MTU} and the CLC τ_{CLC} for Subject 7. The moment due to the CLC was determined from the double exponential model and the MTUs model using Eq. 2.3. The gray areas around the red and green curves represent the 95% confidence intervals of the MTU moment and the estimated CLC moment.

Fig. 2.7 shows that the work done by the lengthening of the MTUs is significantly lower than the total work done due to finger flexion and extension ($p < .001$). Thus the contribution of work η

is less than 50% of the total work. For all the subjects, the contribution of the MTUs to the total work in flexion η_f is greater than that in extension η_e, although in both cases the contribution from the CLC dominates ($p < .001$) (Fig. 2.8).

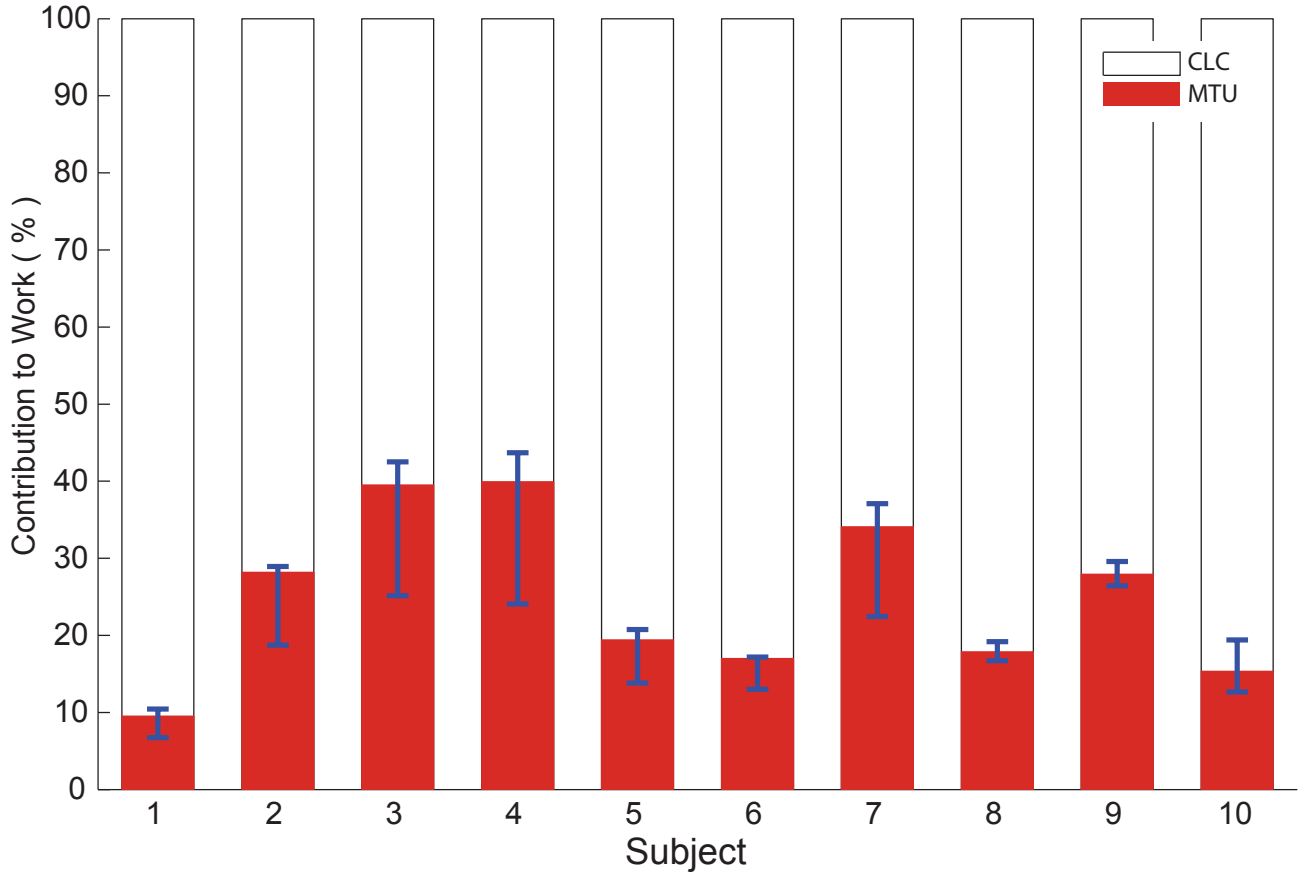

Figure 2.7: Relative contribution of the MTUs and CLC to the total work done to the passive moment through the range of motion for each subject. The contribution of the MTUs to the total work, η (24.87 ± 10.61), is significantly less than 50% of the total work, $t(9) = -7.49$, $p < .001$, $power = 0.68$.

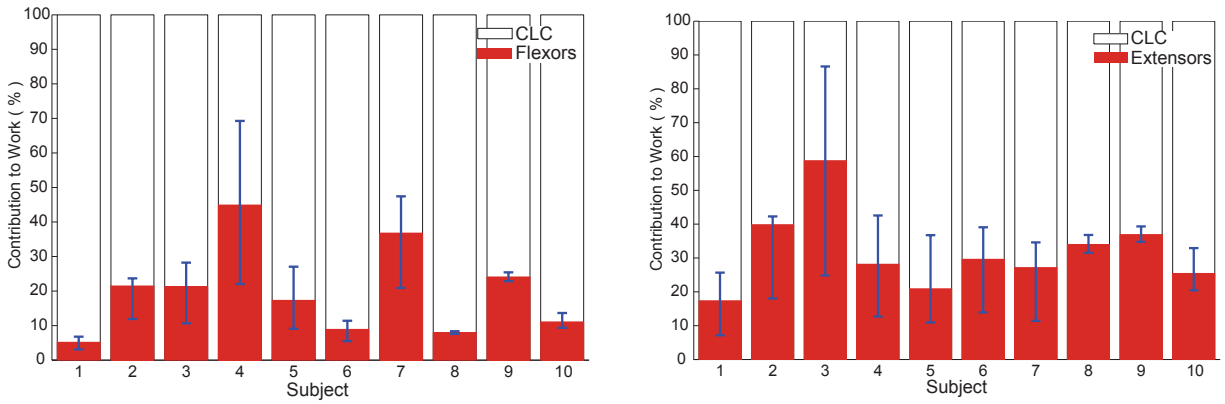

(a) Work contribution in extension direction η_f

(b) Work contribution in flexion direction η_e

Figure 2.8: Relative contribution to the work of the flexors and CLC in extension, and extensors and CLC in flexion. The contribution of the flexors to the total work in extension, η_f (31.81 ± 11.69), is significantly less than 50%, $t(9) = -4.92$, $p < .001$, $power = 0.67$. On the other hand, the contribution of the extensors to the total work in flexion, η_e (19.88 ± 12.9), is also significantly less than 50%, $t(9) = -7.38$, $p < .001$, $power = 0.68$.

2.4 Discussion

The purpose of this study was to investigate the relative contributions of the MTUs and CLC to the total passive stiffness at the index finger MCP joint in flexion and extension. Our results showed that the MTUs produced less than 50% of the contribution to the total work and moment due to stiffness at the MCP joint, so the hypothesis that MTUs provide the majority of the contribution to the joint stiffness was not supported.

We conducted experiments with human subjects to collect data for the model of the total passive moment at the MCP joint. A double exponential model provides a good fit for total stiffness and joint angle data. We estimated the passive muscle moments for the seven MTUs using a model consisting of two nonlinear spring in series. The effect of the CLC to stiffness at the MCP joint

is calculated indirectly using the total passive moment and that due to the MTUs. The passive moment calculated from the MTU models does not match with the total passive moment, leading to large values of the CLC passive moments. Interestingly, the estimated passive moment due to the CLC also shows double exponential variation as the MCP joint angle varies (Fig. 2.6), which matches with the previous capsuloligamentous elasticity models (Minami et al., 1983, 1985; An et al., 1985). A previous study determined the effect of wrist angle change on the passive moment at the MCP joint (Knutson et al., 2000), whereas our study focused on the determination of the passive moments due to the MTUs (intrinsic and extrinsic) and the CLC in the neutral wrist position. The contributions of the MTUs and CLC in the neutral wrist position determined from the two studies are comparable.

The work done due to the passive moment generation was used as a metric for the determination of the contributions to stiffness from the MTUs and CLC. The CLC contributed to more than 50% of the total work (Fig. 2.7), and this trend is maintained in flexion and extension (Fig. 2.8). The MTUs' contribution in flexion is higher than that in extension because of larger range of motion in flexion at which extensors have higher torque generation abilities with longer muscle excursions (Table 2.4). The contribution of the MTUs to the joint stiffness varies with the MCP joint angle.

The extrinsic flexors and extensors provided the majority of MTU passive moment and the contribution of the intrinsic MTUs was negligible (Fig. 2.4). The flexion and extension of the MCP joint resulted in much greater stretching of the extrinsic MTUs compared to the intrinsic MTUs. Also the extrinsic MTUs have higher maximal isometric forces than the intrinsic MTUs, leading to many times higher passive force generation in the extrinsic MTUs than the intrinsic MTUs.

In an in-vivo study, the parameter values for the passive force models are estimated with the underlying assumption that the MCP joint stiffness is the result of only the muscle passive

forces (Qin et al., 2010). Based on the results of our study showing that the CLC provides dominant stiffness contribution, the results from this study may have to be updated. The maximal passive forces generated at the maximal stretch of each MTU were comparable, but generally smaller than the predicted maximal passive forces calculated by using models based on the data from cadaver hands (Fig. 2.5) (Keir et al., 1996; Ranney et al., 1987). For the sake of comparison, we used the same MTU stretch values in our model and in the models developed in a previous study (Keir et al., 1996). The higher force value may have resulted due to the overestimation of the in-vivo passive force values using the in-vitro muscle models (Qin et al., 2010).

The modeling of MTU passive force, moment arm and subject-specific scaling involves a number of assumptions. A potential limitation in this study is that the scaling factor for the variable moment arms was based on the assumption of the linear proportionality to the volume of the index finger. A recent study suggested a multiple-dimensional scaling that scaled both phalanx lengths and thicknesses resulted in an additive effort to the approximation of the moment arms and excursion of muscles in the index finger (Kociolek and Keir, 2011). Therefore, it is reasonable to assume that the variable moment arms of muscles were proportional to the volume of the index finger in our model. The F_{mo} scaling ratio for the extrinsic muscles depends on the linear relationship with the muscle activations (Danion et al., 2002; Maier and Hepp-Reymond, 1995). However, a more precise EMG measuring technique for the individual extrinsic muscles may improve the scaling precision (Leijnse et al., 2008a,b).

The unscaled parameter, pennation angle, may affect our results. However, the angle values for the seven muscles for the index finger are very small when compared to many other muscles in the lower extremity such as the soleus and the short-head of the biceps femoris (Wickiewicz et al., 1983; Zajac, 1989). We also found that the pennation angle was insensitive to the MTUs moments

through our sensitivity analysis (Appendix A). Furthermore, we assumed that at the slack angle all the MTUs were at their respective nominal lengths and that the passive force generated by each MTU is zero. It is possible that the MTUs might produce counterbalancing forces resulting in a zero net moment at the slack angle, but considering that the muscle forces generated even at slightly stretched position are very small, our assumption of zero MTU forces at θ_{ms} is justified. During the experiment, it was difficult to be certain that the participants did not generate active forces. However, we made every effort to eliminate the data from trials in which the EMGs values were above the previously set threshold and monitored noticeable variation in the measured tip force caused by any perturbation from the muscles. Even though our analysis did not show significant differences based on the gender differences (Appendix B), factors such as hormone alterations might potentially affect the contribution to the joint stiffness (Cammarata and Dhaher, 2008).

In summary, the elasticity of the MTUs only contribute a fraction of the total stiffness at the MCP joint in the hand and the majority of the joint stiffness is a result of the passive properties of the CLC. Based on the results from this paper, the studies that assume that the MTUs are the sole contributors to the joint stiffness may have to be updated. The results of this study may lead to updated designs of joint implants, and are also important for the identification and treatment of hand injuries and joint defects. The identification of the critical role of CLC in defining joint stiffness may lead to improvements in the computational models of the hand and also to guidelines for the design of artificial hands. Further study is needed to understand the roles of the passive stiffness from MTUs and CLC, and active stiffness due to muscle co-contractions in hand movement control.

Chapter 3

Damping Identification and Interpretation of the Energy Dissipation at the Metacarpophalangeal Joint of the Index Finger

3.1 Introduction

Passive damping has been shown to be essential to stabilize the active control of limb motions (Gielen and Houk, 1984; Esteki and Mansour, 1996; Wu et al., 1990). Understanding its role during limb movements is critical for clinical diagnoses (Lee et al., 2004; Hsieh et al., 2010; Oatis et al., 2013), physical rehabilitation (Oatis, 1993; Page, 2012), biomechanical modeling (Amankwah et al., 2004; Deshpande et al., 2012) and design of robotic devices (Carpino et al., 2011; Laffranchi et al., 2011). Passive damping is a broad concept to describe the energy dissipation without muscle contractions or stretch reflexes in synovial joints (Zatsiorsky, 1997).

Most studies have attributed passive damping solely to viscosity while ignoring other damping effects (Wright and Johns, 1961). However, damping is a result of tissue viscosity, internal friction due to structural deformation or relative surface motion (Gleghorn and Bonassar, 2008), and thixotropic fluids in joint complex. So there is a need for development of more sophisticated models of passive damping in human hand movements where low inertia of phalanges lead to dominant damping effects.

To date, the viscous damping of articular joints is modeled as a linear function of velocity

through the empirical studies (Hsieh et al., 2010; Lee et al., 2004; Halaki et al., 2006; Nordez et al., 2009b). The small oscillation technique (McFaull and Lamontagne, 1998a; Hayes and Hatze, 1977) or the forced vibration (Hsieh et al., 2010; Lee et al., 2004, 2008) which assume the articular joint to be a second-order linear system are often used to derive the linear damping through the logarithmic decrements or phase lags between cyclic input and forced output. On the other hand, the hysteresis method is also used to capture the dissipated energy phenomenon during the cyclic loading (Esteki and Mansour, 1996; Nordez et al., 2008; Heger et al., 2012). Fitting the loss factor (dissipative energy divided by storing energy) with respect to the angular velocity, the viscosity can be estimated (Nordez et al., 2008; Esteki and Mansour, 1996). A study suggested that the viscosity at the knee joint was linearly dependent on the angular velocity (Nordez et al., 2008). The authors further indicated that the solid friction may be more effective for the energy dissipation than the viscosity due to insensitivity of the velocity (Nordez et al., 2009b). Some nonlinear damping behaviors are from the different joint studies (Esteki and Mansour, 1996; Hatze, 1975; Hayes and Hatze, 1977; Amankwah et al., 2004; Heger et al., 2012). A polynomial function of the joint angle at the elbow, shoulder, and knee (Hatze, 1975; Hayes and Hatze, 1977; Engin, 1984; McFaull and Lamontagne, 1998b), and a power function of the angular velocity at the spine and metacarpophalangeal joint of the index finger are used to describe the viscous damping (Amankwah et al., 2004; Esteki and Mansour, 1996). The results of identified damping vary from joint to joint, and cannot be directly compared. Still most studies assume the damping coefficients to be a constant, and ignore the nonlinear dependency of the damping on the limb position, velocity, and cyclic frequency, and in turn ignore the effects of different damping types on the energy dissipation.

The cyclic frequency with which different hand motions occur greatly influences the control strategies used by the motor system (Ingram et al., 2008; Todorov and Ghahramani, 2004). If the

hand motion is based on the frequency command of desired tasks, the effect of the passive damping needs to be investigated from the spontaneously harmonic motion instead of using the constant velocity motion as a test load. Harmonic loading, often used in the studies of viscoelastic behavior of biological tissues in vitro (Bonifasi-Lista et al., 2005; Lakes, 2009), should be used in the damping study since there are various soft tissues spanning the articular joint. In our study, we carried out harmonic loading test at different frequencies at wide ranges of motion in order to investigate the nonlinear passive damping at the MCP joint.

The aims of this study were to identify the dependency of the passive damping of the MCP joint on the joint angle, angular velocity, and cyclic frequency of harmonic motion, and to determine the contribution of damping types such as frictional, structural, and thixotropic effect in addition to viscous damping, to the damping of the MCP joint. Toward these goals, we designed and built a customized mechanical device to collect the experimental data from the human subjects. We used the hysteresis method to estimate the energy dissipation, and developed nonlinear models using symbolic regression to described different damping at the MCP joint. We then decomposed the nonlinear models using principal component analysis (PCA) in order to separate and interpret effects of various damping types.

3.2 Methods

3.2.1 Human Subjects

A total of 19 right-handed subjects (9 males and 10 females) with mean (st) age = 24 ± 5.31, and with no history of hand injuries or musculoskeletal disorders, participated in the study. We measured the anthropometric parameters of index fingers to calculate the inertia of the index finger for the dynamic model. We calculated the finger segment weight by multiplying volume with density

of the human hand soft tissue 1.16 g/cm^3 (Chaffin et al., 2006). It is assumed that the shape of the finger segment is an uniform rectangular shape with rectangular cross-section and the center of mass is at the midpoint of each segment. The average inertia of the index finger for 19 subjects was $6.14 \times 10^{-5}\ Kg \cdot m^2$, which was fairly small compared with viscoelastic effects (Table 3.1).

Table 3.1: Statistical results of anthropometric measurements based on the gender.

Gender (Unit)	Age (year)	Weight (Kg)	Height (cm)	Finger Volume (m^3)	Finger length (m)	Finger mass (Kg)	Moment of inertia ($Kg \cdot m^2$)
M(n=9)	23.11(4.88)	69.05(4.91)	169.01(10.12)	$2.07 \times 10^{-5}(2.39 \times 10^{-6})$	0.096(0.007)	0.024(0.003)	$7.54 \times 10^{-5}(1.86 \times 10^{-5})$
F(n=10)	24.80(5.81)	58.06(7.62)	168.59(4.22)	$1.48 \times 10^{-5}(1.71 \times 10^{-6})$	0.092(0.002)	0.017(0.002)	$4.88 \times 10^{-5}(7.34 \times 10^{-6})$

3.2.2 Experimental Setup

A custom-design mechanism integrating with a motion capture system (Vicon Inc.) was used to collect the passive tip force and kinematic data of the MCP joint (Kuo et al., 2011). 18 reflective markers (diameter: 4.17 mm) were used to collect the three-dimensional kinematic data of the MCP joint during the experiment in order to precisely determine the MCP joint angle during movements (Halvorsen et al., 1999). Four wireless electromyographic sensors were attached on the subjects flexor digitorum superficialis (FDS), extensor digitorum communis (EDC), biceps and triceps to monitor muscle activations (Trigno, DelSys, Inc.).

3.2.3 Signal Processing

We normalized the EMG signals of each muscle by measuring the EMG signals from the maximal voluntary isometric contraction test before proceeding with the experiment. We processed the raw EMG signals with a $4th$ order bandpass Butterworth filter ($20 \sim 500$ Hz), performed full-wave rectification, and then passed it through a low pass filter with a cut-off frequency of 5 Hz to derive the linear envelop EMGs. We adopted the average of the linear envelop EMG as 100% effort of muscle activations. The data from a trial was eliminated when either one of four EMG signals exceeded the thresholds with 5% of the determinations from the maximal voluntary isometric contraction test (Nordez et al., 2008).

3.2.4 Testing Procedure

Natural movement of the human hands such as reach-to-grasp tasks could reach high angular velocity over 300 $^\circ/s$ at the MCP joints (Ingram et al., 2008). The previous study only covered the velocity up to 75 $^\circ/s$ with limited range of motions (Esteki and Mansour, 1996). In our study,

we carried out a series of frequency-based experiments to generate rich angle-velocity information during passive stretch. For each subject, the index finger was passively moved in a cyclic motion while the subjects relaxed. The mechanism generated harmonic oscillations with 14 cyclic frequencies based on each subject's range of motion of the index finger. Each cyclic trial maintained for 40 seconds, and the range of motion was estimated from the static test (Kuo and Deshpande, 2012). The subjects were given ample time to relax between each trial. The desired frequency range was set from $0.1 \sim 0.8$ Hz. Table 3.2 shows the actual driving frequencies among the subjects. The advantage of using the sinusoidal motion of various frequencies, instead of constant velocity, was to generate a wide range of instant angular velocity through whole range of the finger position. For the state-mapping purpose in this study, the rich angle-velocity data ensured that the fitting model extrapolated the damping behavior in the state space as much as possible (Fig. 3.1).

Table 3.2: Means and standard deviations (Mean(SD)) of 14 driving frequency levels for 19 subjects.

Level	1	2	3	4	5	6	7
Measured Frequency	0.094 (0.0054)	0.123(0.037)	0.198(0.037)	0.254(0.022)	0.3044(0.022)	0.3484(0.046)	0.436(0.042)
Level	8	9	10	11	12	13	14
Measured Frequency	0.514(0.046)	0.577(0.037)	0.623(0.034)	0.667(0.044)	0.709(0.038)	0.756(0.043)	0.797(0.042)

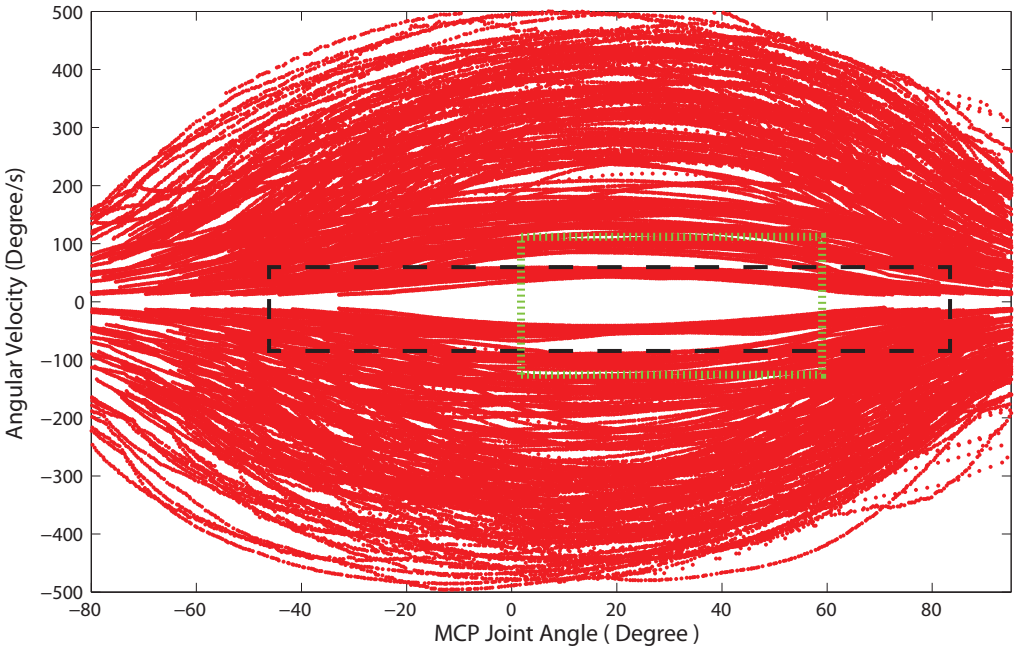

Figure 3.1: The kinematic coverage of cyclic tests for 19 subjects. The experiment design (red color envelopes) can cover larger angle-velocity domains compared with the black and green color rectangle which represents the study from (Esteki and Mansour, 1996) and (Nordez et al., 2008) respectively. Most of subjects can reach over 170° rang of motion of the MCP joint and the maximal angular velocities can reach to $500°/s$ at the mid range of motion.

3.2.5 Data Analysis for Energy Dissipation

Energy dissipation method is one of many ways to investigate the damping without considering the elasticity (Lakes, 2009; Findley and Davis, 2011). The area within the hysteresis loop of the viscoelastic moment represents an energy dissipation due to the internal friction, structural, fluid, and viscous damping. We derived the energy dissipation by determining the loading and unloading path per cycle based on the direction of angular velocity.

$$\tau_{VE} = \tau_L(\theta_m, \dot{\theta}_{m_e}, f) + \tau_U(\theta_m, \dot{\theta}_{m_f}, f) \tag{3.1}$$

here, τ_{VE}, which combines the stored and dissipated capacity, is derived from the subtraction of measured torque and moment of inertia for the overall system. The stored and restituted energy component, τ_L and τ_U, is the upper and lower bound of the hysteresis loop divided by the angular velocity in extension ($\dot{\theta}_{m_e} < 0$) and flexion direction ($\dot{\theta}_{m_f} > 0$). The instant specific energy dissipation capacity (ψ_i) defined by the instant energy loss (ΔE_{D_i}) between loading and unloading moment was estimated by using the trapezoidal numerical integration for each increment (i) of the joint angle.

$$\psi_i = \frac{\Delta E_{D_i}}{E_{L_i}} \quad , \quad \Delta E_{D_i} = E_{L_i} - E_{U_i} \tag{3.2}$$

We used the cumulative histogram method to collect the distribution of processed ψ_i data at the angle and velocity domain with $n = 1000$ samples of counting bin numbers at each frequency. Therefore, there were 14000 post-processed samples for each subject. We also calculated the overall energy dissipation capacity ($\sum_{i=1}^{i=n} \psi_i$) at each frequency for the comparison with other exiting models.

3.2.6 Damping Modeling and Interpretation

In this study we developed a damping model which can describe the energy dissipation coefficient for each subject precisely. We also reduce the model dimensions to interpret the damping behavior of truncated models by using PCA.

3.2.6.1 Symbolic regression

The specific energy dissipation capacity was hypothesized to which different damping types might contribute in cyclic loading. Some classic forms of damping coefficients were well exhibited in the linear system (De Silva, 2007). In order to investigate any possible combinations with the

composite variables which implied different damping types, we used the symbolic regression method based on the genetic programming. A software, Eureqa, was used to analyze the data set (Nutonian, Somerville, MA, USA). The method was used to determine discrete representation for the physical and biomechanical study (Schmidt and Lipson, 2009; Kurse et al., 2012). A set of predefined operators, including $\{+, -, \times, ()^n, e^n, \sin, \cos, ||\}$, was defined as a symbolic pool for the solution search. For each subject, a set of experimental data, $\{\theta_m, \dot{\theta}_m, f, \psi_i\}$, processed from the previous section was divided into a training and a validation set (60% and 40%) for the cross validation. Coefficient of determination (R^2), correlation coefficient (R), and mean square error (MSE) were used as criteria of the goodness-of-fit.

3.2.6.2 Model reduction

After the symbolic regression, we derived 19 explicit forms of energy dissipation model based on the diverse experimental data from 19 subjects. Each model described the specific energy dissipation coefficient for the corresponding subject. For the purpose of understanding the generic phenomenon of underlying damping types and control applications, we need to simplify the models so that we can interpret their common damping features by reducing the model dimensions.

PCA is a method of model decomposition and reduction which assumes that the principal components are linear combinations of aggregated variables (Jolliffe, 2005). It transforms the variables to lower dimensions based on the variances of overall variables (Fig. 3.2). Since each model derived from the symbolic regression was a linear combination of numerous terms, we assumed that each term including its coefficient is an individual function. For instance, there was a linear combination of m terms in a model, we calculated the covariance matrix ($m \times m$) for the functional set by fitting the original data, $\{\theta_m, \dot{\theta}_m, f\}$. The eigenvalue ($\lambda_k$) of the covariance matrix is the variance

of overall terms that projects on the k principal axis. A larger eigenvalue of the PC represents a better explanation of overall data. The most common method to determine the retained numbers of the PCs is to calculate the ratio of added eigenvalues and the summation of the eigenvalues shown below:

$$R^2 = \frac{\lambda_1 + \lambda_2 + \lambda_3 + ...\lambda_n}{\lambda_1 + \lambda_2 + \lambda_3 + ...\lambda_m} > q \tag{3.3}$$

where the explanation R^2 is usually set to be larger than $q = 75\%$ in general. In the study, we selected the PC numbers which explained over 90% of the variance in the data. Therefore, the model can be reconstructed without loosing important features through the process of dimensional reduction. However, the PCs do not have any physical meaning except that they construct a variance structure of overall data. To interpret the damping property of the reduced models, we aim to investigate the relationship between the PCs and the underlying physical meaning.

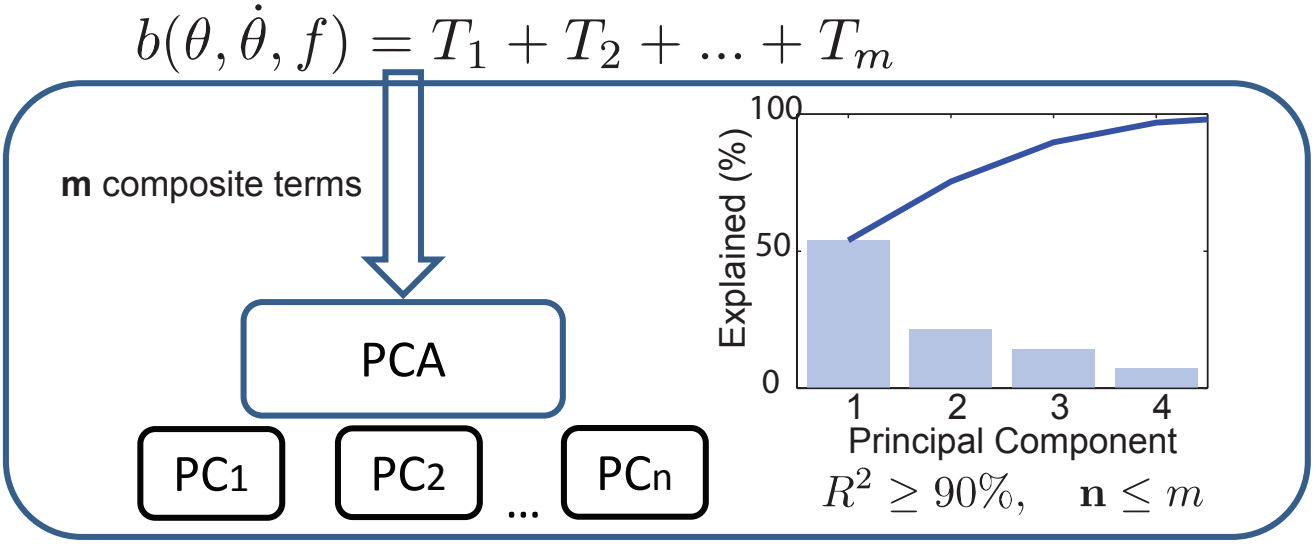

Figure 3.2: PCA for the model reduction

3.2.6.3 Model interpretation and terms selection

We used the loadings (L) which were the correlation coefficients between the underlying PCs and the composite terms to investigate the importance of each term on the selected PCs (Cadima and Jolliffe, 1995):

$$L_{mn} = a_{mn}\sqrt{\frac{\lambda_n}{ss_{mn}}} \tag{3.4}$$

where a_{mn} is the eigenvector for the mth term in the nth PC, λ_n is the eigenvalue/variance associated with the nth PC, and ss_{mn} is the variance of the mth terms. The loading of each term with respect to the PCs represents the importance of the term on the PCs, which leads to a good criterion to induce the correlated terms and to provide a information to interpret the physical meaning of corresponding PCs. The homogeneous damping terms can be regrouped and interpreted by investigating the loadings and the truncated PC structures.

An sensitivity analysis was carried out to determine the thresholds for the selection of loading criteria (L_{crit}) (Fig. 3.3). While increasing a loading criterion, the terms with smaller loadings were eliminated, and the PCs structure changed due to the terms elimination. We determined two indicators to prevent the model from over-reduction. We compared the reduced model with the experimental data. The root mean square error ($RMSE$) and the correlation coefficient (R) were calculated. If R was smaller than 0.8 or the $RMSE$ larger than 0.3 while we gradually increased the loading criterion, the process of discarding terms was stopped (Fig. 3.3).

The purpose of retaining terms and truncating PCs that satisfied our criteria was to the interpret the physical meaning of each potential factors based on the extrapolated terms, which led to different damping types that contributed to the energy dissipation of the articular MCP joint.

We extracted the generalized damping features which might be inherent among 19 subject-specific models from the PCA and the terms selection (Fig. 3.4).

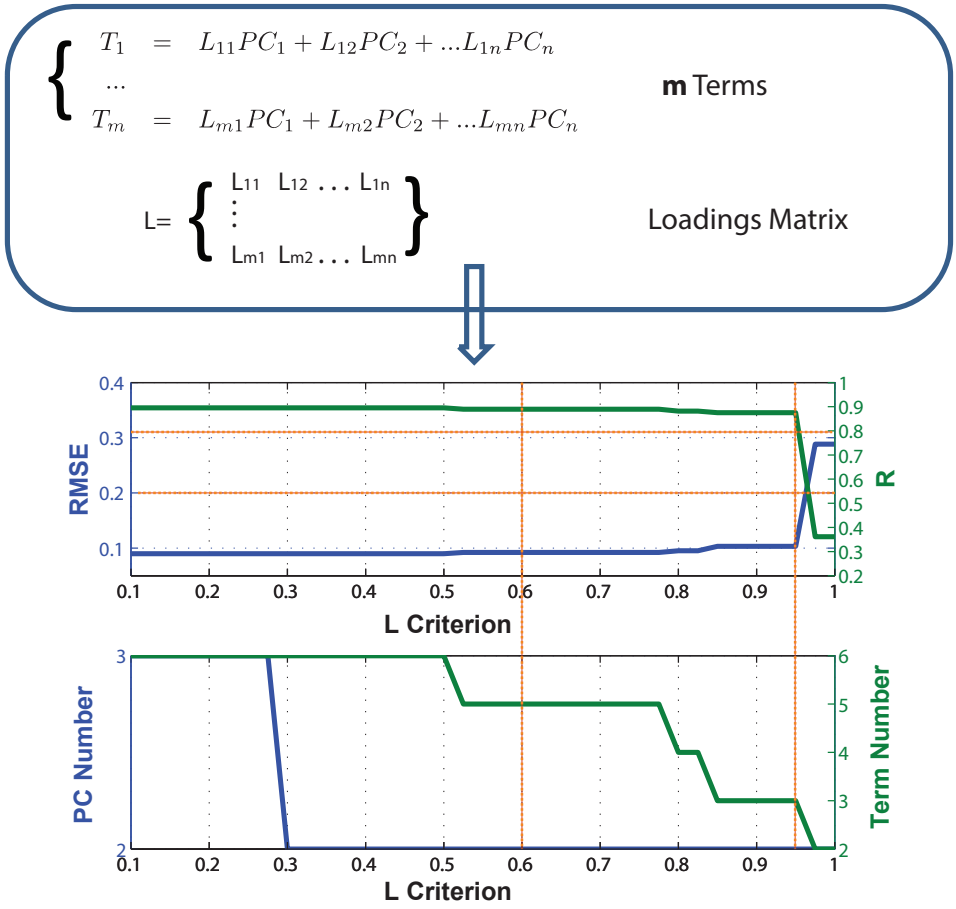

Figure 3.3: Terms selection of the simplied model based on the factorial loadings and the L criteria.

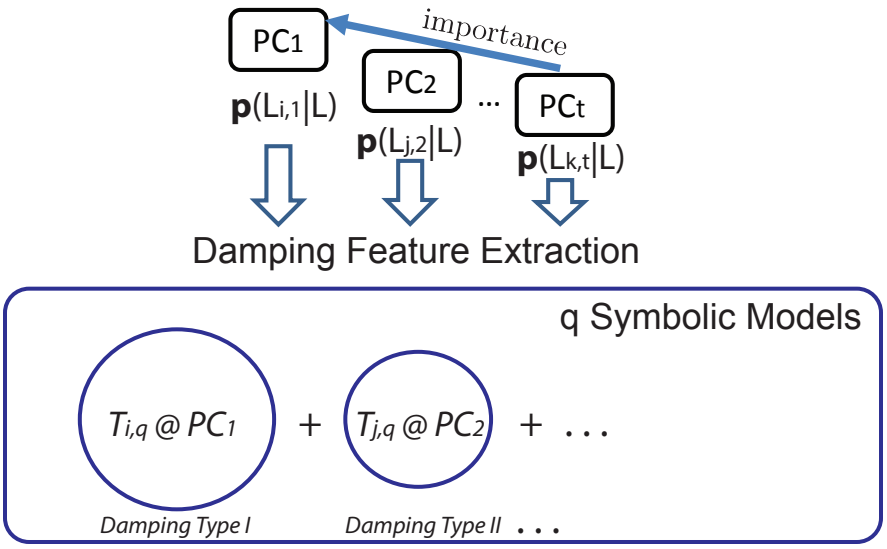

Figure 3.4: Damping extrapolation and intrepretation.

3.3 Results

3.3.1 Hysteresis Loop

We found that the harmonic distortion due to the complicated structures and soft tissues in the MCP joint gave rise to a nonlinear behavior. The results showed that the shape of hysteresis loop varied from sigmoid to elliptical curves when the frequency was increased (Fig. 3.5). It was observed qualitatively that the energy dissipation represented by the area within the loading and unloading curve, was small at lower frequencies and gradually increased following the increase of cyclic frequency. The results showed that the damping depended on the frequency. The normalized instant energy dissipative ratio (ψ_i) was used to identify the relation between the angle, velocity and frequency.

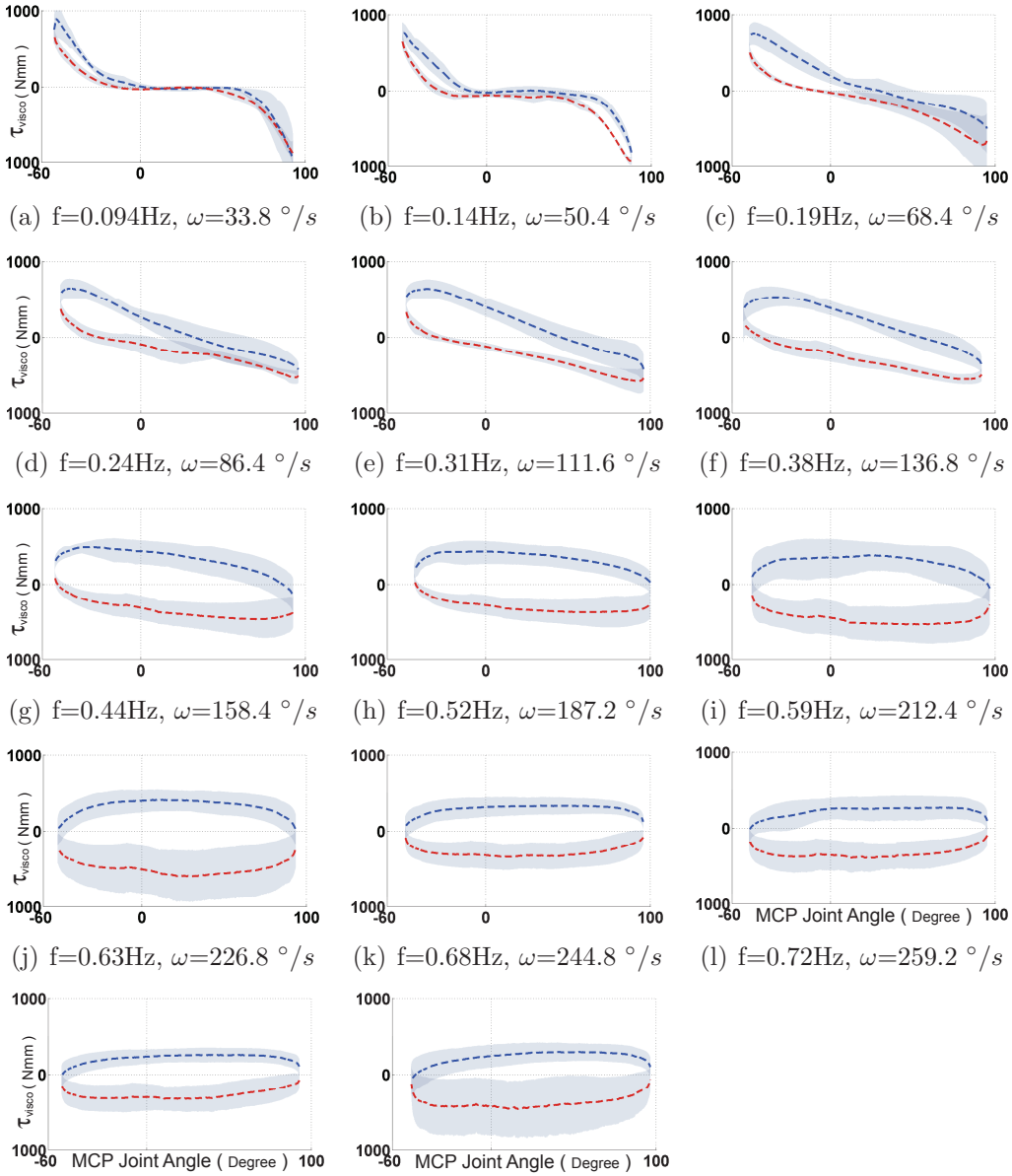

(a) f=0.094Hz, ω=33.8 °/s (b) f=0.14Hz, ω=50.4 °/s (c) f=0.19Hz, ω=68.4 °/s

(d) f=0.24Hz, ω=86.4 °/s (e) f=0.31Hz, ω=111.6 °/s (f) f=0.38Hz, ω=136.8 °/s

(g) f=0.44Hz, ω=158.4 °/s (h) f=0.52Hz, ω=187.2 °/s (i) f=0.59Hz, ω=212.4 °/s

(j) f=0.63Hz, ω=226.8 °/s (k) f=0.68Hz, ω=244.8 °/s (l) f=0.72Hz, ω=259.2 °/s

(m) f=0.76Hz, ω=273.6 °/s (n) f=0.82Hz, ω=295.2 °/s

Figure 3.5: A example of the hysteresis loops of $\tau_{VE} - \theta_m$ plot (Mean±SD) at 14 frequencies for one subject. The blue and red color dashed curve demonstrates the loading and unloading average moment at the extension and flexion direction.

3.3.2 Nonlinear Damping Model

3.3.2.1 Energy dissipation model

The fitting models of the damping coefficient show good fits for 19 sets of the processed data (Table 3.3, $\overline{R^2} = 0.91 \pm 0.03$). The MSE showed the mean, $\overline{MSE} = 0.01 \pm 0.007$, for the whole fitting models and the coefficient numbers were between $5 \sim 8$. We also found that none of the fitting models were identical. However, the first order frequency, f, was mostly selected for many models (Fig. 3.6), and the second order terms such as $\dot{\theta}^2$ and f^2 were also common among the fitting models (13 and 11 out of 19 models). The linear θ appeared in about half of the fitting models.

Table 3.3: Statistical results and fitting models of the energy dissipative function for 19 subjects. R^2: Goodness-of-fit; R: Correlation coefficient; MSE: Mean square error; CN:Coefficient Number; C: Complexity

Subject	R^2	R	MSE	CN	C	Coefficient Model
1	0.92	0.91	0.011	7	35	$k_1 + k_2 f^2 + k_3\theta\dot{\theta} + k_4\dot{\theta}^2 - k_5\dot{\theta} - k_6 f - k_7 f^3$
2	0.91	0.96	0.012	8	42	$k_1 f + k_2 f^{-1} + k_3\theta\dot{\theta} + k_4\dot{\theta}^2 - k_5 - k_6\dot{\theta} - k_7\theta\dot{\theta}^2 - k_8 f^3$
3	0.93	0.94	0.007	5	37	$k_1 f + k_2\theta f - k_3 - k_4\theta^2 f - k_5 f^3$
4	0.89	0.90	0.007	8	35	$k_1 f + k_2\dot{\theta} f + k_3\theta\dot{\theta} + k_4\dot{\theta}^2 - k_5\theta - k_6\dot{\theta} - k_7\dot{\theta}^2 f - k_8\theta\dot{\theta} f$
5	0.87	0.83	0.013	8	39	$k_1 + k_2 f^2 + k_3\dot{\theta} f + k_4\theta\dot{\theta} + k_5\dot{\theta}^2 - k_6\dot{\theta} - k_7\theta - k_8 f^3$
6	0.93	0.96	0.018	6	41	$k_1 + k_2 f^2 + k_3\theta^2 + k_4\dot{\theta}^2 - k_5\theta - k_6 f$
7	0.87	0.93	0.015	6	40	$k_1 + k_2 f^{-1} + k_3 f^2 + k_4\dot{\theta}^2 + k_5\theta\dot{\theta} f - k_6 f$
8	0.91	0.94	0.016	8	32	$k_1 + k_2 f^2 + k_3\theta^2 + k_4\dot{\theta}^2 + k_5\theta\dot{\theta} - k_6\dot{\theta} - k_7\theta - k_8 f$
9	0.92	0.96	0.003	6	37	$k_1 f^2 + k_2\theta f - k_3 - k_4\dot{\theta}^2 f - k_5\theta^2 f - k_6 f^3$
10	0.83	0.92	0.008	6	39	$k_1 f^2 + k_2\theta^2 + k_3\dot{\theta}^2 - k_4 - k_5\theta - k_6\theta f$
11	0.91	0.93	0.018	7	29	$k_1 f + k_2\theta^2 + k_3\dot{\theta}^2 - k_4 - k_5\dot{\theta} - k_6\theta - k_7\dot{\theta}^2 f$
12	0.94	0.97	0.003	6	33	$k_1 f + k_2\dot{\theta}^2 f + k_3\theta\dot{\theta} f^2 - k_4 - k_5\theta - k_6\dot{\theta}^2$
13	0.93	0.92	0.034	7	32	$k_1 f + k_2\dot{\theta} + k_3 f^{-1} + k_4\dot{\theta}^2 - k_5 - k_6\theta f - k_7 f^2$
14	0.92	0.93	0.006	6	37	$k_1 + k_2 f + k_3\theta + k_4\theta^2\dot{\theta} f^4 - k_5\theta\dot{\theta} - k_6\theta^2$
15	0.93	0.86	0.003	7	35	$k_1 f + k_2\theta + k_3\theta\dot{\theta} - k_4 - k_5\theta^2 - k_6 f^2 - k_7\theta\dot{\theta} f$
16	0.91	0.94	0.005	6	43	$k_1 f + k_2\theta\dot{\theta} f + k_3\dot{\theta}^2 f^3 - k_4\dot{\theta} f - k_5\theta f - k_6\theta^2\dot{\theta}$
17	0.92	0.94	0.004	6	41	$k_1 f + k_2\theta\dot{\theta} f + k_3\dot{\theta}^2 f^2 - k_4\dot{\theta} f - k_5\theta f - k_6\theta\dot{\theta}^2$
18	0.87	0.81	0.013	6	35	$k_1 f^2 + k_2\theta f - k_3 - k_4\dot{\theta}^2 - k_5\theta^2 f - k_6 f^3$
19	0.91	0.93	0.003	7	32	$k_1 f + k_2 f^{-1} + k_3\theta\dot{\theta} + k_4\dot{\theta}^2 - k_5 - k_6\dot{\theta} - k_7 f^2$

Table 3.4: The coefficients ($k_1 ... k_8$) of the fitting models at Table 3.3.

Model	k_1	k_2	k_3	k_4	k_5	k_6	k_7	k_8
1	0.11	8.7	5.72×10^{-6}	1.67×10^{-6}	2.08×10^{-4}	1.75	8.08	
2	4.88	0.09	1.13×10^{-5}	3.3×10^{-6}	1.39	3×10^{-4}	1.06×10^{-8}	4.7
3	3.14	3.28×10^{-3}	4.5×10^{-1}	1.03×10^{-4}	3.54			
4	0.423	9.32×10^{-4}	1.35×10^{-5}	9.27×10^{-6}	7×10^{-4}	7×10^{-4}	1.13×10^{-5}	1.61×10^{-5}
5	0.04	4.04	4.28×10^{-4}	3.73×10^{-6}	2.21×10^{-6}	5.15×10^{-4}	2.17×10^{-3}	4.68
6	0.28	3.72	5.09×10^{-5}	1.12×10^{-5}	4.6×10^{-5}	1.53×10^{-3}		
7	29.96	-5.04	3.304×10^{1}	4.25×10^{-6}	8.99×10^{-6}	54.85		
8	0.27	3.39	3.64×10^{-5}	9.33×10^{-6}	7.58×10^{-6}	1.87×10^{-4}	1.49×10^{-3}	1.77
9	80.94	0.038	0.76	1.42×10^{-5}	1.2×10^{-3}	96.55		
10	1.2	6.74×10^{-6}	1.68×10^{-6}	0.0083	2.58×10^{-4}	1.34×10^{-3}		
11	0.27	1.98×10^{-5}	1.18×10^{-5}	0.028	1.94×10^{-5}	1.47×10^{-3}	1.37×10^{-5}	
12	0.31	1.14×10^{-5}	2.27×10^{-5}	0.02	4.34×10^{-5}	3.91×10^{-6}		
13	17.85	2.84×10^{-4}	0.21	4.82×10^{-6}	3.77	7.29×10^{-3}	19.02	
14	0.17	0.35	7×10^{-4}	3.12×10^{-7}	8.08×10^{-6}	3.25×10^{-5}		
15	4.96	2.94×10^{-4}	3.046×10^{-5}	0.88	4.71×10^{-5}	4.25	4.13×10^{-5}	
16	0.63	3.6×10^{-5}	1.14×10^{-5}	8.91×10^{-4}	5.62×10^{-3}	6.836×10^{-8}		
17	0.59	2.77×10^{-5}	8.65×10^{-6}	7.89×10^{-4}	4.37×10^{-3}	2.442×10^{-8}		
18	8.94	6.82×10^{-3}	0.068	2.86×10^{-6}	1.9×10^{-4}	10.2		
19	9.57	0.149	1.14×10^{-5}	3.08×10^{-6}	2.39	2.81×10^{-4}	8.15	

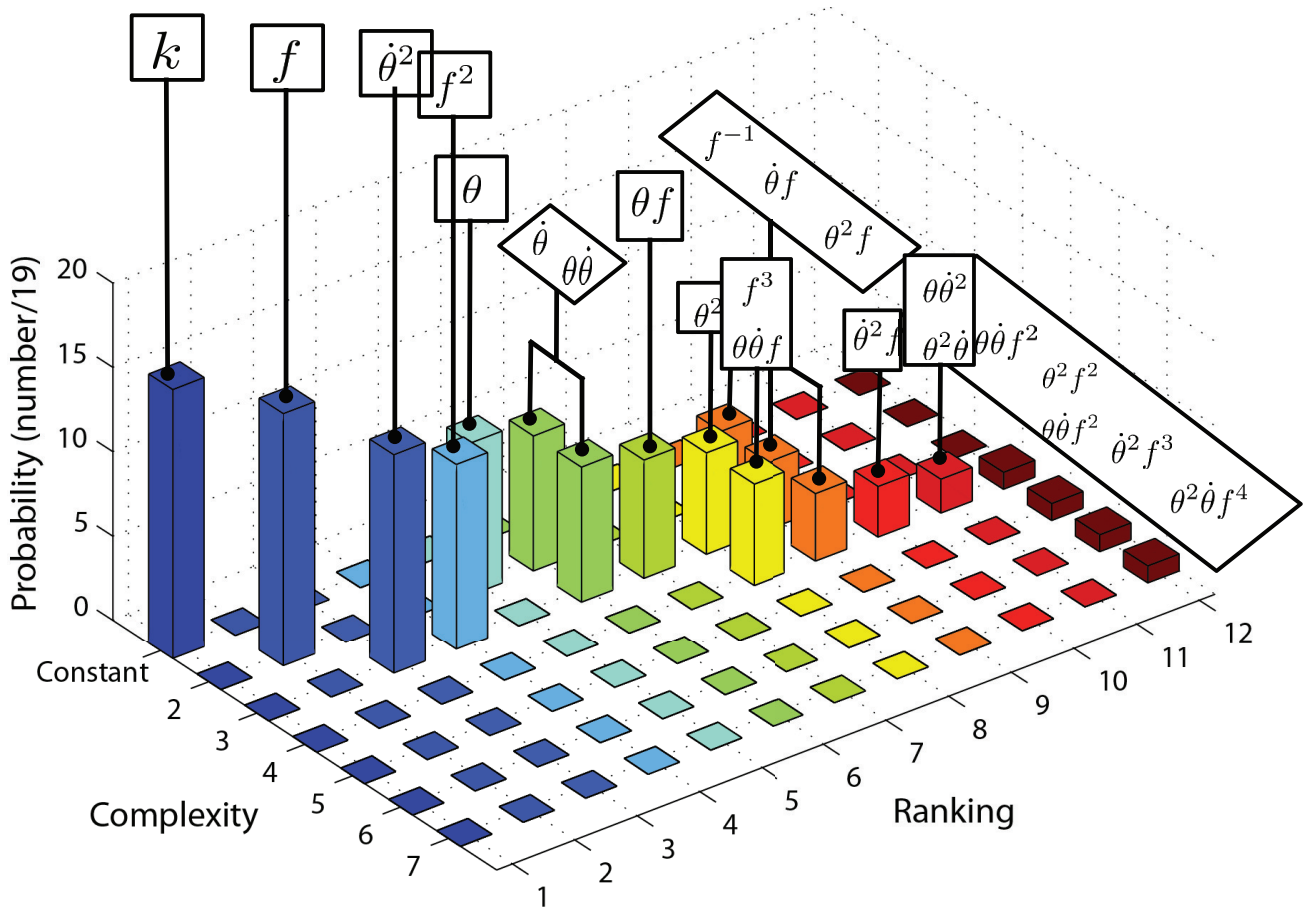

Figure 3.6: The alphabet distribution and the ranking counted among the 19 fitting models. k: constants; θ: joint angle; $\dot{\theta}$: angular velocity;f: cyclic frequency.

3.3.2.2 Model reductions with PCA

The results of PCA showed that four principal components can explain over 90% of the overall variances in average among the 19 models (Fig. 3.7). The first PC explained about 40% of the data variances in average. The results imply that three or four major PCs among the 19 models

can be selected to describe most variances at the models. The loading/correlation for each term on selected PCs was calculated for the model reduction.

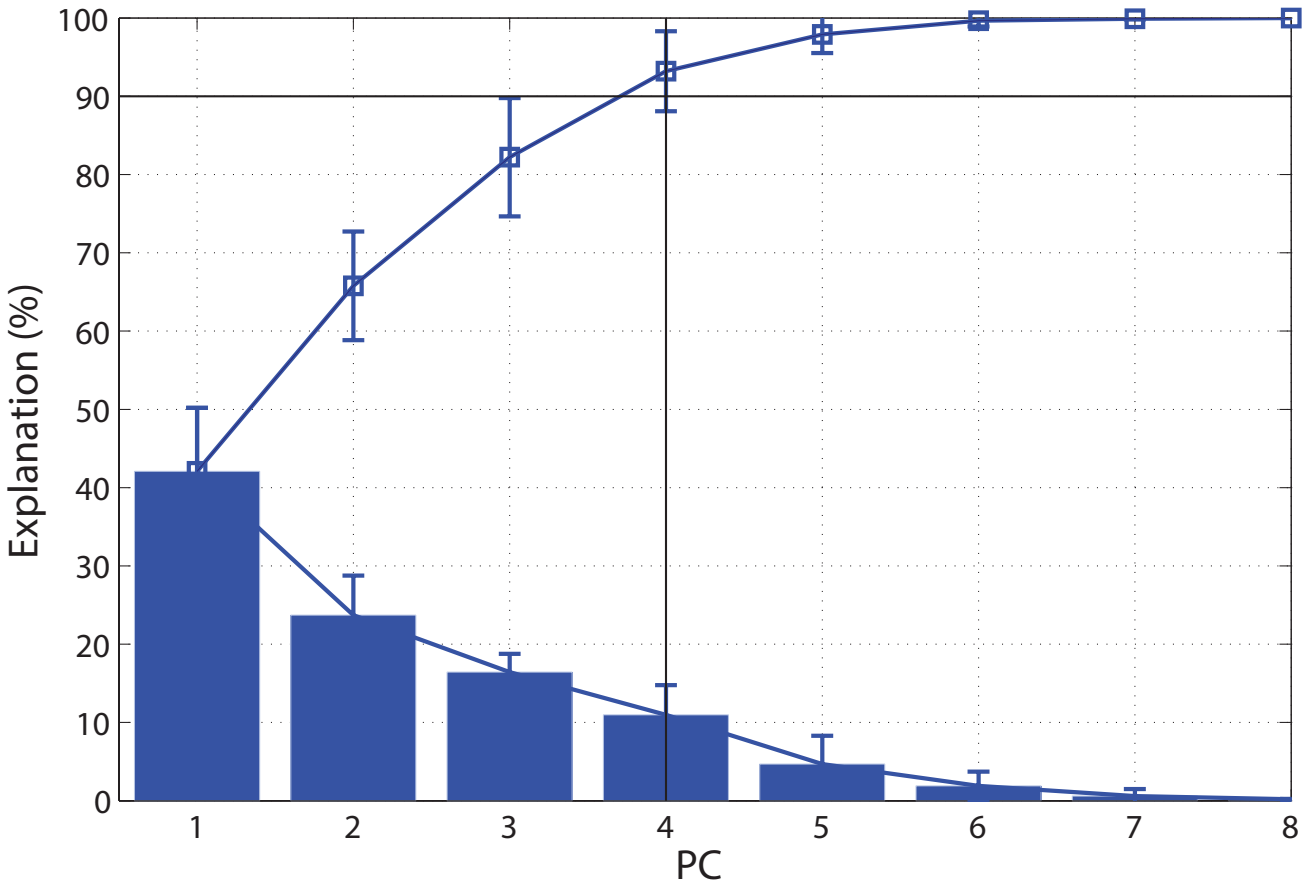

Figure 3.7: Pareto chart of the explanational percenttage of the principal components. The error-bars present the mean values and standard deivations of the variation explianation among the 19 models.and The numbers on the top of the bars shows the subject numbers whose PC numbers explains over 90% of overall variances in data.

3.3.2.3 Subset of selected terms

Fig. 3.8 demonstrates a process for retainment of the terms selection for the model one whose original model expression was:

$$b = k_1 + k_2 f^2 + k_3 \theta\dot{\theta} + k_4 \dot{\theta}^2 - k_5 \dot{\theta} - k_6 f - k_7 f^3 \tag{3.5}$$

First three PCs were able to cover 90% of variance among seven terms in this case. Given a set of loading criteria L from 0.1 to 1 with an increment 0.025, the symbolic terms and PCs number dropped at different loading criteria stages (Fig. 3.8 and Fig. 3.9). When the criterion was small ($0.2 \sim 0.4$), only the constant term with small loadings across the PCs was eliminated. Following with increased criterion, the model still contained the frequency-related terms, but eliminated the velocity-related terms. Observed from this demonstrated result, the PC numbers decreased from three to two PCs. The third PC with smaller projected variance was discarded due to the absence of the terms during the model reduction process (Fig. 3.8(e)).

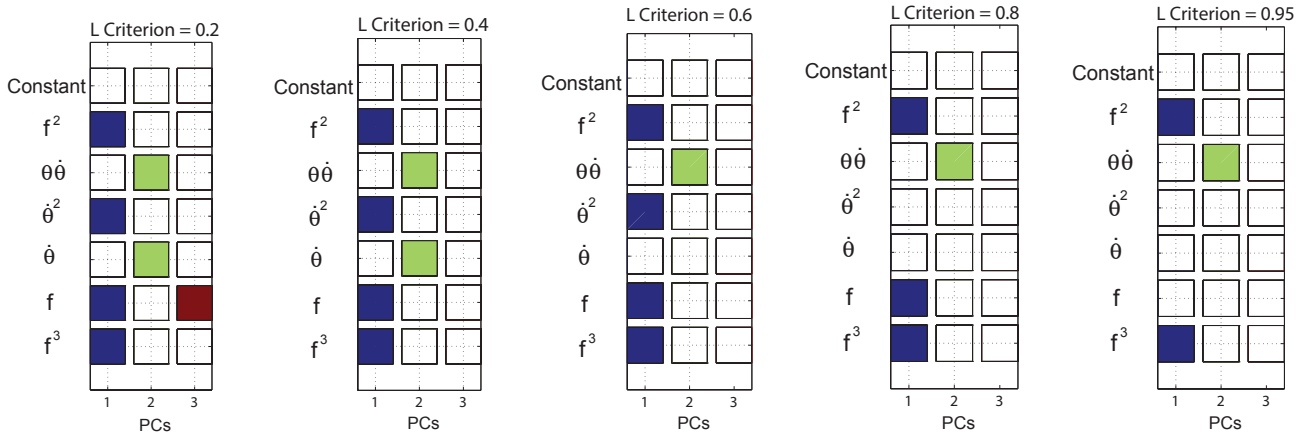

(a) R=0.9 (b) R=0.9 (c) R=0.89 (d) R=0.88 (e) R=0.88

Figure 3.8: Results of terms and PCs reduction based on the increased loading criterion. The simplified energy dissipative model for the subject model one is determined at the loading criterion $L_{crit} = 0.95$. The correlation R between the reduced model and experimental data is 0.88.

The correlation (R) gradually decreased when less terms were retained with increased loading criterion (Fig. 3.9). The R decreased drastically till the loading criterion reached over 0.95. The truncated model retained the three major terms ($\{f^2, \theta\dot{\theta}, f^3\}$) whose loadings were higher than 0.95 and the correlation R between the model and experimental result was 0.88. This implied that the subset of selected terms still highly correlated with the original PCs, and did not overly distort the PCs structure.

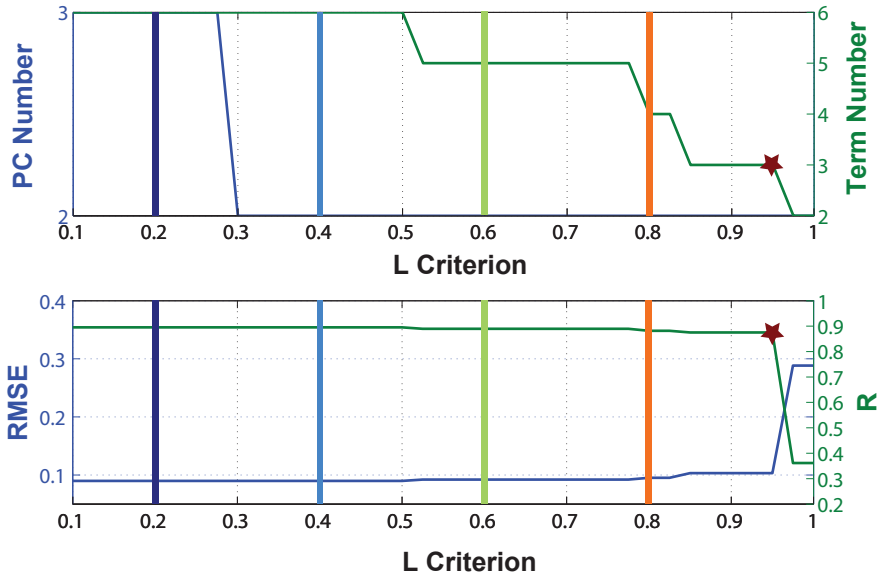

Figure 3.9: Process of the model reduction and terms selection by using the loading criteria (Subject 1). The RMSE and R were used to monitor the goodness-of-fit of the truncated PCs.

Therefore, the truncation of the model which included two PCs and three retained terms was expressed as:

$$b_t = (k_1 f^2 - k_7 f^3)_{pc1} + (k_3 \theta\dot{\theta})_{pc2} \tag{3.6}$$

here, the first and second term f^2 and f^3 constituted a major feature at the first PC, and the last $\theta\dot{\theta}$ represented another damping feature at the second PC. We reduced the symbolic model (seven terms) to a compact model (three terms) with the interpretation.

3.3.2.4 Damping types

Fig. 3.10 shows the results of final term selections and statistics for 19 models. Each block presented the composite terms originally and its final retained terms at each corresponding PCs

based on different loading criteria.

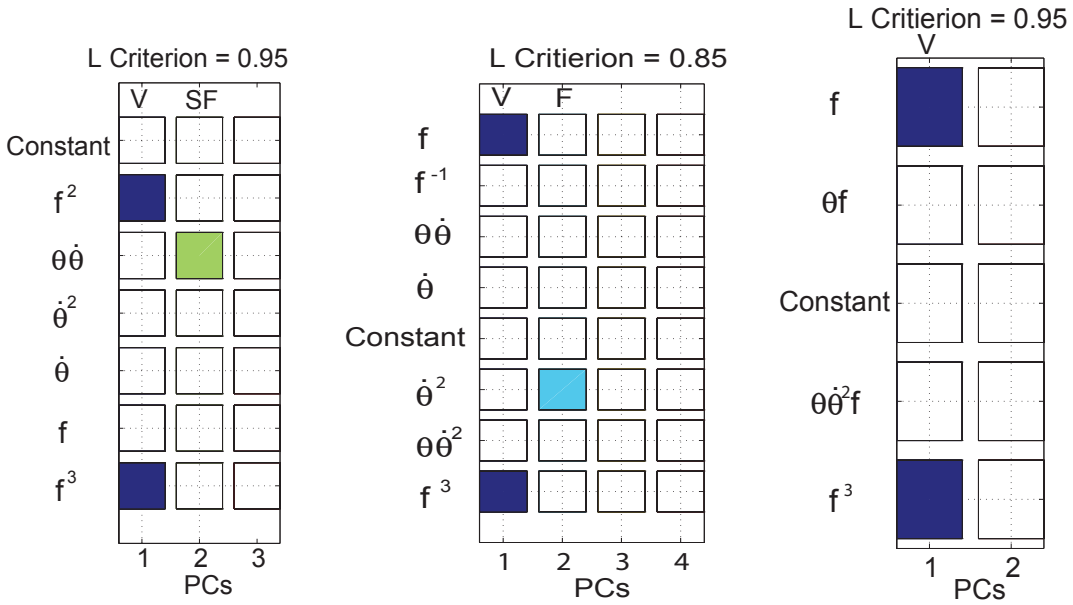

(a) Model one: $RMSE = 0.1$ and $R = 0.88$

(b) Model two: $RMSE = 0.21$ and $R = 0.84$

(c) Model three: $RMSE = 0.14$ and $R = 0.81$

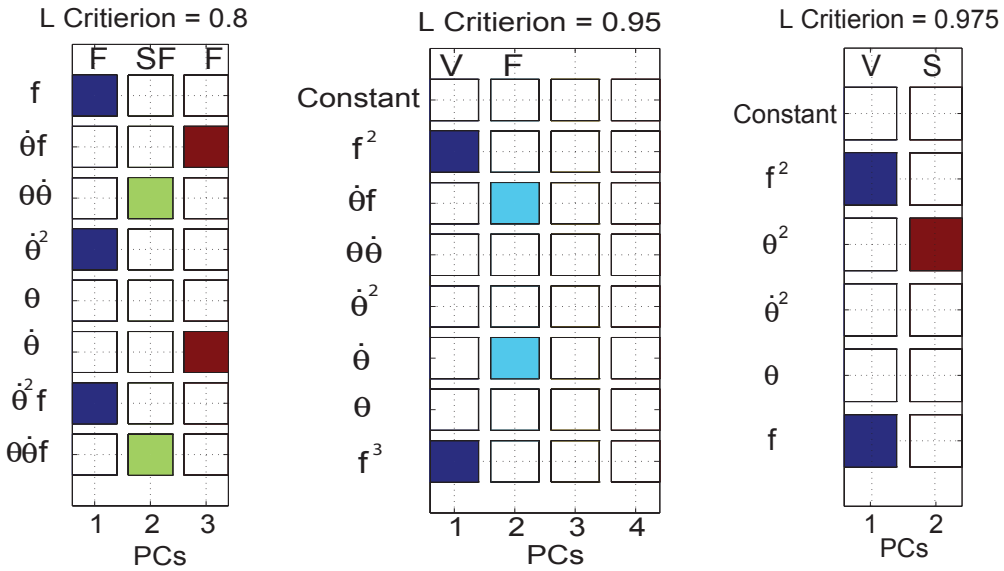

(d) Model four: $RMSE = 0.16$ and $R = 0.85$

(e) Model five: $RMSE = 0.19$ and $R = 0.87$

(f) Model six: $RMSE = 0.23$ and $R = 0.84$

Figure 3.10: Results of the terms extrpolation from 19 subjective models. We categoried the damping feature at each corresponding PCs as: **V**= viscous, **F**= fluid-like, **S**= structral, and **SF**= structral-fluid.

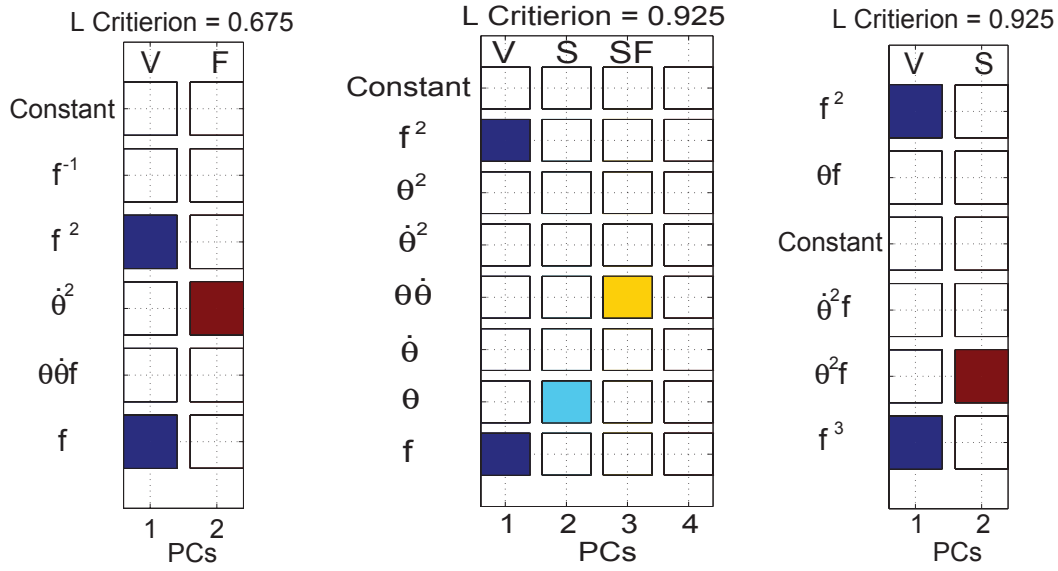

(a) Model seven: $RMSE = 0.17$ and $R = 0.87$

(b) Model eight: $RMSE = 0.17$ and $R = 0.85$

(c) Model nine: $RMSE = 0.18$ and $R = 0.81$

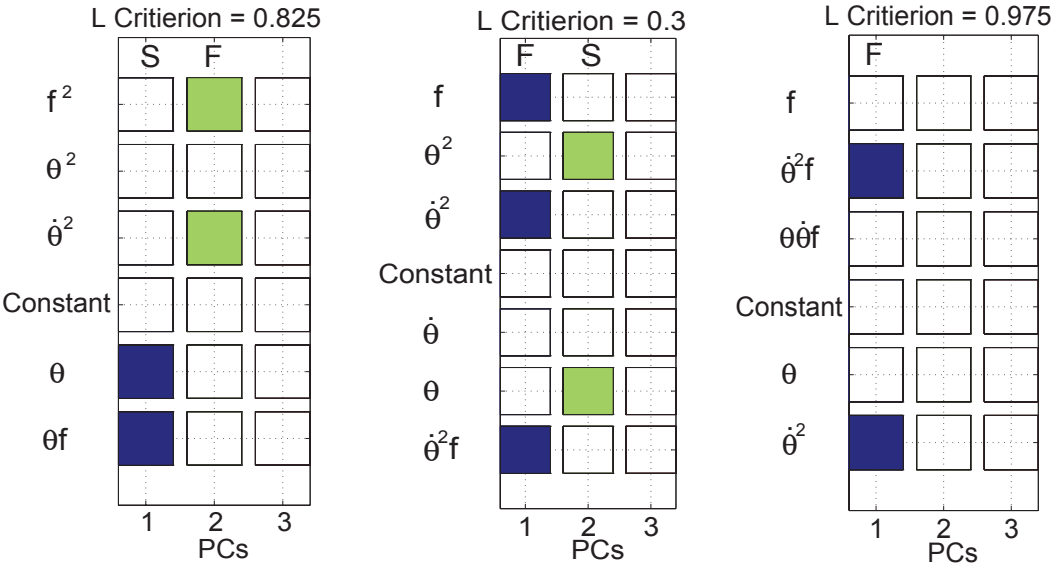

(d) Model ten: $RMSE = 0.28$ and $R = 0.87$

(e) Model eleven: $RMSE = 0.13$ and $R = 0.82$

(f) Model twelve: $RMSE = 0.19$ and $R = 0.83$

Figure 3.10 (Continued)

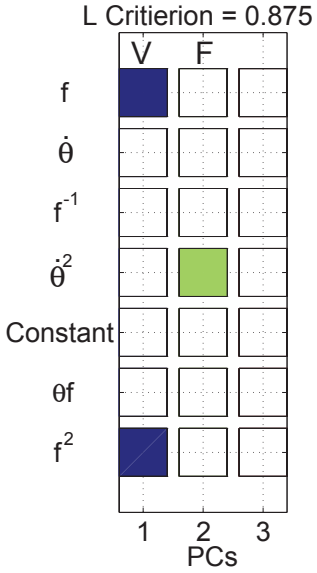

(g) Model thirteen: $RMSE = 0.21$ and $R = 0.80$

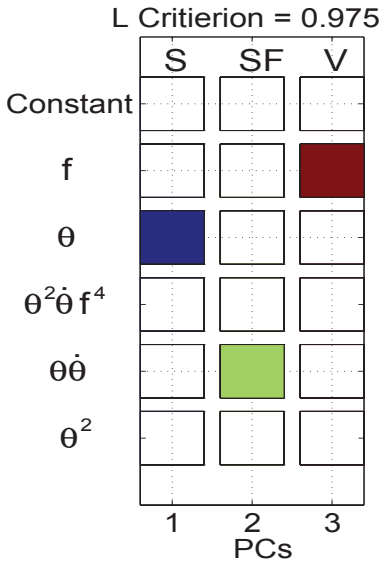

(h) Model fourteen: $RMSE = 0.12$ and $R = 0.83$

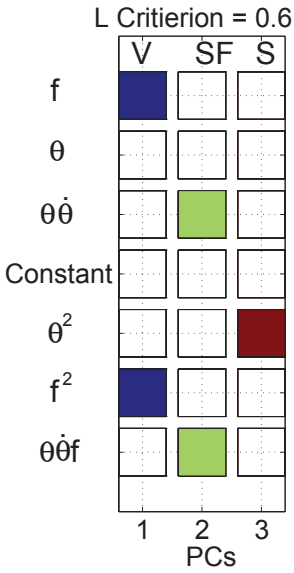

(i) Model fifteen: $RMSE = 0.13$ and $R = 0.83$

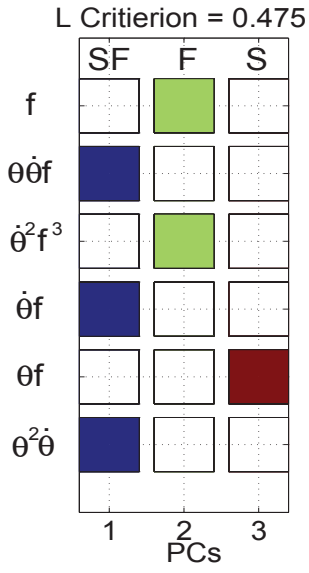

(j) Model sixteen: $RMSE = 0.20$ and $R = 0.81$

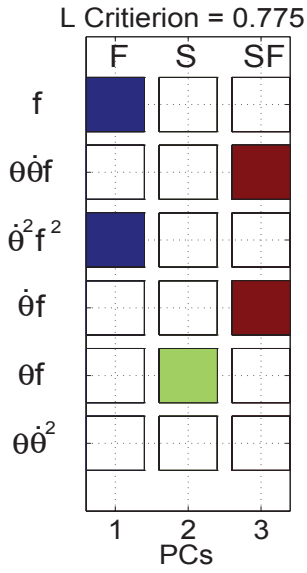

(k) Model seventeen: $RMSE = 0.07$ and $R = 0.94$

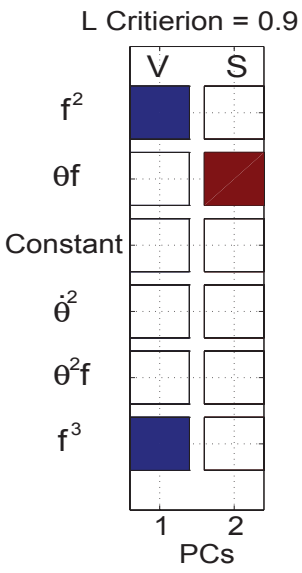

(l) Model eighteen: $RMSE = 0.15$ and $R = 0.81$

Figure 3.10 (Continued)

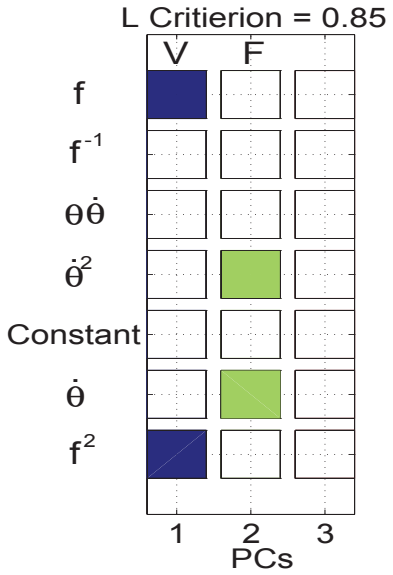

(m) Model nineteen: $RMSE = 0.16$ and $R = 0.86$

Figure 3.10 (Continued)

- Viscous damping (**V**): The first major feature was the frequency dependent damping which implied the energy dissipation due to the viscosity of the soft tissues. We found that 13 models presented this damping type at the first PCs (12) and the third PC (one) which depended on the polynomial combination of frequency terms. We demonstrated the viscous feature assuming that the viscous damping torque was proportional to the angular velocity (Fig. 3.11).

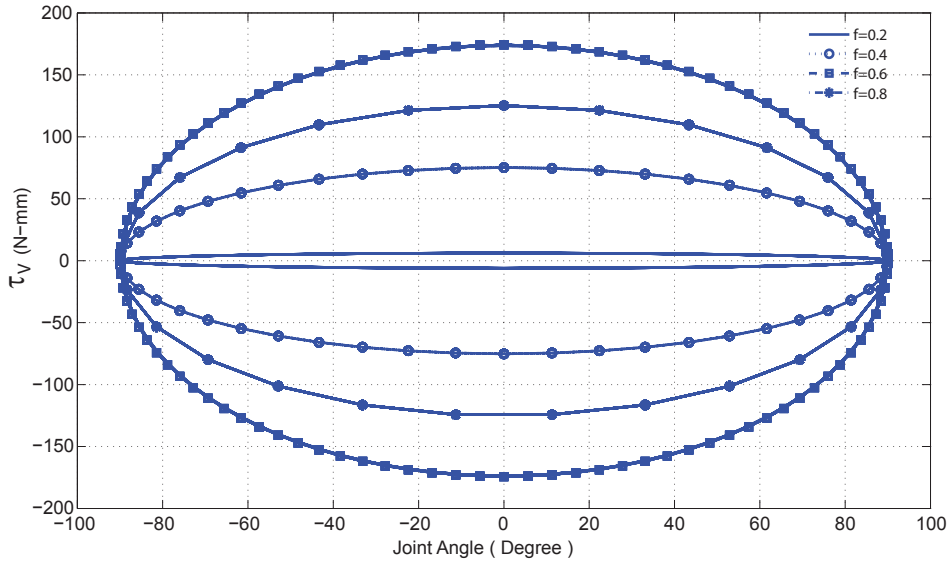

(n) Viscous Damping v.s. θ

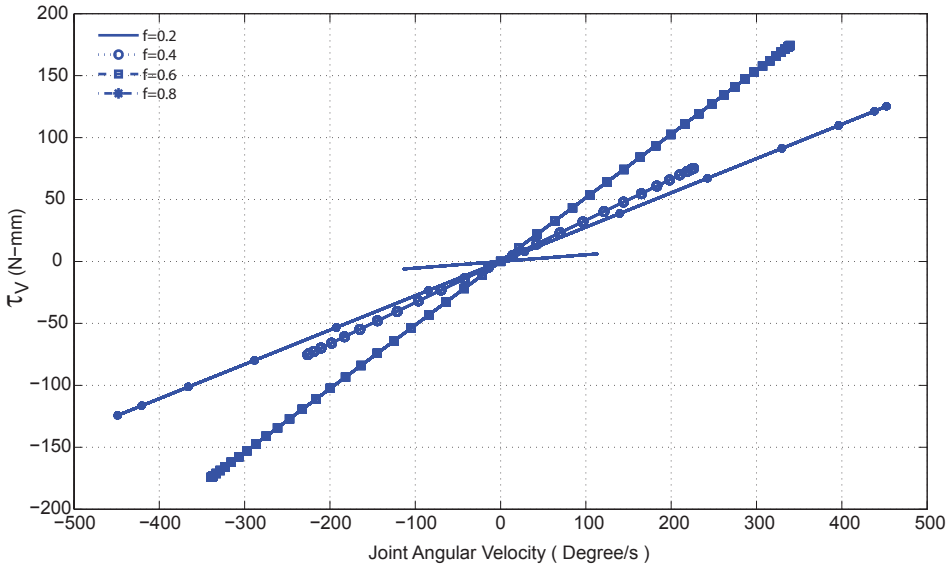

(o) Viscous Damping v.s. ω

Figure 3.11: Demonstrated viscous damping torque with respect to the angle and angular velocity. The first feature is oberved in the 13 models $\{1, 2, 3, 5, 6, 7, 8, 9, 13, 15, 18, 19\}_{pc1}$ and $\{14\}_{pc3}$.

- Fluid-like damping (**F**): We found that the secondary feature which interpreted from the eleven models was velocity dependent term. Most of the models in this category showed the feature at the second PC (ten). Although the velocity dependent terms usually coupled with the frequency, the velocity terms with higher orders dominated the corresponding PCs, leading to the similarity of the energy dissipation function. We assumed that the fluid-like damping torque was proportional to the angular velocity. Fig. 3.12 shows a demonstrated patterns of fluid-like damping torque due to different cyclic frequencies.

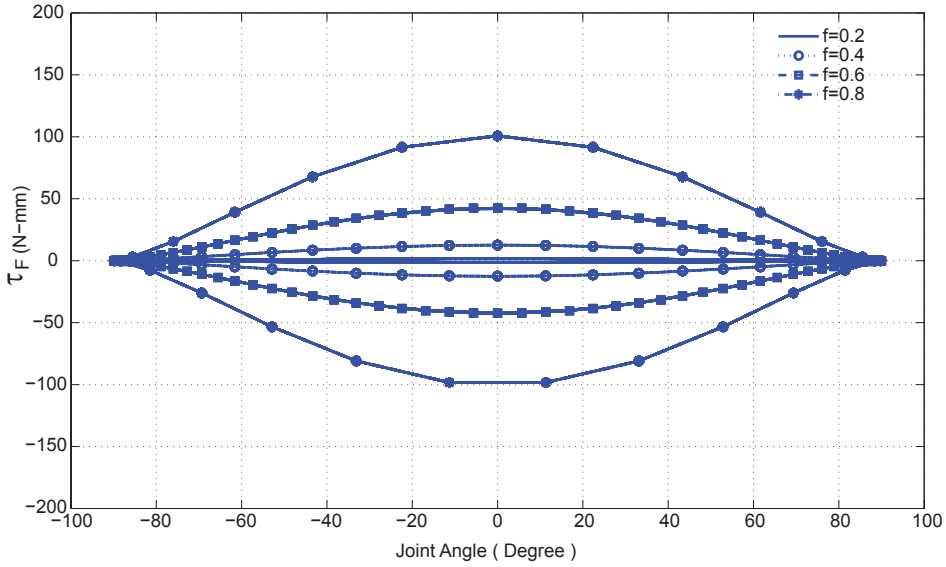

(a) Fluid Damping v.s. θ

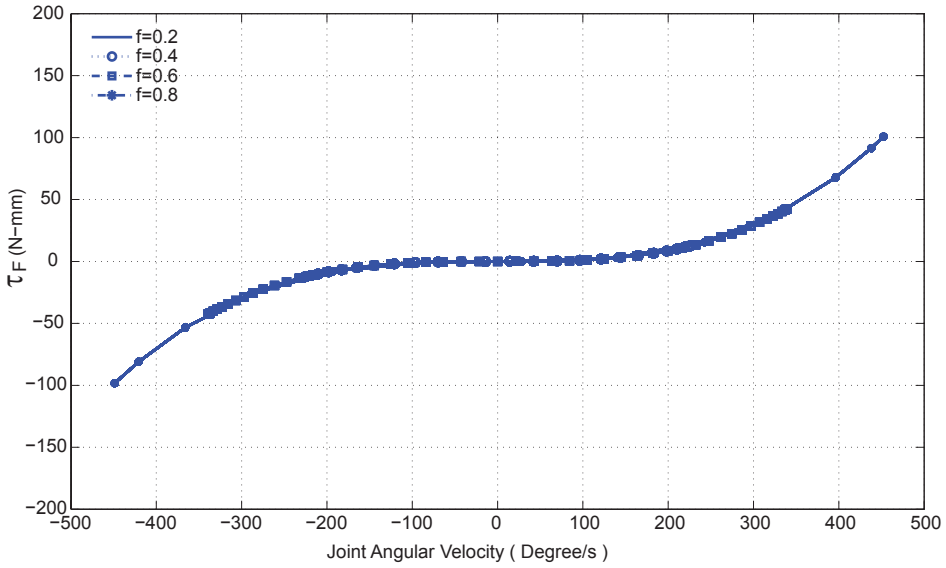

(b) Fluid Damping v.s. ω

Figure 3.12: Demonstrated fluid-like damping torque with respect to the angle and angular velocity. The second feature oberved in eleven models ($\{2, 5, 7, 10, 11, 12, 13, 16, 17, 19\}_{pc2}$ and $\{4\}_{pc1,pc3}$).

- Structural damping (**S**): The third feature depended on the joint angle which was related to the friction caused by the deformed soft tissues and joint configuration. We found that eleven models showed the structural damping behavior at the first PCs (two), second PCs (seven), and the third PCs (two). Similar with the fluid-like damping, the forms of the structural damping also coupled with the frequency. The structural damping was assumed to be proportional to the signum function. Fig. 3.13 demonstrated a general structural damping with different frequency levels. We found that although the energy dissipation was smaller than the other types, the hysteresis loop in Fig. 3.13 distinguished the damping effect between the structural and the other damping types.

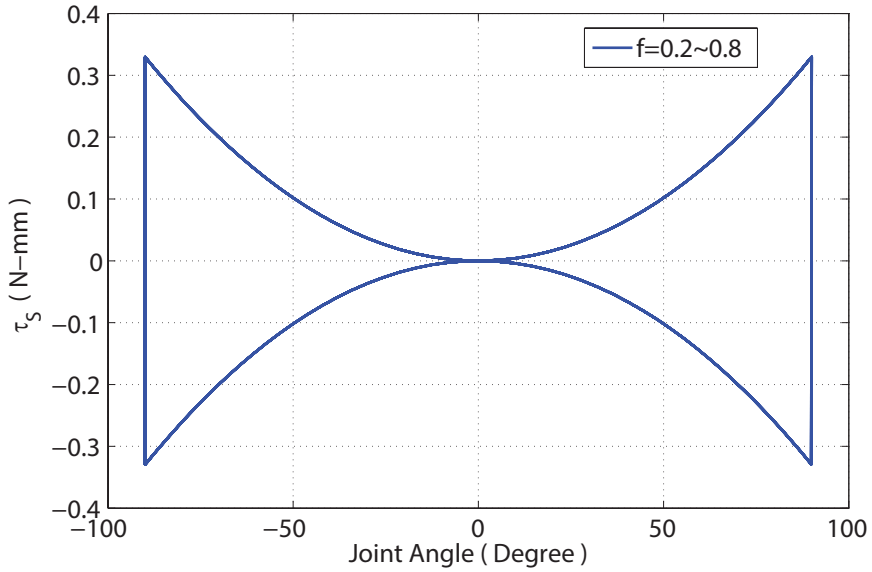

(a) Structural Damping v.s. θ

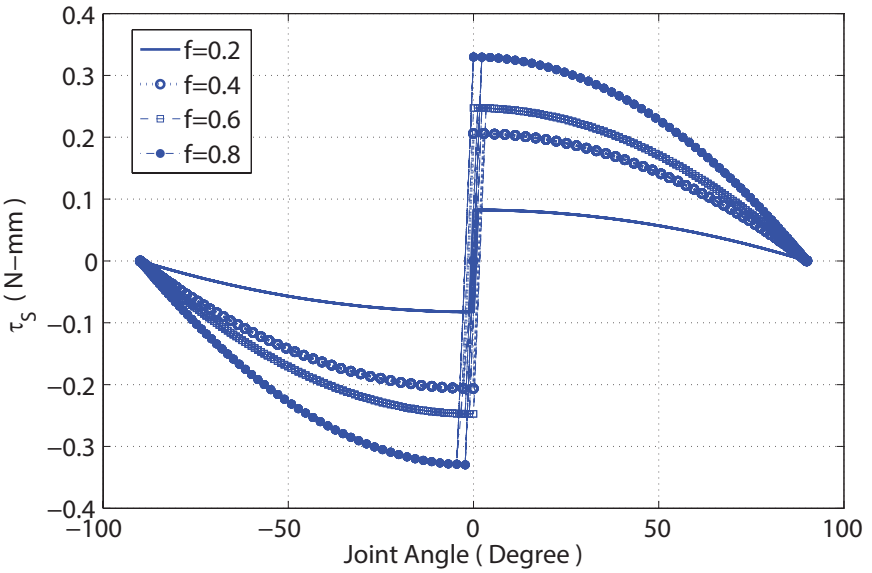

(b) Structural Damping v.s. ω

Figure 3.13: Demonstrated structural damping torque with respect to the angle and angular velocity. The third feature is oberved from the eleven models ($\{2, 6, 8, 9, 11, 12, 17, 18\}_{pc2}$, $\{10, 14\}_{pc1}$, and $\{15, 16\}_{pc3}$).

- Structural-fluid damping (**SF**): We also found another type of damping which implied the interference between the tissue deformation and the synovial fluid in the joint. Seven models presented this damping type at the first PC (one), the second PCs (five), and the third PC (one). The angle, velocity, and frequency term appeared in various coupling forms but led to the similar function of energy dissipation. The damping behavior was similar with the structural damping, but represented the lubrication in the MCP joint.

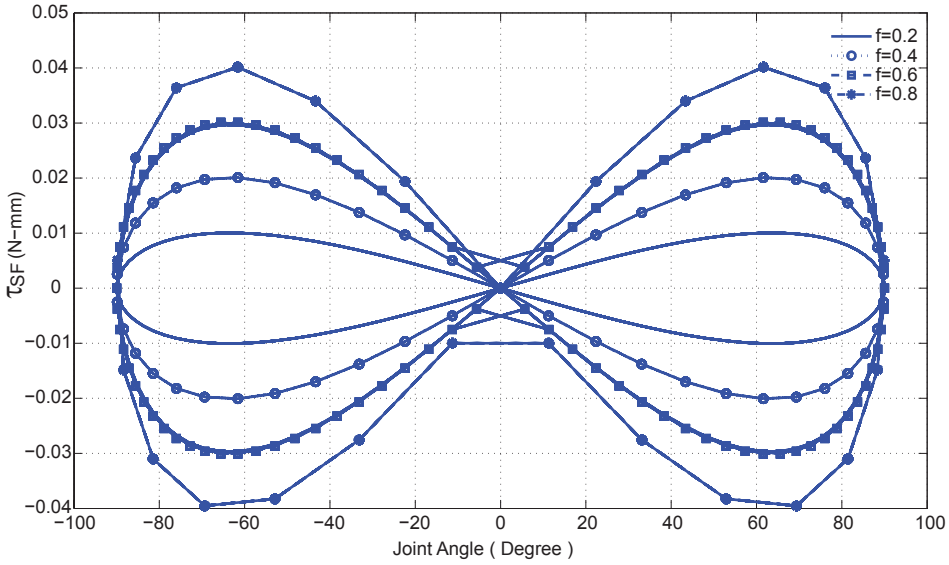

(a) Structural-fluid Damping v.s. θ

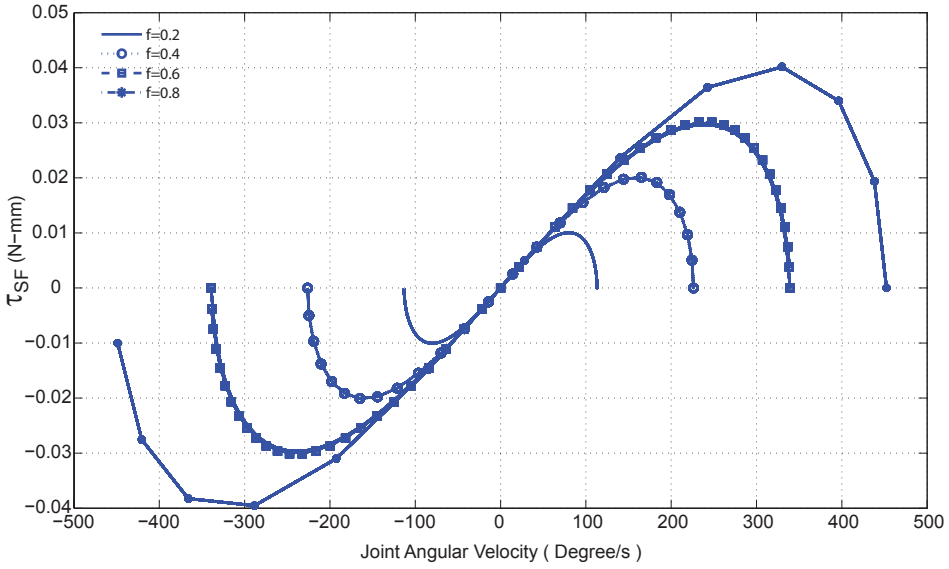

(b) Structural-fluid Damping v.s. ω

Figure 3.14: Demonstrated structural-fluid damping torque with respect to the angle and angular velocity. The fourth feature is oberved from the seven models ($\{1, 4, 8, 14, 15\}_{pc2}$, $\{16\}_{pc1}$, and $\{17\}_{pc3}$).

Based on the classification, the generalized damping torque of the MCP joint interpreted from the 19 models can be summarized following with the importance of the damping features:

$$\tau_d(\theta, \omega, f) \quad = \quad b_{\mathbf{V}}\omega + b_{\mathbf{F}}\omega + b_{\mathbf{S}}sign(\omega) + b_{\mathbf{SF}}sign(\omega) \tag{3.7}$$

where, the τ_d represented a general concept of passive damping at the MCP joint, which included the viscous, fluid, structural, and structural-fluid effects. Even though some models did show that the synovial fluid or joint geometry dominated the energy dissipation behavior rather than the influence from the tissue viscosity, we proposed that the generality of the Eq. 3.7 should meet the robust interpretation of different damping type and its importance based on the significant features relying on the rank of the PCs.

3.3.3 Model Comparison

We also showed the the averaged simplified viscosity (b_v) from the 19 subject-specific models as a comparison with the experimental result and the existing models. We found that the power or linear model could not fit the experimental data ($\overline{B}_f$) which showed a nonlinear trend with respect to the frequency (Fig. 3.15). Estimation from previous damping models with linear and power function were significantly higher than the experimental results. We found that our simplified model and experimental result were similar, classified as nonlinear bell-shaped trends with respect to the frequency (Fig. 3.15). It is important to note that the models from previous research were derived from the experiments with maximal frequency less than $0.2Hz$.

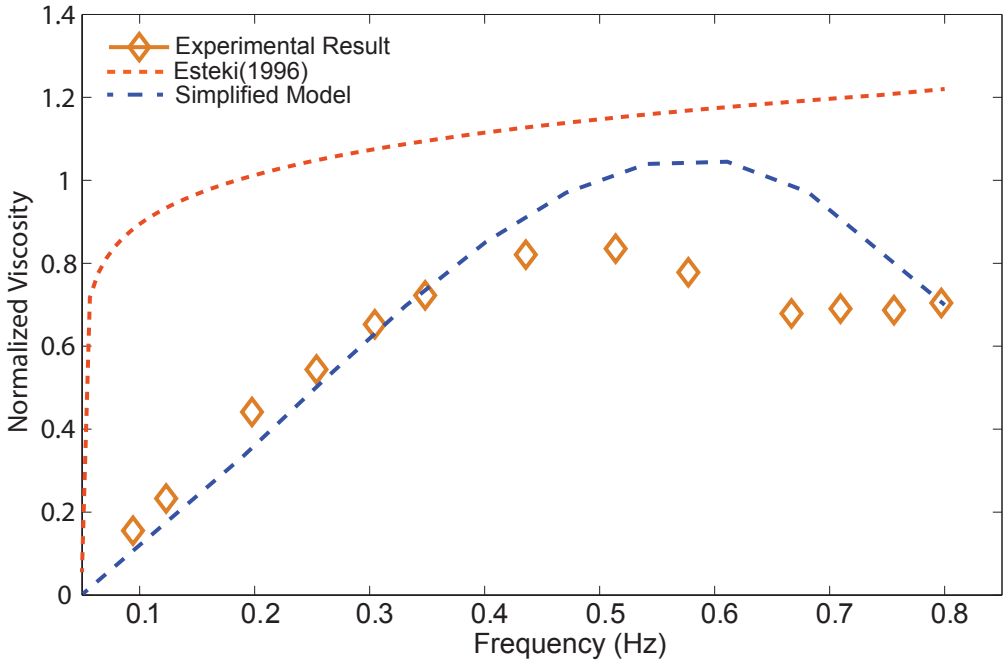

Figure 3.15: Comparisons between the average of experimental results for the energy dissipation capacity, the other damping models from (Esteki and Mansour, 1996), and the average of simplified viscous model (b_v).

3.3.4 Passive Damping Dynamics during the Finger Motion

We investigated the nonlinear damping torques at the angle and angular velocity domain with increased frequencies (Fig. 3.16). During the passive harmonic motion, we found that the damping torques were fairly small at lower frequencies (F = 0.1 $\sim$ 0.2 Hz), and at smaller angular velocities (Fig. 3.16 (a)), and within the whole joint angle range (Fig. 3.16 (d)). The damping torques gradually increased when the frequency and instant angular velocity were increased. The angle and velocity slices in Fig. 3.16 (d) show that higher damping torques were located slightly away from the neutral position (0°), which were distributed in the first and third quadrant of the angle-velocity domain of the index finger (Fig. 3.16 (b)). The torque peaks occurred when the index

finger was stretched with highly extensional velocity (Fig. 3.16 (c)).

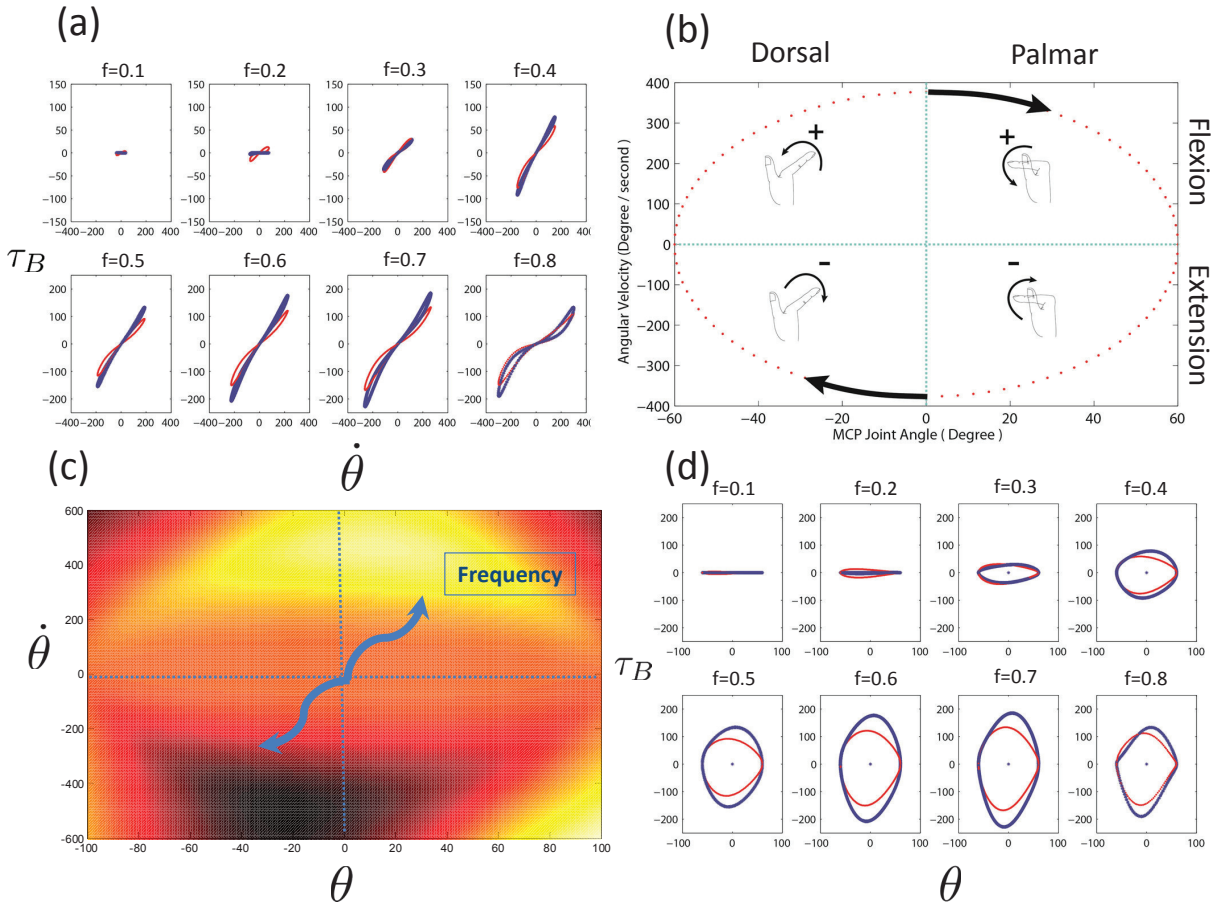

Figure 3.16: (a) and (d) presents the damping moment slices of the model two and nine at the harmonic motion with the increased frequencies (c). The blue arrow shows a direction of changing damping moments when the freqnecy is increased from low to higher values. (b) demonstrates a angle-velocity domain with anatomical defintion to determine the concentrated damping location.

3.4 Discussion

The purpose of this study was to investigate the nonlinearity of energy dissipative behavior of the MCP joint at the index finger, and to further obtain models of inherent passive damping effects to as high a degree of approximation as possible. To identify the nonlinear damping model by mapping the energy dissipative function to the angle, angular velocity, and frequency, we have conducted a series of cyclic tests to estimate passive viscoelastic moments of the MCP joint from 19 subjects. We used the hysteresis loop to derive the energy dissipation functions with the symbolic regression. We then determined different damping effects with the PCA and the loading criterion.

3.4.1 Nonlinear Viscous Damping

Our results showed that the viscous damping was frequency dependent. The viscous damping term, if constant, predicts that energy dissipation is proportional with the cyclic frequency. Although the viscous torque is proportional to the angular velocity observed from our results, the energy dissipation due to the viscosity of the MCP joint is still nonlinearly dependent upon the cyclic frequency for the most cases. We suggest that the viscous damping of the MCP joint cannot be treated as a simple constant or a linear function of the frequency. Moreover, the second-order linear system model is often used to describe viscoelastic behavior of compliant joints in biomechanics, motor control, and robotics. The coefficient of the velocity term stands for the viscosity of passive muscles. We show that the so-called *viscous coefficient* actually includes a functional set of the different damping properties rather than a single constant value. Although we show that the tissue viscosity is still critical in damping, treating the coefficient as the passive *muscle viscosity* may lead to incorrect physical meaning of damping that ignore the existence of other damping properties than just the viscosity. A potential explanation for the nonlinear trend of viscous damping is that

a combined effect of the thixotropic behavior and change of mechanical properties in the various soft tissues crossing the MCP joint, leading to the variations of viscous damping. However, the real mechanism is still not clear with the lumped system model.

We developed a new model that brought out non-Newtonian behavior in viscosity at the MCP joint. The trend of bell-shape in viscosity with respect to the frequency indicates that the apparent viscosity is not proportional to the frequency. In fact, the damping is small at small oscillations or low cyclic frequencies. At the mediate frequency bandwidth ($0.1 \sim 0.6$ Hz), the experimental damping results estimated from the hysteresis loops increased linearly. Therefore, it is reasonable to simplify the viscous damping as a linear function when the frequency of joint movement is low or the oscillating amplitudes is small.

3.4.2 Alternative Damping Types

The identification of biomechanical damping is difficult through the direct measurement in-vivo, and even in the simple mechanical system since the measured values represent the overall damping force/torque. In this study, we used the model-based classification to extrapolate the damping characteristics from the hysteresis loop. We showed that although the 19 fitting models were unique, some general forms of constructed damping were still commonly shown among 19 distinct models. In our study, instead of using the traditional regressions to estimate the coefficients based on known models, we used the symbolic regression for model exploration and the PCA for model reduction. Not only did it allow us to explore the subject specific models but also provided a systematic way to interpret the common damping features of the MCP joint. The viscous and fluid damping play major contributions to the total damping of the MCP joint. Although the effects of the structural and structural-fluid damping due to the friction are small, these should be

considered in the joint modeling when the tissue deformation or relative motion are significant. The interaction between joint contact surface and circulated fluids from the MCP joint, the frictional behavior of structural or structural-fluid damping could contribute to the energy dissipation even more observed from our modeling results, which might be due to the stribeck effect (Gleghorn and Bonassar, 2008).

Joint damping at the MCP is not symmetrical. Our results showed that the passive damping property of the MCP joint not only depended on the cyclic frequency but also depended on the finger positions and the direction of angular velocity. In daily life, the joint kinematics of the human hands often exhibit the harmonic movements to perform tasks in grasping and manipulation. Our results showed that the MCP joint generated higher damping torques passively in finger dorsal position with higher extension angular velocity and in palmar position with flexion angular velocity. Types of input such as cyclic displacements may bring out the position dependency of nonlinear damping.

3.4.3 Applications

The damping models we have developed in this study have applications in human motor control, clinical diagnosis, and robot design and control. The stretch reflex and co-contraction of muscles modulates the body joint stiffness and damping to fine tune the stability in either posture control or trajectory following (Hajian and Howe, 1997; Milner and Cloutier, 1998a; Heitmann et al., 2010; Halaki et al., 2006; Wu et al., 1990). The damping property from soft tissues acts as a mechanical buffer to regulate the limb motion in such as a manner that when the limb motion is moving at high velocity ranges ($> 0.5Hz, 180°/s$), the muscle-reflex system needs to response rapidly to compensate the effect of high passive damping. The passive damping majorly depending on the frequency also absorbs the energy from the impact, external loads, or the motion constraints. For

studies of hand movements and motor control, our finding provides a nonlinear damping model due to the soft tissues and joint structure as a basic internal resistance to study the external disturbance or impact.

Viscosity in spastic patients were larger than the normal subjects (Lee et al., 2004). We provide a model as a base of healthy subjects for the pathological diagnosis and the hand occupational therapy. The model gives useful information for the hand physical therapies to be mindful of applied frequency, amplitude, and speed when the patient's fingers are passively stretched.

For design of new generation of robotic hands, taking advantage of mimicking damping property of the finger joints may improve the performance in grasping and manipulation. For the design a rotational damper or implement the impedance control for robotic hands, we provide a set of damping models which exhibits simplified viscous, fluid, and structural damping. The viscous model with frequency dependency at the trusted bandwidth between $0 \sim 0.8$ Hz can be used for the damping gain estimation in active software control. The development of a human-like damping model may be beneficial to robotic compliance control.

3.4.4 Limitations

In our study, we carefully monitored the muscle activations during the experiments, and eliminated the data when the EMG signals were over the thresholds. One rat study found that the stretch reflex EMG occurred at the ankle joint for high stretch frequency ($f = 2$ Hz) (Hsieh et al., 2010). The other studies showed that the threshold of the stretch reflex was $272^\circ/s$ ($\approx f = 0.76$ Hz (Thompson et al., 1996; Bose et al., 2002). However, we did not find obvious active muscle activities at higher frequencies. Our results showed that the viscous damping moments only passed through the first and third quadrant of moment-velocity domain, which indicated that the system

was defined as a passive system. We assumed that the measured torques had limited changes during the 40 seconds test, and we gave a ample time for subjects to recover from the stress relaxation effect. We did find the higher peaks at the first cycle compared with the rest of cyclic torque peaks. We discarded the data of first cycle during the data processing. Another potential limitation is that the models may not be used to describe precise damping below or over certain frequency range (i.e. $f < 0.1$ Hz or $f > 0.8$ Hz). However, we think that our experimental design really preforms a good coverage of joint kinematics.

3.5 Conclusion

We conclude that the passive damping of the MCP joint at the index finger is non-Newtonian, and it is nonlinearly dependent on the frequency, joint angle, and angular velocity. The usage of constant coefficient to represent the energy dissipation and resistive torque for the articular joint need to be corrected. Using the symbolic regression allows us to achieve high approximation of nonlinear damping models with the experimental data for subject-specific needs. Adopting the PCA with the loading criteria, and the importance of the truncated PCs on the energy dissipation reduce the model complexity for a better interpretation of damping types. The study provides insightful information about intrinsic property of articular joint in human hands for the human motor control, biomechanical joint modeling, clinical diagnosis, and robotic hand design.

Chapter 4

A Novel Joint Design with Human-like Parallel Compliance for Robotic Hands

4.1 Introduction

Toward the goal of designing a new generation of robotic hands with human-like compliance, here we focus on designing a compliant joint mechanism with variable-stiffness. In the human hand, the passive joint compliance varies exponentially with the joint angle and such variable stiffness has been shown to play an important role during grasping and manipulation (Keir et al., 1996). In case of the index finger metacarpophalangeal (MCP) joint, the passive moment vs joint angle curve demonstrates the exponential relationship which results in exponential changes in the joint stiffness. The joint compliance is a combination of the muscles ($< 50\%$) and joint soft tissues plasticity ($> 50\%$) (Kuo and Deshpande, 2012). To be able to achieve human-like manipulation in a robotic form and also to understand the biomechanics of the human hand, we have decided to implement human-like variable stiffness in robotic joints.

Variable stiffness in a robotic joint can be achieved by tuning the stiffness through software control of the actuators based on realtime feedback from position and force sensors (Haddadin et al., 2007), or by designing mechanical elements that passively vary stiffness (Wolf and Hirzinger, 2008; Pratt and Williamson, 1995; Albu-Schaffer et al., 2008; Ham et al., 2009; González Rodríguez et al., 2011). Although the software control strategies, such as impedance control can, in theory, achieve

any desired stiffness without any mechanical change to the system, this approach has limitations. High data bandwidth is critical and any delays in the control and sensing loops can lead to instability, especially, under un-modeled external impacts. Actuators need to expend energy to change and maintain compliance even when the robot is stationary, and there is no mechanism for storing or releasing energy (Eiberger et al., 2010).

On the other hand, the variable stiffness solution achieved through a clever design of mechanical elements leads to configuration based modulation in stiffness (Wolf and Hirzinger, 2008; Albu-Schaffer et al., 2008) and may even be designed to be energetically efficient with its capacity for storing and releasing energy (Grebenstein and van der Smagt, 2008; Jafari et al., 2012). Given these factors, we decided to design a joint module whose compliance changes passively based on its configuration. A number of passive non-linear stiffness designs for robotic joints have been presented previously (Accoto et al., 2012; Carpino et al., 2011; English and Russell, 1999; Grebenstein and van der Smagt, 2008; Laffranchi et al., 2011; Migliore et al., 2005; Eiberger et al., 2010; Wolf and Hirzinger, 2008). Two common branches in this method are antagonistic and series actuator designs (Ham et al., 2009; Jafari et al., 2012). The antagonistic design motivated by the human muscle co-contraction is used to implement non-linear springs into tendon-driven systems to control variable joint stiffness (English and Russell, 1999; Grebenstein and van der Smagt, 2008; Migliore et al., 2005). Series actuator designs are based on the mechanical design of variable stiffness incorporated with joint actuators (Wolf and Hirzinger, 2008; Eiberger et al., 2010; Laffranchi et al., 2011). Some rotary designs with cam shape profiles have successfully incorporated passive compliant elements with variable torsional elasticity without additional actuators to regulate the joint stiffness (Accoto et al., 2012; Carpino et al., 2011; Kuo and Deshpande, 2013). A non-circular pulley-spring mechanism has been designed to create a nonlinear rotational stiffness for the gravity

compensation (Kim and Deshpande, 2014). Although using linear spring to integrate with cam of changing radius gives nonlinear stiffness, these designs depend on commercially available springs. Custom-made springs can be designed, but still the size and weight are too high for an implementation such as robotic hands. The trade-off between need for stiffer spring and decreasing the joint size is critical. Therefore, adopting an alternative energy storing element is necessary.

Recently, elastomer or polyurethane has been used as an alternative to commercial linear metal spring for the robotic applications (Odhner et al., 2014; Schepelmann et al., 2014; Pfeifer et al., 2012; Lantada and Morgado, 2012; Cutkosky and Kim, 2009), including with cam design for nonlinear stiffness (Schepelmann et al., 2014). For the robotic hands, SDM hand used viscoelastic polyurethane as a joint flexure to reduce the joint oscillation and improve the grasping ability (Odhner et al., 2014; Odhner and Dollar, 2011; Dollar and Howe, 2007). A robotic joint capsules with silicon rubber sleeves has been designed to provide passive joint compliance (Xu et al., 2012). The authors claimed that the artificial joints possessed stiffness and damping properties similar to the human fingers, however they simplified nonlinear stiffness and damping of finger joints as constant values (Xu et al., 2011). In this work, we have developed a miniaturized compliant joint in which the passive joint properties match those derived from the human experiments (Kuo and Deshpande, 2012).

The nonlinear passive stiffness of the human hand, which varies over a wide range of motion, has been shown to play an important role in movement and dexterity. The maximal range of motion of the index finger MCP joint in natural movements is about 90° - 103° (Ingram et al., 2008) and an average of 165° under passive stretching (Kuo and Deshpande, 2012). We used MCP joint torque-angle results from human experiments to design an intrinsically flexible joint that possesses human-like finger joint compliance. Our idea is to then use the active compliance control only for

the stiffness component in grasping and manipulation that cannot be realized by the preset flexible joint.

A previous version of variable stiffness joint mechanism (shown in Fig. 4.1) is based on the idea of cam shape integrating with linear spring follower, and it generates the double exponential joint torque profile with a modular design (Kuo and Deshpande, 2013). However, considering the size and weight of this joint design, we decide to use new idea for generating nonlinear stiffness involving compliant materials and rotary pulleys. We have realized a miniaturized design for compliant joint with 3-D printing technique and custom-made elastomer (shown in Fig. 4.2). The key innovations in this design are: a) nonlinear elasticity of compliant materials to increase the capacity of storing energy effectively, b) variable pulley configurations to tune the stiffness profile, and c) pretension mechanism to scale the stiffness profile.

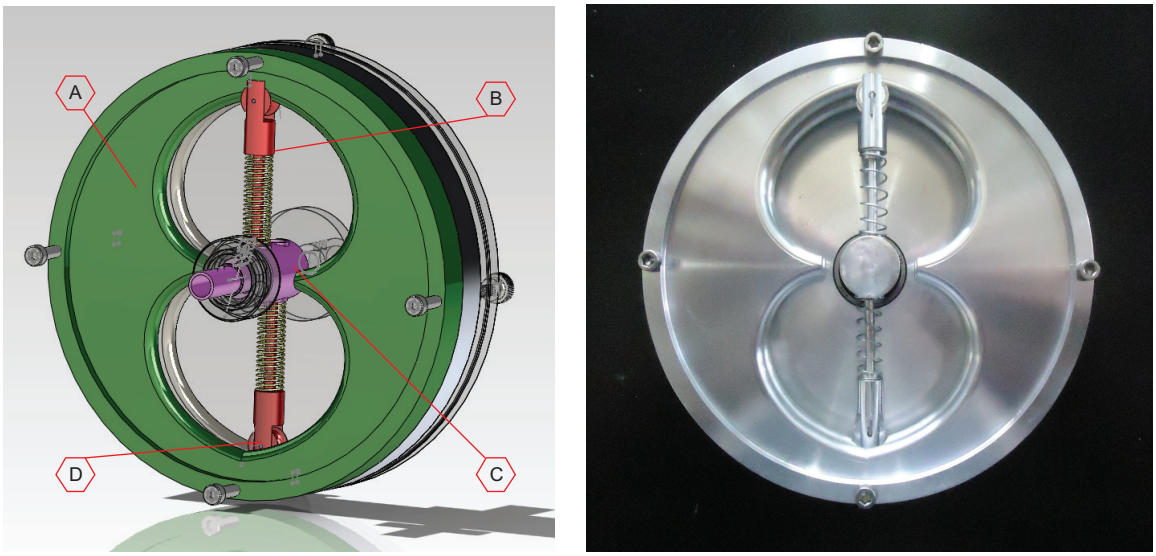

(a) CAD model of the design (b) Front view of the prototype

Figure 4.1: A variable stiffness joint mechanism with the components - (A): cam profile, (B): spring follower, (C): main shaft, and (D): arced roller. The dimension of the joint mechanism is 120 × 40 milimeter (Diameter × Thickness) and weight is 765 gram.

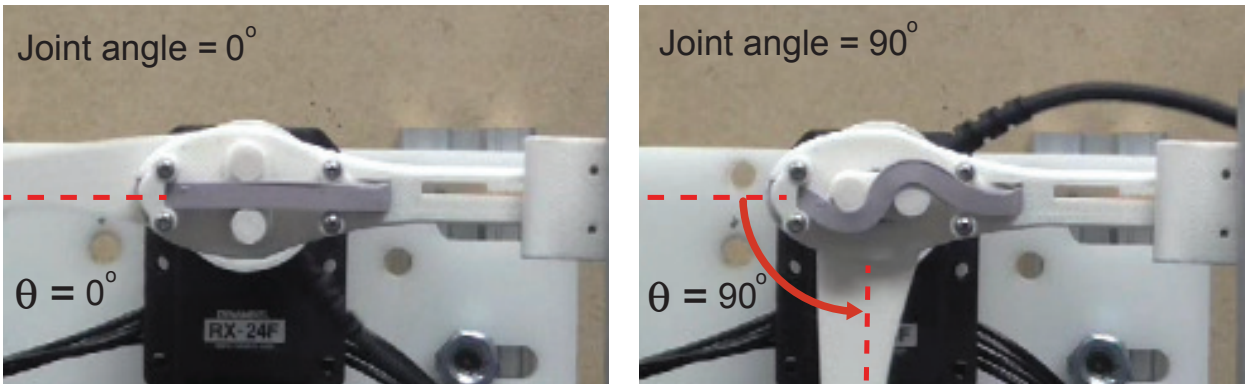

(a) Joint resting position (b) 90° joint rotation

Figure 4.2: A prototype of novel design and the test bed for the parallel compliant joint mechanism. The features such as compliant material, variable pulley configuration, and pre-tension mechanism are shown in subfigures. The dimension of the joint mechanism is 25.46 × 23.18 milimeter (Diameter × Thickness) and weight is 5.34 gram.

4.2 Variable Stiffness Joint Design

4.2.1 Joint configuration

The underlying joint mechanism is based on a configuration shown in Fig. 4.3. A rectangular shape of compliant material, with a dimensions, $2L_o \times t \times W$ (Length $\times$ Thickness $\times$ Width), is located between a pair of pulleys that connect with the rotating shaft of the joint (Fig. 4.3(a)). The pulleys rotate the same angle about the center of joint when the joint is rotated. The radii of the pulleys are r_p, and the distances between the pulleys and the joint center are R. Two pairs of spacers with radius r_s constrain the material at the ends as the pulleys engage with the compliant material during the joint rotation. The material is fixed at the end of the joint by a clamp that guaranteed the security of the material. The material generates passive tension when it is stretched, and this results in passive torque around the joint (Fig. 4.3(b)).

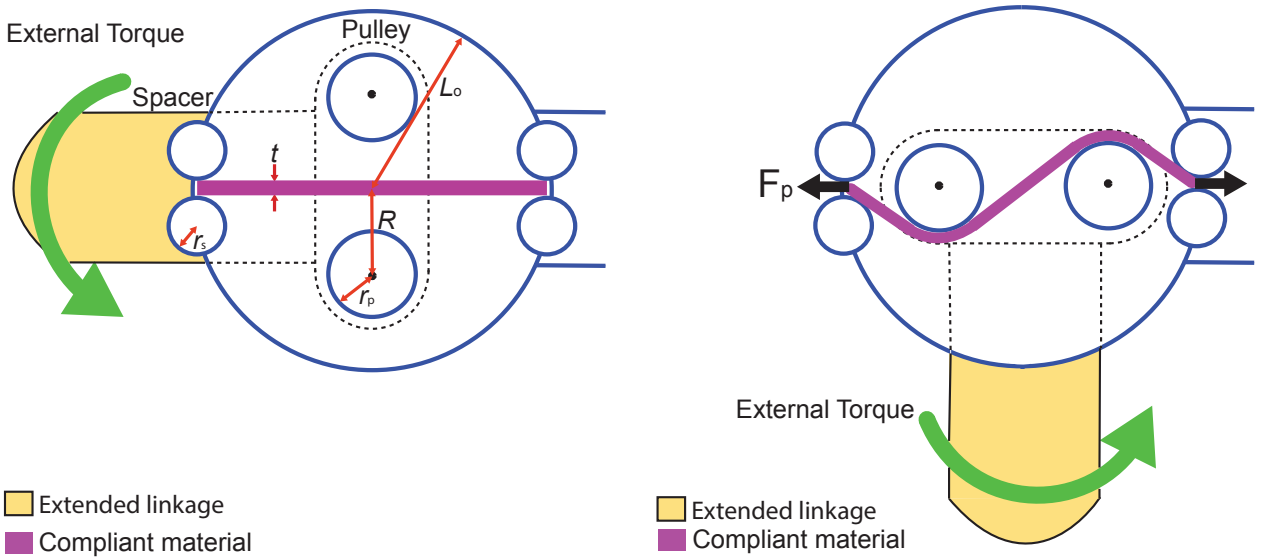

(a) Initial joint configuration

(b) Rotated joint configuration

Figure 4.3: The underlying configuration for variable stiffness joint. The dimension of the joint design with the compliant materials at the initial position $\theta_d = 0°$ (a), and at the joint angle $\theta_d = 90°$ (b). The green arrows show that the pulleys rotated about the center of the joint.

4.2.2 Material excursion (L)

Based on the configuration, a mathematical model of joint compliance is developed using the joint geometry (Fig. 4.4). We derive the stretch length of the material (L) due to the change of joint angle by summing the curvatures ($S1$ and $S2$) and the lengths ($D1$ and $D2$) between two insertion points on the pulleys and spacers. The stretch length is a function of joint angle (θ_d) and the design variables (L_o, R, r_p, r_s, t) (Fig 4.3). The two distances D_1 and D_2 can be expressed as:

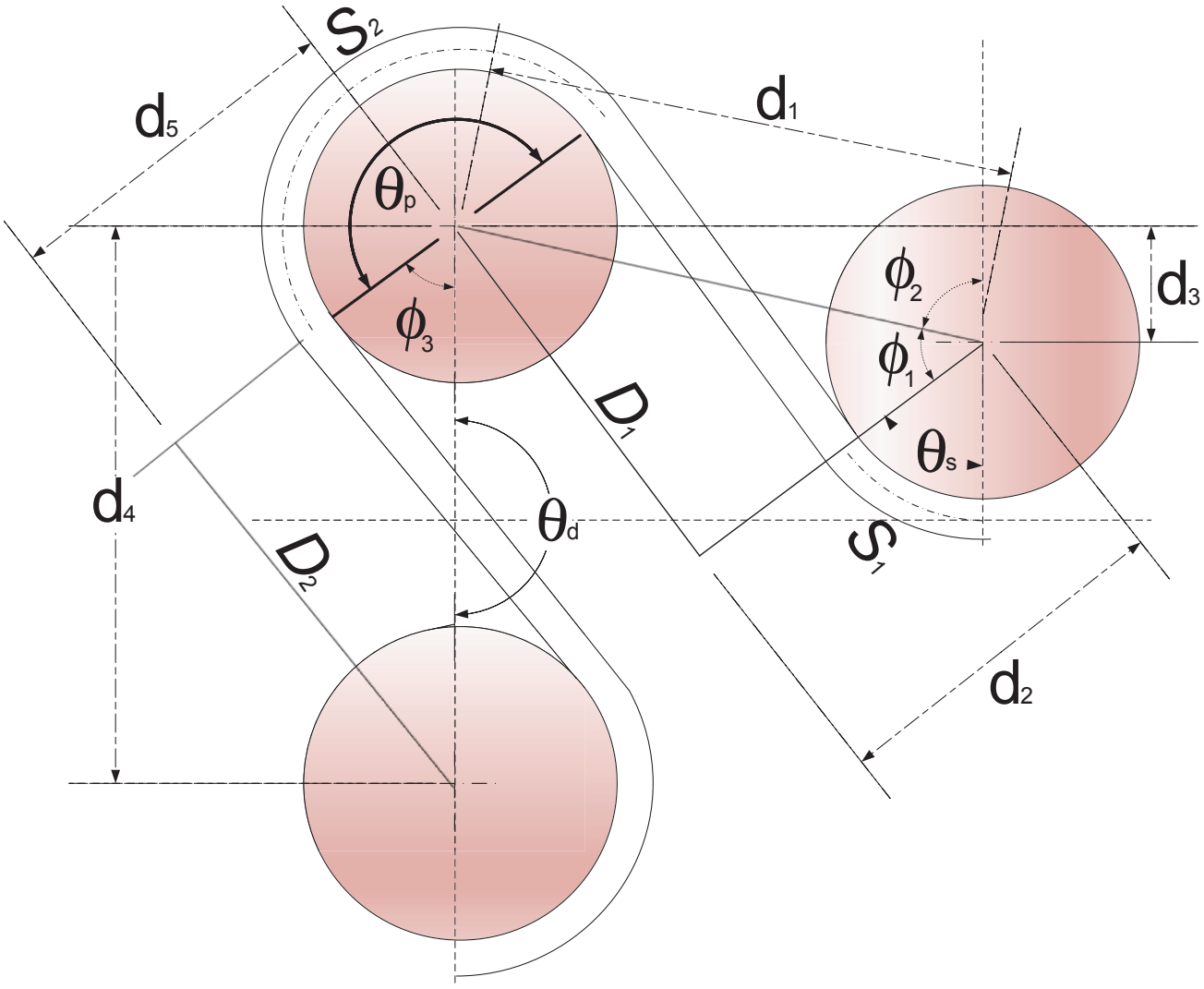

Figure 4.4: A schematic diagram of the rotated joint configuration and geometrical representations.

$$
\begin{aligned}
D_1 &= \sqrt{d_1^2 - d_2^2} && (4.1)\\
&= \sqrt{(L_o - R\sin\theta_d)^2 + (r_s + 0.5t + R\cos\theta_d)^2 - (r_p + r_s + t)^2} && (4.2)\\
D_2 &= \sqrt{d_4^2 - d_5^2} && (4.3)\\
&= \sqrt{4R^2 - (2r_p + t)^2} && (4.4)
\end{aligned}
$$

where, the d_2, d_4,and d_5 were constant distances summed from the pulley radius and material thickness, and the vector d_1 described the relative motion between the pulleys and spacers.

$$
\begin{aligned}
\vec{d_1} &= (L_o - R\sin\theta_d)\vec{i} + (r_s + 0.5t + R\cos\theta_d)\vec{j} && (4.5)\\
& && (4.6)
\end{aligned}
$$

Since the curvatures S_1 and S_2 are both functions of routing angles, and radius of the pulleys and spacers. They can be expressed as:

$$
\begin{aligned}
S_1 &= \theta_s r_s && (4.7)\\
S_2 &= \theta_p r_p && (4.8)
\end{aligned}
$$

where, the spacer angle θ_s and the pulley angle θ_p can be derived from:

$$
\begin{aligned}
\theta_s &= \pi - \phi_1 - \phi_2 && (4.9)\\
\theta_p &= \theta_d + \theta_s - \phi_3 && (4.10)
\end{aligned}
$$

where,

$$\phi_1 = \sin^{-1}(\frac{D_1}{d_1}) \tag{4.11}$$

$$\phi_2 = \sin^{-1}(\frac{d_3}{d_1}) \tag{4.12}$$

$$\phi_3 = \sin^{-1}(\frac{D_2}{d_4}) \tag{4.13}$$

Therefore, the stretch length of the material can be expressed as:

$$L = 2(S_1 + S_2 + D_1) + D_2 > 2L_o \tag{4.14}$$

4.2.3 Material resistive force (F_p)

After we determine the stretch length of the material due to the joint rotation, the material tension can be estimated by the material property derived from the tensile test. We assume that the total volume of the material does not change when unloaded or loaded ($AL = A_oL_o$). The tension generated by compliant material can be expressed as:

$$F_p = f_t(\epsilon_t)A = f_t(\epsilon_t)\frac{A_oL_o}{L} = \frac{V_o}{L}f_t(L) \tag{4.15}$$

where, V_o and L_o is the unchanged volume and the initial length of the material. The stress ($\sigma_t = f_t(\epsilon_t)$) is a function of true strain (ϵ_t), and it can be converted to the function of material excursion (L).

4.2.4 Effective moment arm (MA) and resultant joint torque (τ_{design})

The effective moment arm of material tension due to the joint rotation is the rate of change of material length with respect to the joint angle. By taking a partial differentiation of total excursions (E) with respect to the joint angle (θ_d), the instantaneous moment arm (MA) can be derived:

$$E = \delta L = L - 2L_o \tag{4.16}$$

$$MA(\theta_d) = \frac{\partial E}{\partial \theta_d} \tag{4.17}$$

Once the effective moment arm is determined, the passive joint torque of the design can be calculated by the effective moment arm and material tension:

$$\tau_{design}(\theta_d) = MA(\theta_d) F_p(L) \tag{4.18}$$

4.2.5 Elastic materials: silicone and polyurethane

We choose a silicone elastomer (PlatSil $71-20$ series, Polytek Corp., PA, USA) and a polyurethane rubber (PMC 724, Smooth-On Inc., PA, USA) as bases to create compliant materials of varying elastic properties. Both contain two mixed components, and need addition-curing. The basic information is shown in Table 4.1. By adjusting the mixing ratio, we aim to create different levels of nonlinear elasticity for the joint design. The tensile tests for the new materials are carried out for validating the material properties.

Table 4.1: Physical properties of two commercial compliant materials. The resources are from the data sheets provided by the Polytek Corp and Smooth-On.

Type	Mixing Ratio	Tensile Strength (mPa)	Elongation Break	Cure Time (hrs)
Polyurethane (P)	1 : 10 by Weight	4.14	$> 700\%$	16 ($> 73°F$)
Silicone (S)	1 : 1 by Volume	2.54	$> 530\%$	24 ($> 77°F$)

4.2.5.1 Mixing, Vacuuming, and Curing Procedure

We decide the adjusted ratio of the mixed compounds based on the empirical trials and the manufacturer's suggestions. The mixed materials are compose of two liquid compounds, material A and B, separately. We create six materials by mixing these two compounds based on the ratios shown in Table 4.2.

Table 4.2: Mixing ratios and notations for the six elastic materials. Material P series are mixed by weight ($gram$) and Material S series are mixed by volume (ml). $P1$ and $S1$ have the default ratios recommended from the manufacturing.

Type	P_1	P_2	P_3	S_1	S_2	S_3
Polyurethane (P)	1 : 10	1 : 5	1 : 1			
Silicone (S)				1 : 1	1 : 2	2 : 1

Initially, material A and B compound are separated in different containers before we started the mixing protocol. Each mixing takes over ten minutes to ensure the two compounds are well mixed. Following the ASTM $D412$ standard which instructs the tension test for general compliant elastomers, we prepared "dumbbell" shaped samples for tensile tests. We use a Computer Numerical Control (CNC) machine to manufacture the specimen molds. After application of a release agent on the molds, we carefully poured the mixed materials into the molds, and secured the mold panel into a vacuum chamber. We controlled the room temperature at $73°F$ and the chamber pressure at 35 psi to remove air from the specimens. The specimens were settled to cure for at least 24 hours

after the specimens were vacuumed for 20 minutes (Fig. 4.5(a)).

(a) Dumbbell shape for specimen

(b) Tensile machine during test

Figure 4.5: ASTM *D*412 standard test for specimen with curing materials and tensile test with large elongation of testing material.

4.2.5.2 Tensile Test

We used a tensile test machine (Instron, MA, USA) to conduct a series of tensile strength tests for the compliant materials (Fig. 4.5(b)). The geometric parameters of each specimens such as width and thickness of flat head and neck areas were measured, and were used as inputs for the calculation of material properties. We carefully loaded the specimens on the clamps of the

machine, and placed the extensometer to define a initial length of test specimen. The test speed is 20 inches per minute, and the machine continued to pull the specimens until ruptured. We tested four specimens of each materials. The material property for each materials was derived and averaged from the test results of four samples. Because all the specimens show large deformations when loaded, we compared the true stress and strain with the engineering stress ($\sigma_e = \frac{F_p}{A}$) and strain ($\epsilon_e = \frac{\delta L}{L_o}$) to identify the material linearity or nonlinearity, in order to estimate a linear elastic region in which the material can be treated as a liner spring. If the material excursion is under the linear elastic range, we can use a constant Young's modulus ($E = \frac{\sigma_e}{\epsilon_e}$) to estimate the linear force of the material ($F_p = \frac{EA_o\delta L}{L_o}$). The true stress and strain can be expressed as:

$$\sigma_{true} = \sigma_e(1 + \epsilon_e) \tag{4.19}$$

$$\epsilon_{true} = ln(1 + \epsilon_e) \tag{4.20}$$

On the other hand, if the elasticity of the compliant materials is highly nonlinear, as observed from the true stress-strain curve, a nonlinear elastic model is necessary. We used a power function (ax^b) to fit the experimental data, and the goodness of fit was validated. This tensile tests provide nonlinear elastic property of tested materials for the options of choosing energy storing element of the variable stiffness joint design.

4.2.6 Parametric analysis

We carry out a parametric analysis to determine the exact passive torque generated by the configuration as described above, and also to determine the effects of changes in design variables on the key design features. Fig. 4.6(a) shows the configuration base values for the design variables. Fig. 4.6(b) 4.6(d) show the configurations with altered values for the design variables. As shown in Fig. 4.7, the design parameters such as routing angles of the material on the pulley and spacer

(θ_p, θ_s), material length change (δL), effective moment arm $(MA(\theta_d))$, and resultant joint torque (τ_{design}) are investigated by adjusting the pulley radius r_p (case 1), material thickness t (case 2), and the distance R (case 3). By tuning individual design variables, we observe different levels of material excursion and effective moment arm, leading to nonlinear joint torques. This is promising because it shows by changing the design variables, we may be able to achieve the desired human-like passive torque profile. However, we cannot achieve human-like compliance by tuning the design variable individually (Fig. 4.7(d)). To address this we carry out a design optimization to search for the best set of the design variables such that the optimum joint configuration can exhibit a human-like joint torque-angle relationship.

In summary, we have developed a mathematical model of the joint design. Instead of using linear spring, we consider compliant materials which engage with the pulleys during the joint rotation. The large elongation of selected materials may store the potential energy efficiently without collinear stretching. This design also allows us to increase the range of motion without mechanical limits. In order to mimic the human-like joint torque profile, it is important to choose the right materials and to understand the elastic properties of materials selected.

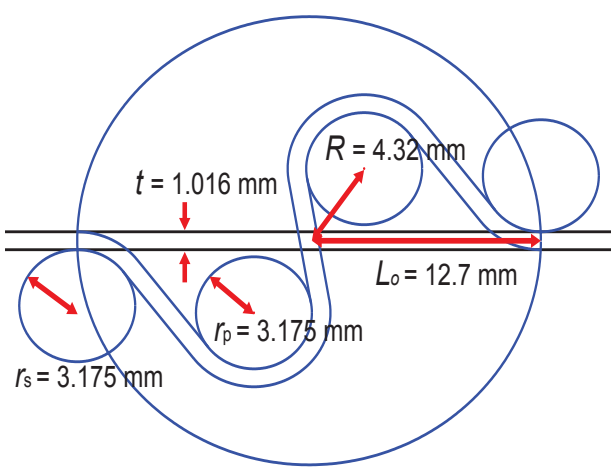

(a) Initial Configuration

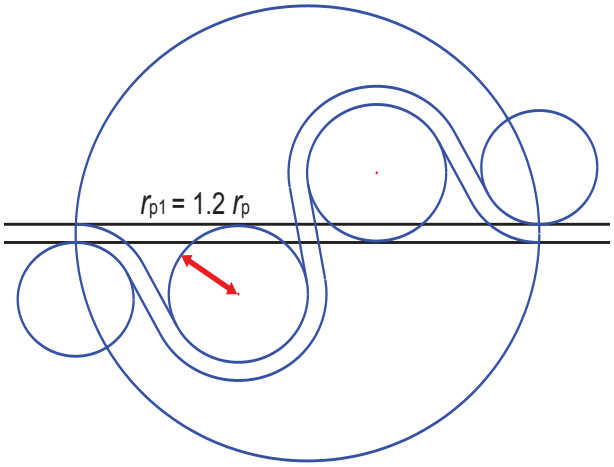

(b) Case 1: Increase pulley radius r_p

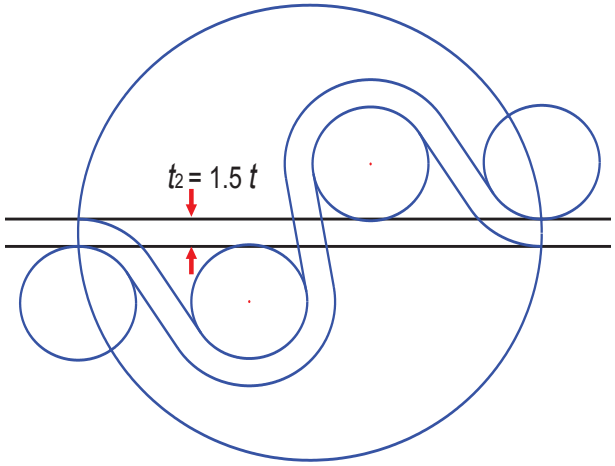

(c) Case 2: Increase material thickness t

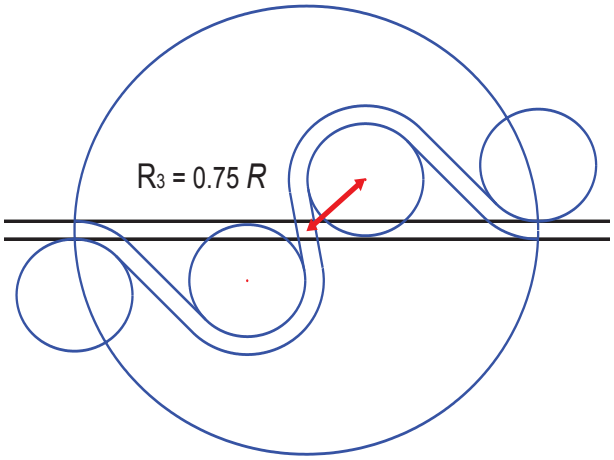

(d) Case 3: Decrease the distance R

Figure 4.6: Three cases of adjusted joint configuration due to change of deisgn variables.

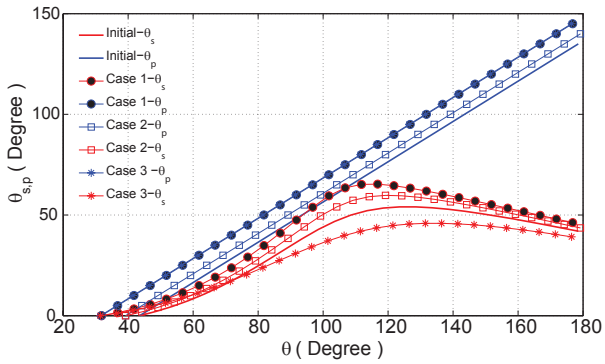

(a) Routing angles, θ_p and θ_s

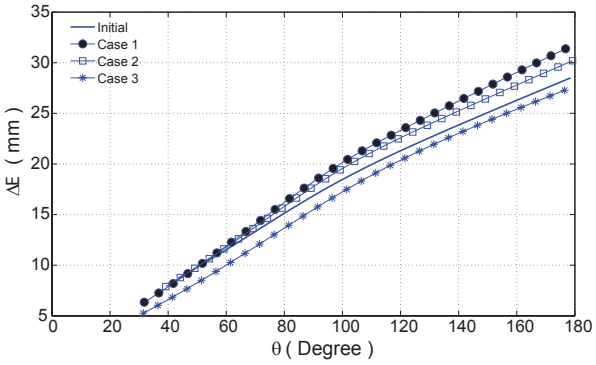

(b) Material excursion, δL

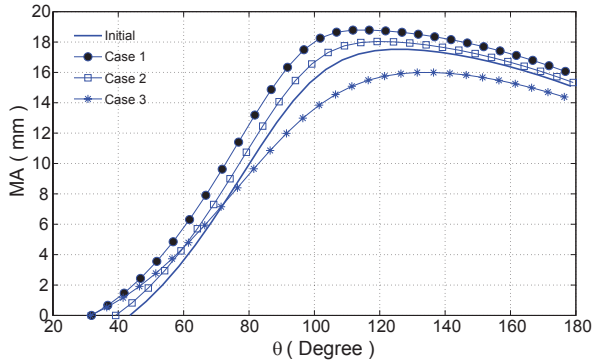

(c) Moment arm, MA

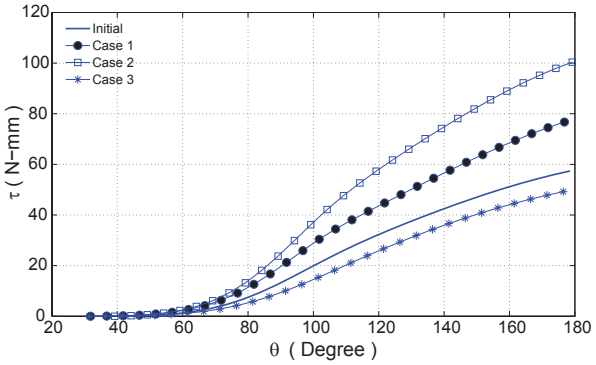

(d) Passive joint torque, τ_{design}

Figure 4.7: The results of design parameters by changing the design variables. Routing angles (4.7(a)), material excrusion (4.7(b)), effective moement arm (4.7(c)), and joint toruqe (4.7(d)) are investigated based on the three cases in Fig. 4.6.

4.2.7 Design Optimization

The goal of the design optimization in this work is to search for an optimum set of geometrical variable values so that the joint exhibits exponential torque for a wide range of joint rotation. The design variables are radius of joint (L_o), pulley (r_p), and spacer (r_s), the distance between center of pulleys and joint (R), and the thickness of compliant material (t). To find an optimum values for

geometrical variables, an optimization with inequality of geometrical constraints is carried out to search for the best set of $\{L_o, R, r_p, r_s, t\}$. Consider the optimization problem as:

$$minimize \quad E = \sqrt{\frac{\sum_{\theta_d=0}^{\theta_d=100} (\tau_{desired}(\theta_d) - \tau_{design}(\theta_d))^2}{n}} \tag{4.21}$$

subject to the constraints:

$$g(1) = 0.5t + r_p - R \leq 0 \tag{4.22}$$

$$g(2) = R - L_o \leq 0 \tag{4.23}$$

$$g(3) = t + r_s + r_p - d_1 \leq 0 \tag{4.24}$$

The objective function in Eq. 4.21 minimizes the root mean square error (RMSE) between the summation of design and desired joint torques calculated at the joint range $\theta_d = 0^\circ \sim 100^\circ$. The joint torque values τ_{design} are computed by adopting Eq. 4.15 to 4.18 at each joint angle, and are summed through the whole range of motion. For the geometric constraints, $g(1)$ in Eq. 4.22 demonstrates that pulleys cannot compress the material at least the distance R is small their summation, $g(2)$ indicates that the internal distance R is smaller than overall joint dimension (L_o), and $g(3)$ is the geometrical constraint that guarantees such that the material can not be over compressed when the pulleys and spacers are collinear at a certain joint angle. We choose the elastic model of original M_2 as a default material with a width of 4 mm in the optimization search.

The gradient projection method is used to search for the optimal set of design variables with initial guess of the design variable set $\{L_o, R, r_p, r_s, t\} = \{13, 5.08, 3.18, 3.18, 0.51\}$ mm. The optimization algorithm is successful and optimum set of design variables ($\{L_o, R, r_p, r_s, t\}_{optimum} =$

$\{25.46, 9.38, 5.36, 4.04, 8.08\}$ mm) lead to a close matching of the desired torque profile (Fig. 4.8). The variable values are larger than initially guessed values (Fig. 4.8(a)). The thickness of the material increases drastically to fill the gap between two pulleys so that the material contributes to the passive force and moment arm at the initial position (Fig. 4.8(b)). We can scale down the overall joint dimension by selecting a stiffer elastic material.

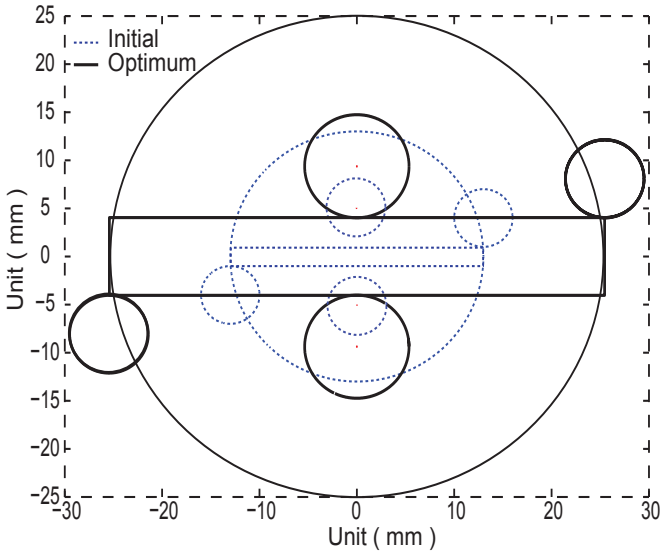

(a) Joint configurations

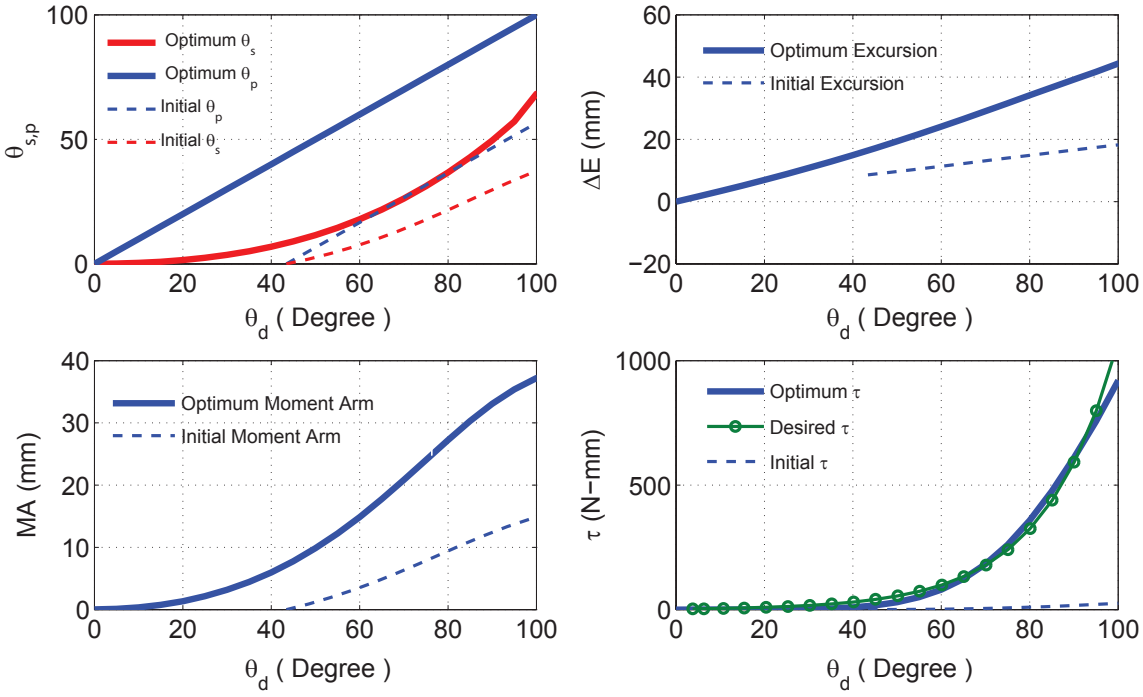

(b) Design parameters

Figure 4.8: Results from optimization of design variables and parameters.

4.2.8 Tuning the Variable Joint Torque Profile

Human finger joint compliance at the MCP joint of the index finger is asymmetric in extension and flexion. Therefore, we introduce two mechanisms to adjust the joint torque profile in different rotating directions. Tuning the joint torque profile includes to either change the torque amplitude or the shape of torque curve. In this section, we introduce two mechanisms that one could change the pretension of the materials, and the other could adjust the effective moment arm of applied tension.

4.2.8.1 Pretension mechanism

Adjusting pretension of compliant material allows us to scale the joint torque amplitude, while keeping the same torque profile. We designed a mechanism to adjust the pretension of compliant material by stretching the material at the neutral position. A chamber is designed in the segment to embed the mechanism. We created a socket-head type of screw as an adjuster to change the pretension of the material (Fig. 4.11(b)). The housing can slide through the chamber when the screw is rotated out of the chamber. A slot in the housing is designed to fit the material and to ensure that the material is fixed nicely. Also, the pulling force from the screw can transmit to the housing collinearily. The pretension level can be determined by the displacement of the housing which is controlled by the increment of thread counts. Two open tunnels at both sides of segments are created such that a piece of customized parallel compliant materials can be routed through the segment (Fig. 4.11(a)), and then the material connects with the pretension mechanism (Fig. 4.11(b)). A cast based on the design is fabricated to create the non-uniform shape of the compliant material for this element (Fig. 4.12). The overall pretension mechanism with the material is embed into the chamber inside the mechanism's main body.

4.2.8.2 Variable pulley configuration

The other way to adjust the torque profile is to change the effective moment arm (Fig. 4.4 and Eq. 4.17). The effective moment arm is mainly decided by the excursion of compliant material due to the joint geometry or the vector originated from the center of the joint perpendicular to the applied tension of engaged material. Changing the pulleys location will adjust the effect moment arm without changing any design variables or carrying out further optimization. Given the pulleys off-center (C), the pulleys can be rotated at clockwise or counter-clockwise direction with respect to the pulley base to increase or decrease the effective moment arm (Fig. 4.9). We define the off-center point C at the mid-point of the original radius r_p. The pulley is arbitrarily rotated θ_r so that a virtual center of the pulley O' reconstructs the mathematical relation between the material excursion and joint geometry. For instance, a new radius R' and distance d_1' in Fig. 4.9 were used to derive the curvature S_1 and the distance D_1 in Fig. 4.4. The coordinate of virtual center O' was written as a vector form below:

$$\vec{O'} = \{(R + \frac{r_p}{2})\sin(\theta_d) - \frac{r_p}{2}\sin(\pi - \theta_d - \theta_r)\}\vec{i} + \{-(R + \frac{r_p}{2})\cos(\theta_d) - \frac{r_p}{2}\cos(\pi - \theta_d - \theta_r)\}\vec{j} \quad (4.25)$$

Following the same calculation as previously, the material excursion and effective moment arm, which differed from the initial configuration, can then be derived. In Fig. 4.9, we demonstrate the geometrical change when the bottom pulley is rotated about the off-center (C) at the counter-clockwise direction with a angle θ_r. The top pulley can be adjusted with the same fashion.

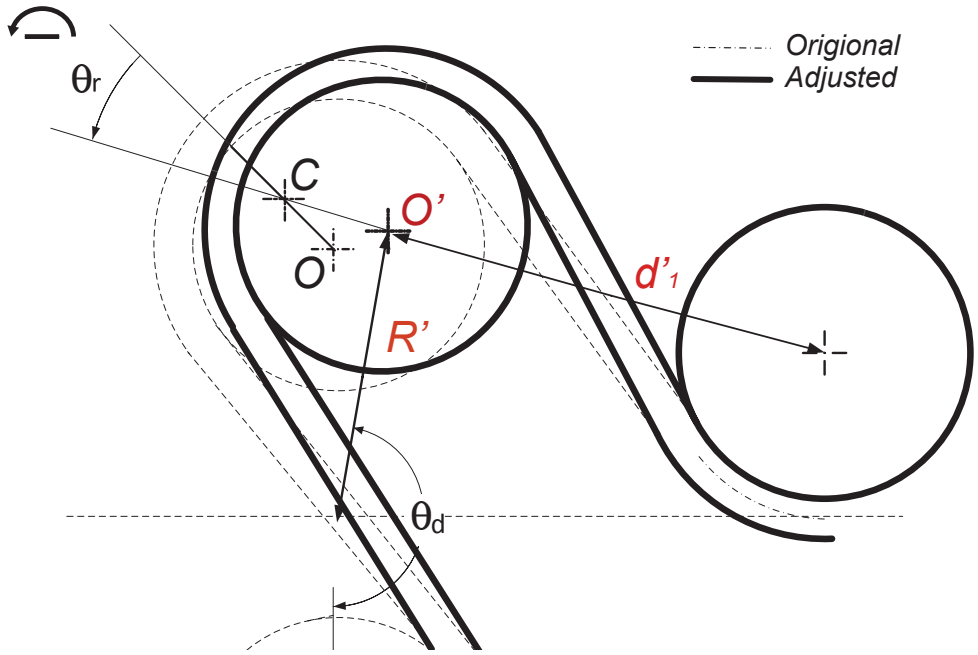

Figure 4.9: A schematic diagram of off-center pulley and its new gometrical parameters due to the rotation in conter-clockwise direction. The pulley is rotated about the off-center C with the angle θ_r, causing a change of geometrical engagment between the pulley and the material such that the new center of pulley (O'), radius (R'), and the distance R' change the effective moment arm.

The other effect of changing the pulley angles is that it shifts the contact phase with the material. In the original setup, there is no delay in engagement of the material with the two pulleys. In the case of adjusted pulley configurations, the contact angle for each pulleys can be derived by calculating the vertical gap between the pulleys and the material:

$$G_b = -(R + 0.5r_p)\cos(\theta_b d) - 0.5r_p \cos(\pi - \theta_b d - \theta_r) + r_p + t \tag{4.26}$$

$$G_t = (R + 0.5r_p)\cos(\theta_t d) + 0.5r_p \cos(\pi - \theta_t d - \theta_t) - r_p - t \tag{4.27}$$

where the gaps G_b and G_t give the distances between the bottom and top pulley and material when

the bottom and top pulley is rotated with the angle θ_r and θ_t. The contact angles for the bottom and top pulley are θ_{bd} and θ_{td}, respectively. If these two angles, for instance, are both rotated 60° at clockwise directions, the contact angles for both pulleys are both 42° when the joint is rotated at the counter-clock direction. On the other hand, if the direction of rotation is switched to counter-clockwise direction for both pulleys with the same angles as previously, the contact angles for both pulleys are 18° when joint rotated counter-clock wisely. The contact angles θ_{bd} and θ_{td} not only shift the timing of contacting material but also affect the material excursion in a sense that the excursion of material D_2 and the material excursion due to the non-engaged pulley are absent in the calculation (Fig. 4.4).

To test the effect of changing the pulley configuration, we designed a hexagonal shape of conjunction on the pulley base which allows the pulleys to rotate in two directions. We increase the rotated angle with an increment of 60° at clockwise (+) or counter-clockwise (−) direction for two pulleys. Fig. 4.10 shows five pulley configurations that we test in order to achieve the desired shift in joint torque profile with respect to the joint angle .

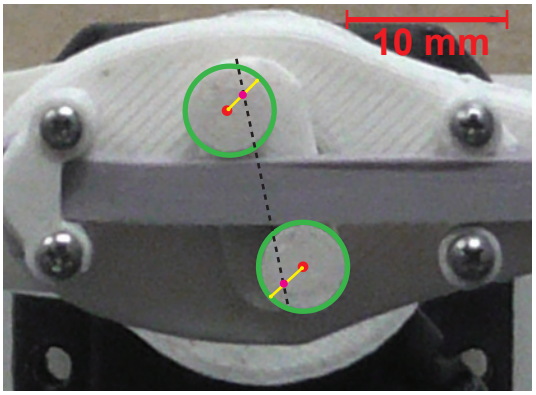

(a) Config. 1: Top and bottom 60°(+)

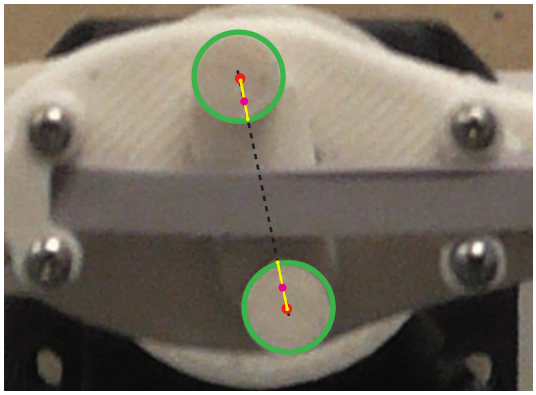

(b) Config. 2: Top and bottom 180°(+)

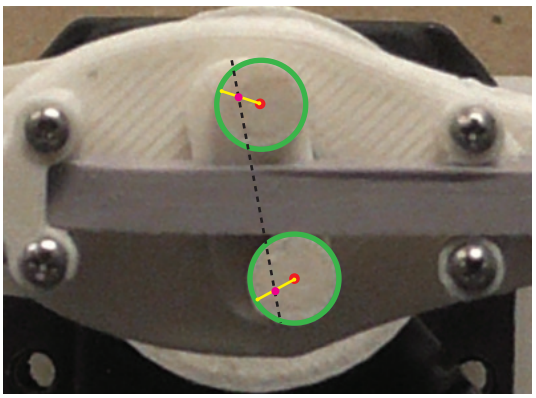

(c) Config. 3: Top 60°(−) and bottom 60°(+)

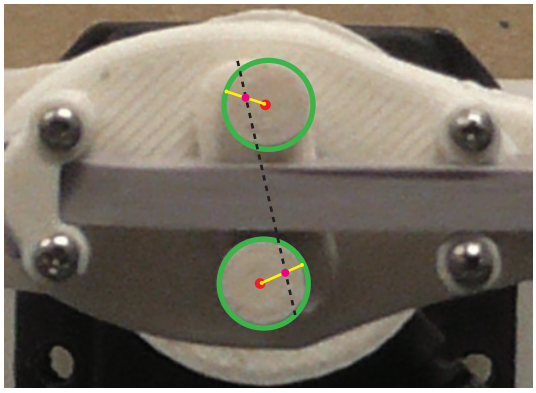

(d) Config. 4: Top 60°(−) and bottom 120°(−)

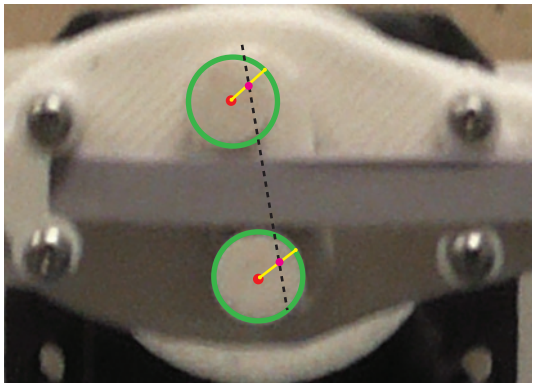

(e) Config. 5: Top 60°(+) and bottom 120°(−)

Figure 4.10: Five pulley configurations to modify the moment arm and hence the passive torque profile in the joint design.

4.3 Prototype Design and Manufacturing

The miniaturized prototype of passive parallel joint design and each component are shown in Fig. 4.11. From the design optimization, the radius of the joint L_o resulted to be about 25 mm with choice of elastic material with low elasticity. It is possible to scale down the overall dimensions of the joint design variables to a different sizes while still maintaining the same torque profile by replacing the material with a one with higher stiffness. In this study, for the purpose of demonstration, we scale the design variables derived from optimization by half to ($\{L_o, R, r_p, r_s, t\} = \{12.73, 4.69, 2.68, 2.02, 4.04\}$). This results in the outer diameter of main body to be 25.46 mm (Fig. 4.11(a)), which is comparable with the size of the human MCP joint.

We use a plastic extruding-type of 3D printing technique to make the prototype (Replicator $X2$, MakerBot, NY, USA). The Polylactic Acid (PLA) is used as a printing material. For the shape deposition of compliant material, we build the design mold for the mixed material, mix and pour the material into the mold, and then place the mold in the vacuum chamber to remove the air from the mixed material. We wait over 24 hours for the material to cure. Fig. 4.12 shows the 3D printed mold and the testing materials. The miniature stainless steel ball bearings (Outer diameter: 5 mm) are used in assembly. Extended segments are built to connect the joint center with the sensing and actuation (Fig. 4.11(a)). The pulley can connect with a junction of extended segment through a geometrical slot and constraint. The pulley can be rotated in 60° increments through the design shown in Fig. 4.11(c). The small clamps with rough surfaces mounted on the main body are used to fix the compliant material at the end (Fig. 4.11(d)). The material S_1 is used to test the pretension mechanism (Fig. 4.11(b)). The material is fixed in the housing with a screw so that the material does not slip through the pulling when the joint is rotated. We embed the pretension mechanism inside of the main body when we carry out the experiment.

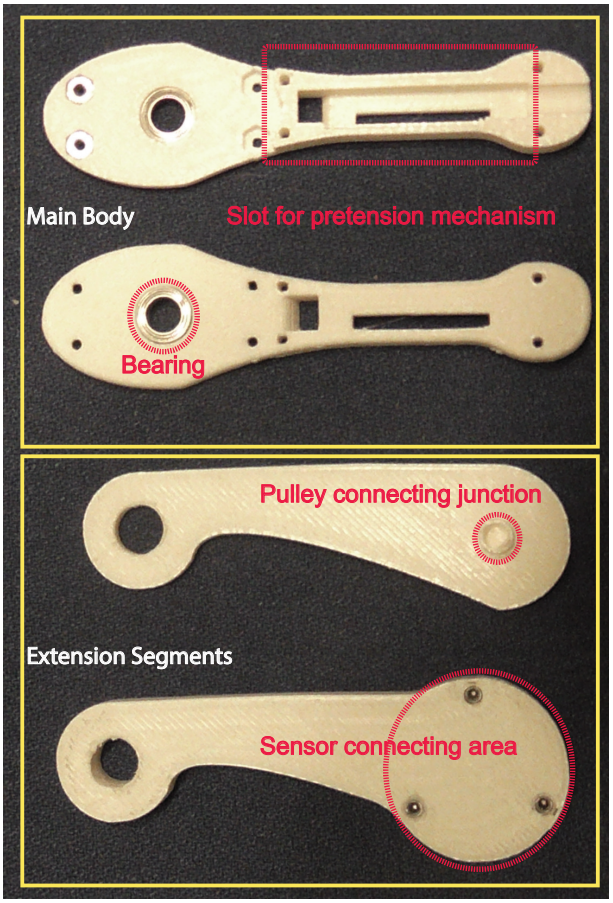

(a) Main structures

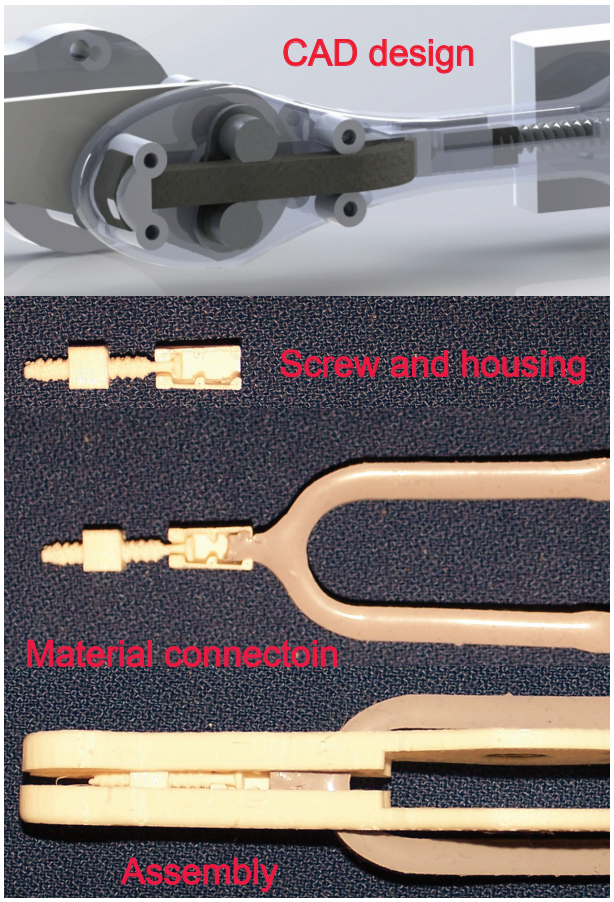

(b) Pretension mechanism

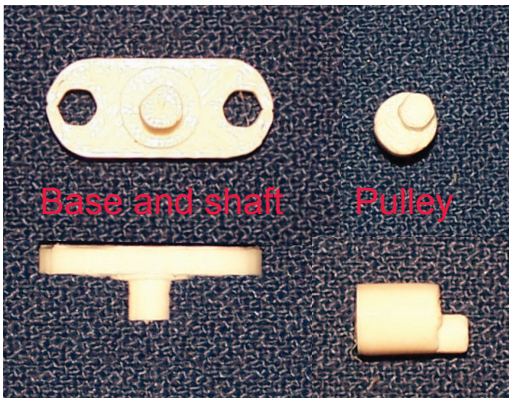

(c) Pulley and shaft design

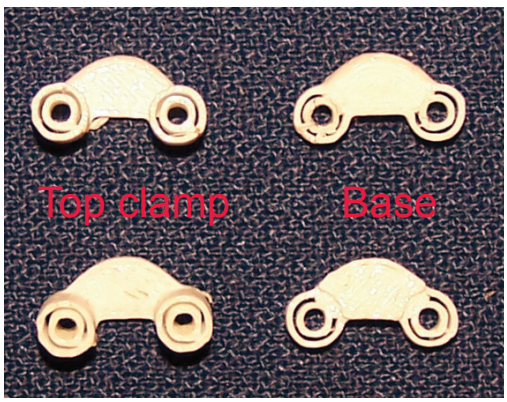

(d) Clamping design

Figure 4.11: The components of parallel compliant joint design and the CAD joint deisgn. Over 21 parts of the design are fabricated by 3D printer.

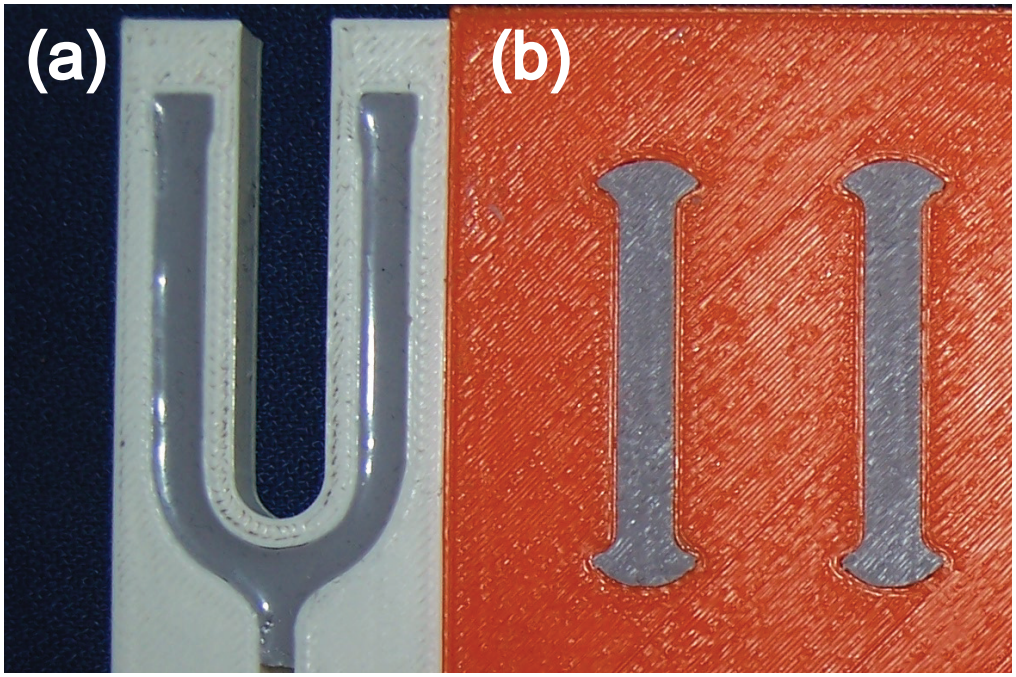

Figure 4.12: (a) shows the mold and shape deposition for the pre-tension mechanism, and (b) shows the compliant materials for testing the design of variable pulley configurations.

4.4 Experimental Setup

To validate the joint design, we built a test-bed to carry out experiments (Fig. 4.13). The joint is connected to an extended linkages mounted with a force/torque sensor (Nano25, ATI Inc, NC, USA) and a DC servo motor (NYNAMIXEL-RX-24F, Robotis, CA, USA) attached in parallel to the joint. The motor and sensor rotate together about the center of the joint such that the torque sensor acts as a rotary torque sensor to measure the resistances due to the system damping or the compliant material when the DC motor applies loading on the joint. The DC motor applied a sinusoidal amplitude loading as input to the overall system. A set of frequency is used to drive the system in the range of -100° to 100°. We tested the overall system in the following dynamic

conditions: (1) the joint without compliant material; (2) with different compliant materials; (3) with two pretension levels; and (4) with five variable pulley configurations. The goal of the first test is to identify the effect of damping and inertia on the overall system. The second test is to measure the effect of the compliant materials with different nonlinear stiffness on the resultant joint torques. The third and four test are carried out to validate the effect of pretension mechanism and the different pulley pair configurations on the adjustment of joint torque profile. The joint torques and joint angles for each tests are collected through a universal series bus of the data acquisition system ($USB-6343$, X Series, National Instruments, TX, USA). MATLAB (MathWorks, MA, USA) is used to command the servo motor and to import the raw data for further analysis.

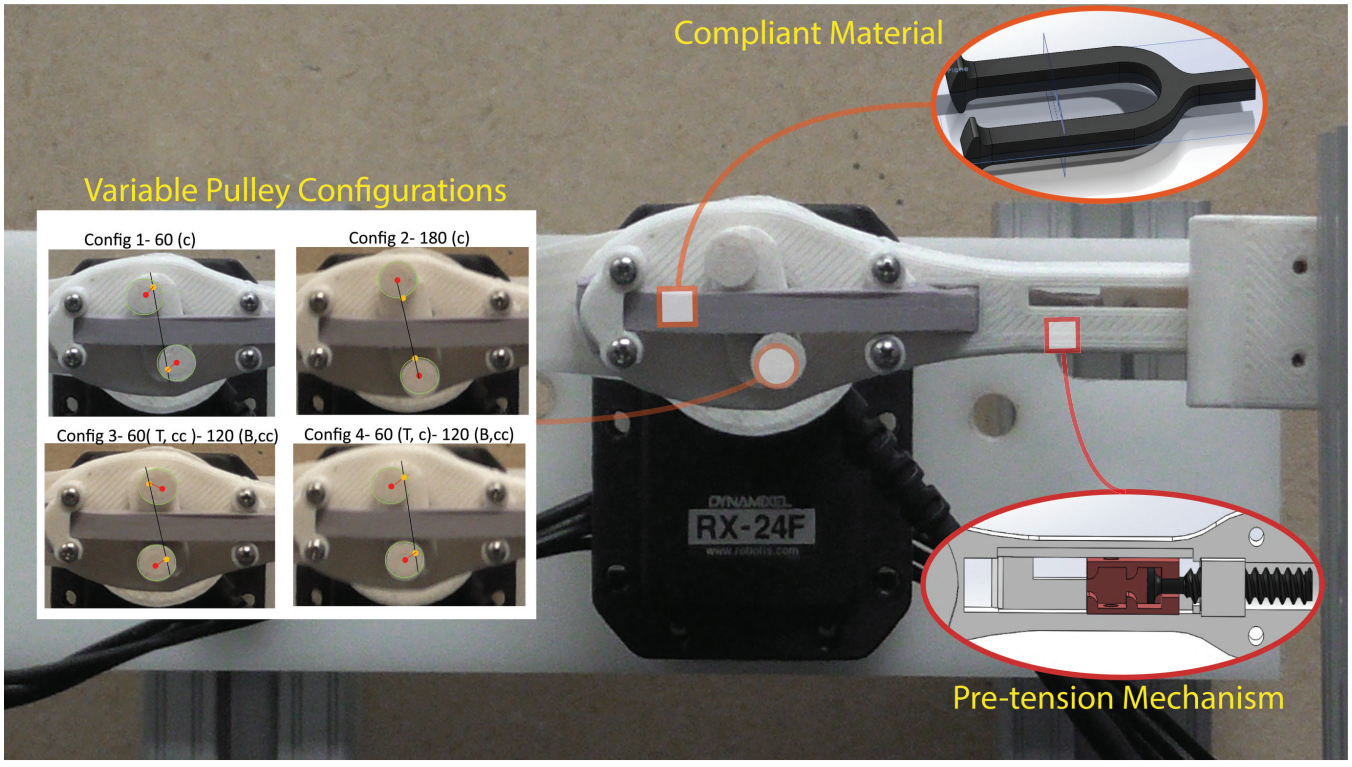

Figure 4.13: A prototype of parallel compliant joint mechanism. Subsystems such as compliant material, variable pulley configuration, and pre-tension mechanism are shown in subfigures.

4.4.1 System Damping Identification

Our experimental setup allows us to directly measure the resistance torques generated from energy dissipation components and compliant structures. This will allow us to determine if the proposed joint exhibits significant damping. We measured the damping torque for each frequency during the free drive test.

We then used linear stepwise regression to model the damping torque as a function of θ_d, $\dot{\theta}_d$, and f. A quadratic model which includes an intercept, linear terms, interactions, and squared terms are selected as candidates in the progressive model enhancement. We also simplify the model by calculating the t values to infer the significance of each term. The coefficient of determination (R^2) and root mean square error ($RMSE$) are used to evaluate the goodness of fit. The damping model is used to investigate the energy loss at the joint design, and to estimate the effect of variable joint compliance when we carry out the tests for different pretension and pulley configured conditions. The joint compliance can be derived from:

$$\tau_{ppc} = \tau_{ext} - \tau_B \tag{4.28}$$

where we derive the joint torque due to the compliance τ_{ppc}.

4.5 Results

4.5.1 Nonlinear Material Properties

The results showed that the six materials presented nonlinear stress and strain relationships during the tensile test (Fig. 4.14(b)). The engineering stress-strain curves are linear (Fig. 4.14(a)) if we considered the cross-section area and length change did not change substantially when loaded,

which might not be a case in large deformations among six materials. The material P series seemed to have smaller ranges of linear elasticity, and smaller Young's moduli compared with the material S series (Table 4.3). We also observed that the material P series are relatively ductile with longer elongations compared with the material S series. In general, all of testing materials had fairly large extensions. For example, if we assumed that the materialS_2, which was the brittlest, had an initial length 60 mm, the material based on its maximal true strain ($\epsilon_{true} = 1.5$) can reach a extension about 150 mm and a excursion 90 mm without rupture. We also tested the materials with cyclic loading with velocity 50, 250, and 500 mm/min. The hysteresis loops from these tests were not substantial. The power function was used to fit the experimental data of stress-strain curve for each material (Table 4.4). The results showed a close goodness of fit for each material. The models were used to estimate the tension generation when the materials were stretched due to the joint rotation. The compliant materials are typically considered viscoelastic materials. However, from our experimental observation, the tested materials show negligible viscous damping effects so we can treat the materials as elastic components. In general, the Young's moduli of the tested materials can be used if the tensile strains did not reach over their linear regions in Table 4.3. In our study, the elongation due to the joint rotation reached beyond the linear region, so we adopted the nonlinear power model to describe the force generation for each materials.

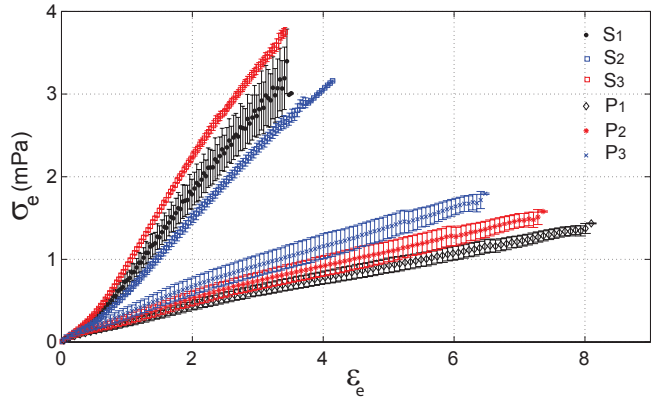

(a) Engineering stress-strain curve

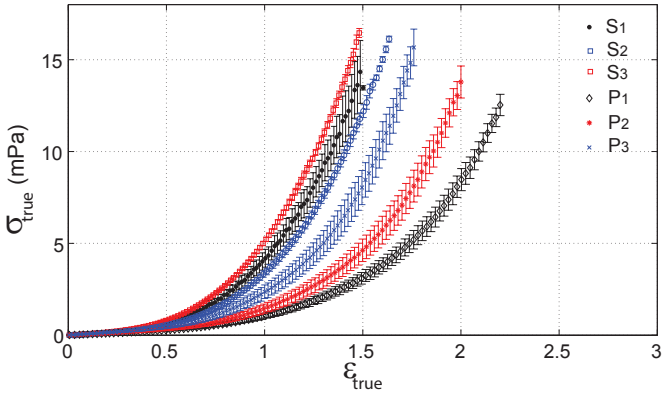

(b) True stress-strain curve

Figure 4.14: The stress-strain curves of six materials during the tesile test. The curves and their errorbars represent the mean values and standard deviations of five specimens for each material.

Table 4.3: The estimated Young's moduli of testing materials at the linear regions. E_s is the engineering Young's modulus. E_t is the Young's modulus at the linear region of nonlinear stress-strain curve for each material.

Type	E_e (mPa)	E_t (mPa)	ϵ_l	Linear region
P_1	0.182	0.463	0.191	8.66%
P_2	0.257	0.574	0.146	10.32%
P_3	0.531	0.712	0.128	13.81%
S_1	0.912	0.909	0.341	22.7%
S_2	0.913	0.929	0.349	23.58%
S_3	0.763	0.763	0.337	20.61%

Table 4.4: Fitting parameters and goodness of fit of the nonlinear stress-strain model, $\sigma_t = A\epsilon_t^B$, for each material.

Type	A	B	SEE	R^2	RMSE
P_1	2.229	3.362	4.972	0.99	0.225
P_2	1.653	3.414	5.58	0.99	0.328
P_3	2.102	3.455	6.135	0.99	0.269
S_1	4.184	2.994	1.623	0.99	0.129
S_2	4.281	2.896	0.663	0.99	0.082
S_3	3.361	3.167	1.231	0.99	0.112

4.5.2 Joint Torque Profiles with Different Materials

The joint exhibited a human-like double exponential profile of joint torque during the dynamic tests. Fig. 4.15 shows the results of the joint torque profile with different compliant materials implemented at the joint. The S series materials were used to investigate the resultant joint torques during the dynamic tests with the increased frequencies. We also compared the experimental results with the theoretical models which are based on each nonlinear elastic models (Table 4.4). The torque results did not change significantly with increased frequency of the sinusoidal loading. This implies that the selected material S series did not change the elastic behaviors with the loading frequencies.

The results also show that the different elasticity in S series material convey the nonlinear effect on the joint torque profile. The experimental values are slightly larger than the mathematical models for predicted the nonlinear stiffness of the material S_1 and S_2, but still matched the predicted model closely. Although, we observed that there were small hysteresis loops due to the viscoelasticity of the materials (Fig. 4.15), the energy dissipation effects were small enough to be ignored.

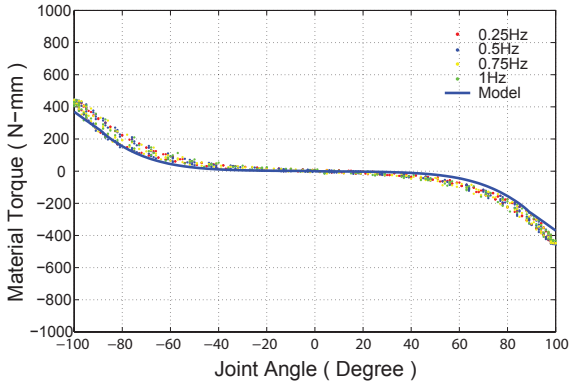

(a) Material S_1

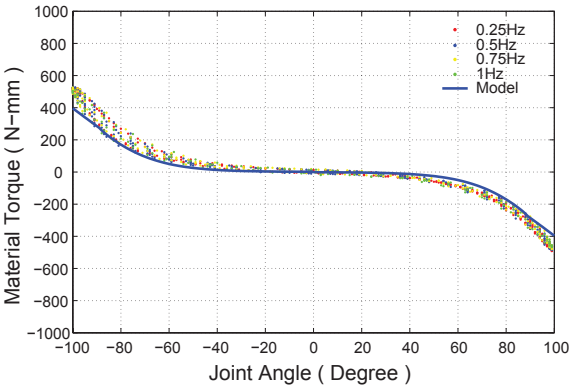

(b) Material S_2

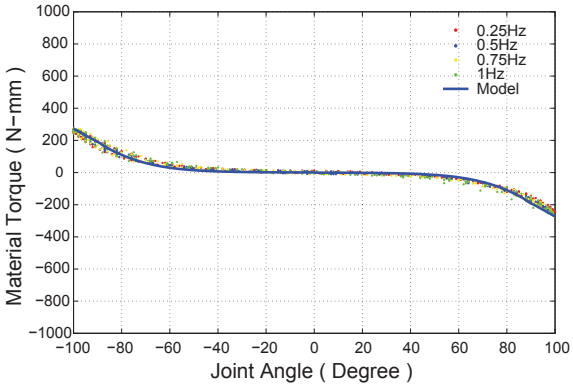

(c) Material S_3

Figure 4.15: The joint torque responses from the harmonic test with different cyclic frequencies for three S series applied materials.

4.5.3 Damping Model

The damping torque at the joint was fairly small ($< 20Nmm$) when compared with the joint compliance torque generated from the material. The regression model fitted the estimated damping torque closely (Table 4.5). Although we eliminated the terms of the model whose t values were smaller, the simplified model $\tau_{damping} = a_1\theta + a_2\theta f$ still showed a good fitting with the estimated damping torque. Therefore, we used this simplified model to describe the damping behavior of the joint. The model was finally used to estimate the joint torque due to the compliant configuration.

Table 4.5: Statistical results and coefficients of regression model fitting. pValue showing $< .005$ means that the coefficient is extremely significant.

Regression Model=$a_0 + a_1\theta\omega + a_2\theta f + a_3\omega f + a_4\theta^2 + a_5\omega^2 + a_6 f^2$				
coefficient	Estimate	SE	tStat	pValue
a_0	-1.8471	0.3667	-5.0366	$5.3646e-07$
a_1	$-2.3664e-05$	$8.0362e-06$	-2.9447	0.003287
a_2	0.098936	0.0048354	20.461	$1.7036e-81$
a_3	0.013659	0.001903	7.1777	$1.1528e-12$
a_4	-0.0015309	$3.8218e-05$	-40.057	$1.4668e-233$
a_5	$-2.0853e-05$	$2.3108e-06$	-9.0243	$5.8966e-19$
a_6	-38.125	1.5143	-25.177	$1.8923e-115$
Goodness of fit: $R^2 = 0.973$, $RMSE = 2.41$				
Simplified Model=$a_1\theta + a_2 f + a_3\theta^2 + a_4 f^2$				
coefficient	Estimate	SE	tStat	pValue
a_1	-0.088058	0.0019178	-45.915	$8.565e-281$
a_2	44.039	1.1989	36.732	$5.8185e-207$
a_3	-0.0014044	$3.5525e-05$	-39.533	$1.2354e-229$
a_4	-31.484	1.3604	-23.144	$1.7146e-100$
Goodness of fit: $R^2 = 0.885$, $RMSE = 3.58$				

4.5.4 Modified Torque Profile

Tuning the pulley rotating angle and the configurations substantially changed the slope and flat region of joint torque profile (Fig. 4.16). The results showed that, with the clockwise rotation for both pulleys (Fig. 4.16(a)), the joint torque changed the effective moment arm leading to a steeper torque profile in the flexion direction (joint angle > 0 degree). The joint torque profile also became shallower in extension direction (joint angle < 0 degree). Fig. 4.16(d) shows the joint torque results when the pulleys were rotated with a counter-clockwise direction. We found that this pulley configuration reversed the effect on the slopes of joint torque profile which is shallow in flexion and steep in extension. Fig. 4.16(b) demonstrates a change of contact phase between the pulleys and material in a sense that the flat region, which had zero force generation, shifted or widened the torque curve based on the rotating angles. Also, the joint torque profile was extremely steep when we tuned the pulleys to the maximal angle, $\theta_d = 180°$. This is the example of maximizing the effect of pulley configuration on the flat region and torque slope. However, for those configurations which changed the rotating angle with opposite directions between pulleys, the effect seemed to be eliminated (Fig. 4.16(c) and 4.16(e)). We observed that the compliant material was slightly compressed by the pulleys and spacers in the configuration 2, when the pulleys and spacers aligned. Overall, the results were promising with smooth internal motion of the pulleys and no irregular joint torques.

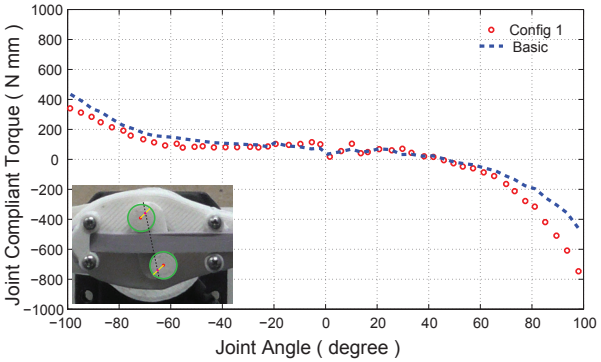

(a) Config. 1: Top and bottom 60°(+)

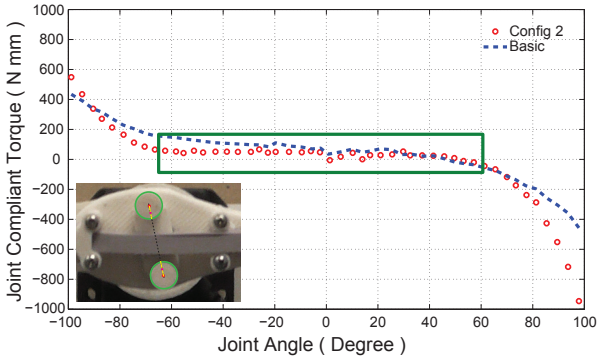

(b) Config. 2: Top and bottom 180°(+)

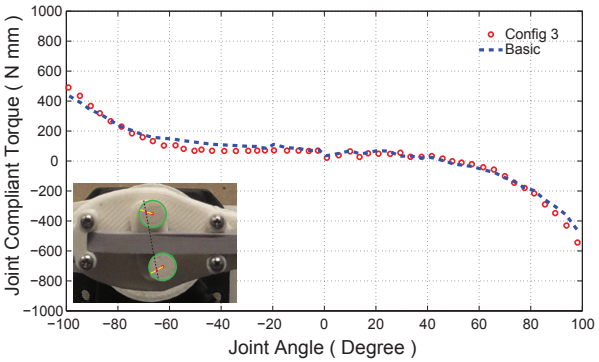

(c) Config. 3: Top 60°(−) and bottom 60°(+)

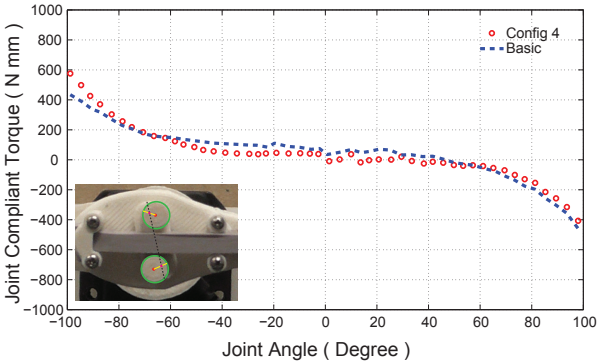

(d) Config. 4: Top 60°(−) and bottom 120°(−)

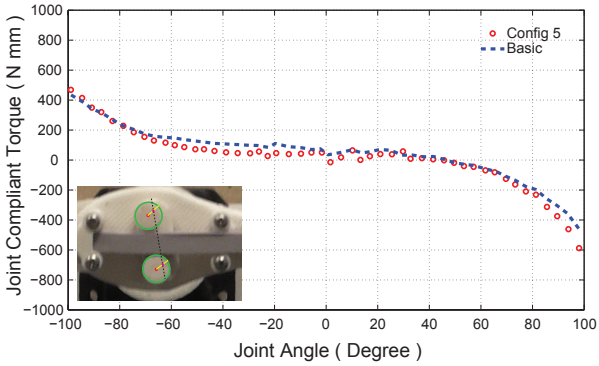

(e) Config. 5: Top 60°(+) and bottom 120°(−)

Figure 4.16: Experimental joint torque results of tuning pulley angle and rotating direction.

4.6 Discussion

We have presented a miniaturized robotic joint design that exhibits human-like passive joint torque. The mechanism has a custom-made compliant material and a set of pulleys that stretch the compliant material to generate nonlinear torque profile. Adjustable pulley configurations and a pretension mechanism allow for modification in torque profile to match the desired human-like torque profile.

4.6.1 Custom-made materials for compliant robotic hands

In this design, we provide a set of compliant materials for applications of designing soft robots. Use of the nonlinear elastic materials led to decrease in the weight and size of joint structures, and it also eliminated unnecessary energy dissipation that may happen with complex designs. Additive manufacturing procedure provided us the freedom to create any intricate geometries of the parts leading to a more compact joint mechanism. The elastic materials produce nonlinear resistive force for a wide range of motion of the joint, and the nonlinear joint stiffness achieved with the circular geometries of design elements. The design exhibits consistent torque production regardless of the increase in harmonic loading, implying that the passive force provided by the compliant material remains stable during the dynamic test. It also can be observed from the cyclic loading during the initial material test which shows that the elastomer does not change its elastic behavior significantly during the dynamic tests. Previous robotic joint designs have used linear springs to create nonlinear joint compliance with cam designs (Accoto et al., 2012; Carpino et al., 2011). However, the linear spring usually has a limited operating range, lateral vibration, and single action direction when it is stretched or compressed. Our work shows that adopting customized compliant materials as alternative can resolve the problems and can be beneficial for other compliant robotic

designs.

4.6.2 Tunable Joint Torque Profiles for Specific Joint Feature

The design of variable pulley configurations allows for the tuning of the torque profile. Changing the pulley angle and its rotating direction adjusts the joint torque in such a way that: (1) increasing rotating angles for a pulley will increases the joint stiffness, (2) pulley rotation angle and direction also affects the timing of engagement of the material in both directions. When the pulleys are moved away from the material, the flat region extends for the joint torque profile (Fig. 4.16(b)).

Based on those features, any arbitrary exponential-type of torque profiles can be realized through our design and tuning process. For instance, three joints at the index finger of the human hand have different joint torque profiles. To design a human-like passive compliant robotic finger, we plan to match the range of motion, joint stiffness at different rotating direction, and the joint slack position are for individual joint. By adopting the joint design we developed in this chapter, the passive joint compliance for individual joints that we aim to mimic from biomechanical observation can be realized through the optimization progress. We have developed a novel robotic manipulator which implements three passive parallel compliant joints (See Chapter 5).

4.6.3 Manufacturing Errors

The inconsistency of experimental results with the theoretical model may be due to a slight deformation of the shafts and pulleys from higher resistance of compliant material at large rotating angles. The future design will need to resolve following issues:

- Consider different types of printing materials to prevent large deformation of critical parts.

- Modify the design for some critical parts such as shaft-base-pulley connections.
- Increase the accuracy of fabricating the material to prevent the material from slacking between pulleys.

4.7 Conclusion and future works

We have developed a miniaturized joint design with the human-like passive joint compliance. The design is compact with low friction, and is light in weight which allows for implementing it to the robotic fingers. Key features of the design include the multiple options for custom-made compliant materials with nonlinear stiffness, the pretension mechanism, and adjustable pulley configurations which allows for tuning of the torque profile. Addictive manufacturing allows for fabricating complex and small mechanism parts, fast prototyping, and testing. In the following chapter, we will introduce transfer of the design to develop a novel robotic manipulator in grasping and manipulation tasks.

Chapter 5

Design and Control of Human-like Fingers with Passive Nonlinear Parallel Compliance

5.1 Introduction

With the goal of achieving better grasping and manipulation, in this study, we focus on a design and control of a novel robotic finger which has the human-like passive joint compliance (Fig. 5.1). The passive nonlinear parallel compliance (PPC) we have developed previously was implemented into the each finger joint and series elastic actuation (SEA) was developed to achieve force control. Passvie joint compliance has been shown to reduce the energy consumption by minimizing the sum of the actuation torque (Borràs and Dollar, 2014). It has been shown that adding linear joint compliance can improve the stability of manipulation for delays due to the sensing (Niehues, 2014).

Passive compliance has been implemented in robotic design (Marques et al., 2010; Pfeifer et al., 2012; Kim et al., 2006, 2008). but, there exist only a few examples of robotic fingers with passive compliance. These include the SDM Hand (Dollar et al., 2010), SPRING Hand (Carrozza et al., 2004), UB Hand 3 (Lotti et al., 2005), Karlsruhe hand (Pylatiuk et al., 2004; Kargov et al., 2007), and the DLR Hand (Grebenstein and van der Smagt, 2008; Grebenstein et al., 2010). The iLimbs prosthetic hands used linear springs across the PIP joints to create passive joint compliance in flexion, however, the joint compliance in extensional direction was not available. The compliance

in these robotic and prosthetic hands is typically invariant of the configuration, and is designed to achieve limited robustness during position control. In many cases the passive invariant compliance is deemed detrimental to achieving favorable position controls.

To date, the effect of passive nonlinear compliance on the grasping or manipulation in robotic hands is still not clear. Although the study has shown that the linear parallel compliance reduces the force requirement from the motor in parallel manipulator (Borràs and Dollar, 2014), the grasping stability with the nonlinear parallel compliance remain unknown. The stiffness analysis for robotic hands has been used to evaluate the stability of grasping (Cutkosky and Kao, 1989). Understanding the stiffness at the joint and Cartesian space, we can investigate the relative contributions of the nonlinear parallel compliance to the grasping stability at different configurations. During the grasping and manipulation, the external force/disturbance is always expected. The interaction between the robot and external force that could cause any instability needs to be investigated. Especially, with a configuration dependent compliance at the multiple finger joints, the stiffness contribution to the grasping stability is critical.

In this chapter, we present a design of human-like compliant robotic finger, and we carry out a stiffness analysis to understand the effect of adding nonlinear compliance in robotic hands. To validate the design, we integrated the two-finger manipulator with a series elastic actuator (SEA) subsystem for force control.

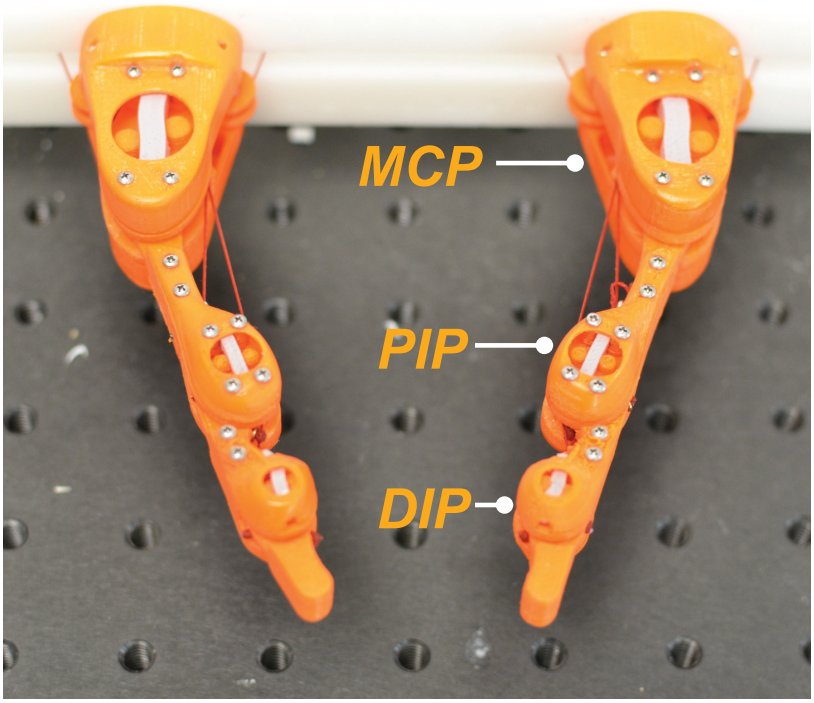

Figure 5.1: A novel design of compliant fingers which incorporates with the human-like parallel compliance inspired from the biomechanical features found from human hands study (Kuo and Deshpande, 2012). The MCP, PIP, and DIP express three finger joints as a sequence from the proximal to distal segment.

5.2 Design of PPC Tendon-driven Fingers

5.2.1 Passive Parallel Compliance for Robotic Fingers

It was found that the passive joint torques at the MCP, PIP, DIP joint of the index fingers have exponential tendencies, but with diverse results in terms of torque amplitudes, slopes, and neutral/zero torque positions for different subjects (Kamper et al., 2002). From the perspective of prototyping a robotic hand, we designed three arbitrary PPC joints in a sense that keeping these three joint torque profiles the same, but scale the profiles by the decision of finger geometrical

dimensions. The joint stiffness profiles for the three joints are shown in Fig. 5.2. The MCP joint is the default joint stiffness, and we scaled the MCP joint profile with a ratio 0.4 and 0.2 for the PIP and DIP joint, respectively.

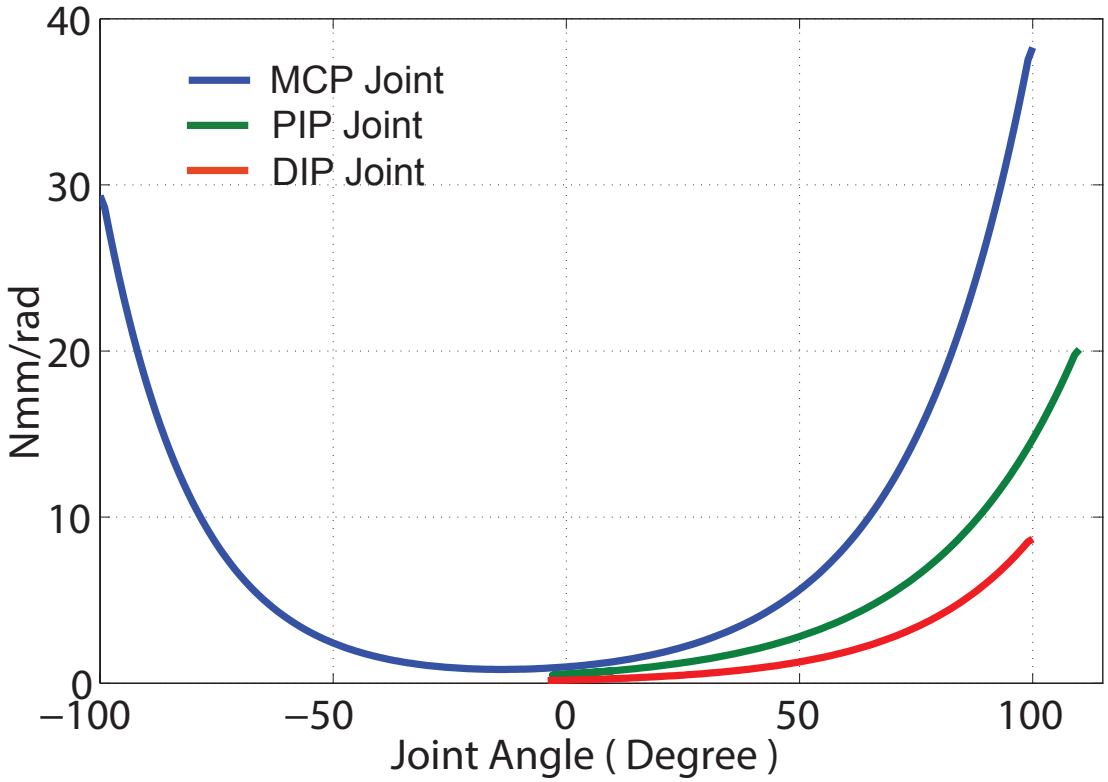

Figure 5.2: The joint compliance profiles for the three joints. The range of motion for the MCP joint is decided from $-100°$ to $100°$, and for the PIP joint from $-4°$ to $114°$.

5.2.2 Finger Structure

Fig. 5.4 shows the tendon-driven finger design that mimics geometrical structure and kinematic function of the index finger. There are three degrees of freedom in the finger robot ($N = 3$). The first two and the third joints correspond to the metacarpophalangeal (MCP), proximal inter-

mediate phalangeal (PIP), distal intermediate phalangeal (DIP) joint of the human's index finger, respectively. The finger can move in the two dimensional plane, and each joint is designed as the revolute joint based on the miniaturized joint design. The range of motion for each joint is $[-100^\circ \sim 100^\circ]$ for the MCP, $[-4.1^\circ \sim 110.5^\circ]$ for the PIP, and $[-14^\circ \sim 72^\circ]$ for the DIP from extension to flexion. Two bearings were installed in each joint. The CAD designs in Fig. 5.3(a) and 5.3(b) show a compact design of the robotic finger. A human bone-like segment is developed to decrease the weight, and to reserve the space for the tendon pathway. The internal pulleys for each joint are designed to fit into the joint space compactly. The dimension of the pulleys are based on the scaling and calculation of geometrical model that we have developed previously.

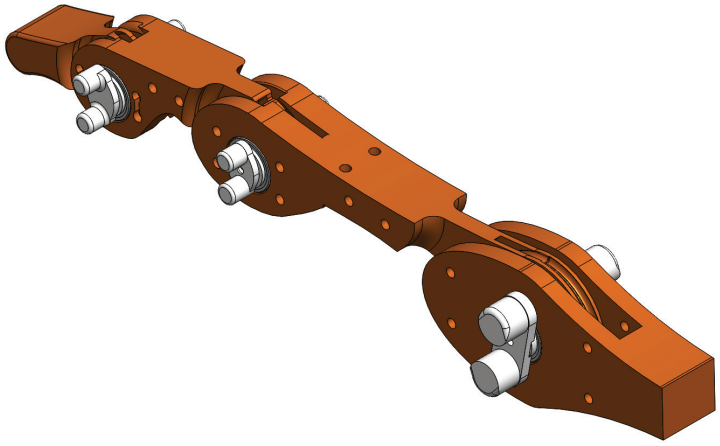

(a) 3-D isometric view

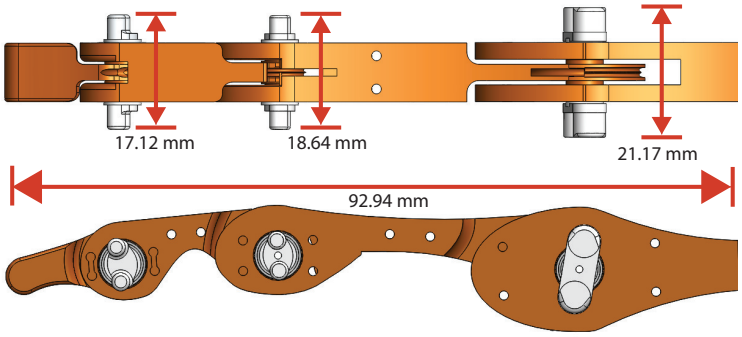

(b) Top and side view

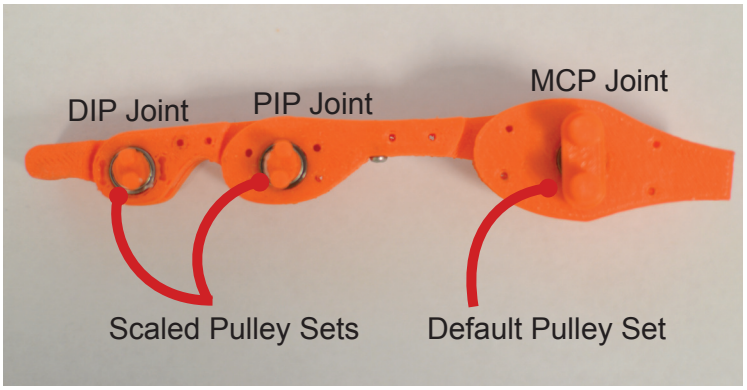

(c) Built structure

Figure 5.3: The CAD design and the dimensions for the finger structure.

5.2.3 Casing Design for Compliant Materials

We designed three cases to secure the compliant material at each joint, and to protect the pulleys at the operational spaces. We created nonuniform surface planes to reduce the weight and size of design following the contour of the bone structure. We carefully adjusted the dimension and thickness of each case to ensure that there was no interference between the pulleys and casing walls. The spacers designed for the compliant joint were inserted in the cases to reduced space and assembly complexity. For the MCP and PIP joint, we designed a miniaturized clamp structure to secure the compliant material in place by merging the clamps to the both sides of the spacers (Fig. 5.4(c)). Given clamping pressure during the assembly, the clamps can press the compliant materials, and prevent the materials slip off while rotating the joint. Space of the DIP joint is extremely limited for any clamping mechanisms to be built, so we modified the internal structure of the DIP case to secure the compliant material. The screws were used to secure the casing on the finger structure.

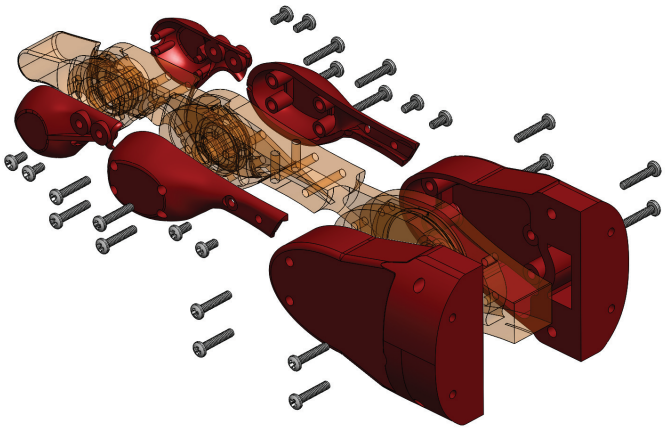

(a) 3-D isometric view

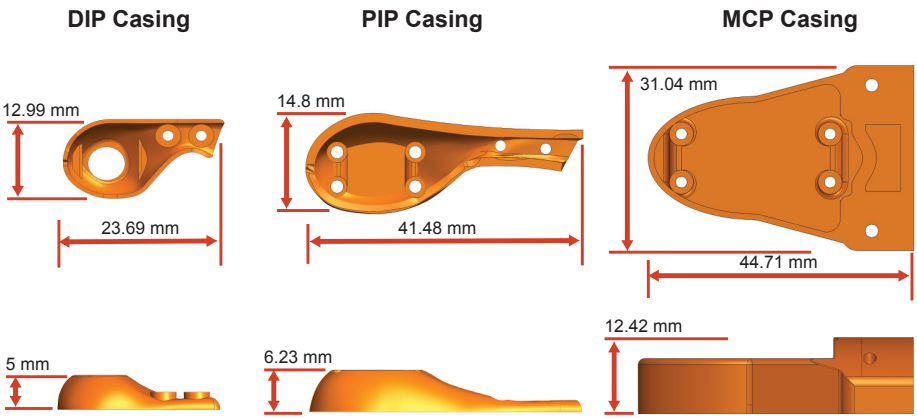

(b) Outside and inside view

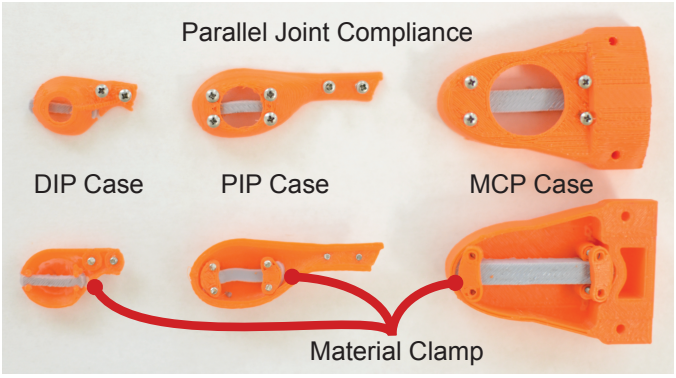

(c) Built structure

Figure 5.4: The CAD design and the builds of the casing for the MCP, PIP, and DIP joint.

5.2.4 Finger Assembly

Fig. 5.5 shows the miniaturized finger design and a human finger as a sizing reference. The dimensions of the design are close to those of the real human finger. The weight of whole finger assembly is about 28 - 29 gram, which is also close to the weight of the human fingers (about 30 gram) (Esteki and Mansour, 1997).

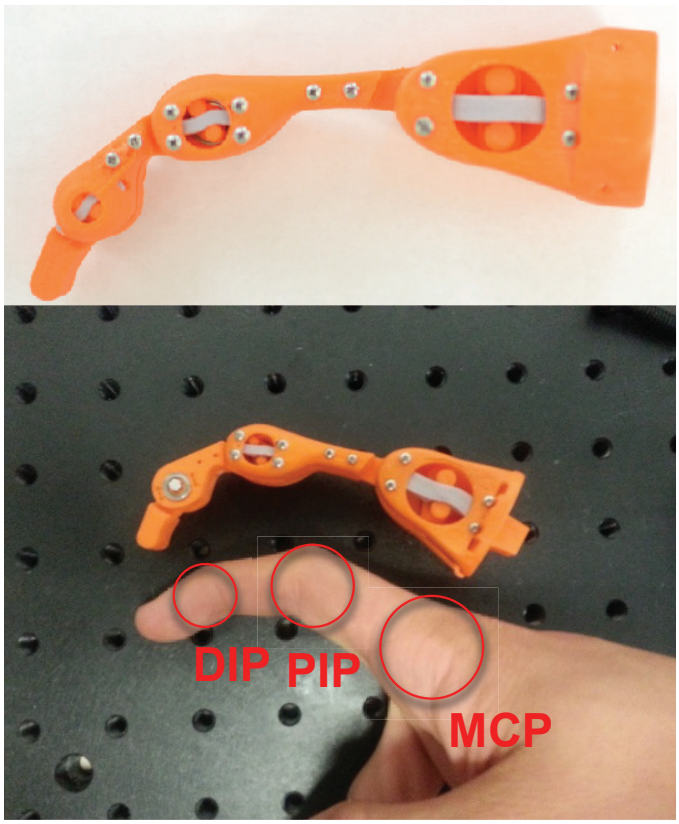

Figure 5.5: Assembly of the PPC finger design and a comparison between the robotic finger and human finger.

5.2.5 Tendon Routing

We implemented three tendon-driven mechanisms (TDM) into the finger design. Fig. 5.6 shows the routing of the tendons across the MCP and PIP joint, respectively. One extensor (EXT) was routed across the MCP joint in extension direction; one flexor ($FLEX$) was across the MCP joint in flexion and PIP joint in flexion direction; and a cross-over tendon (CO) was routed across the MCP joint at the flexion and the PIP joint at the extension, respectively. A coupling tendon mechanism (CTM) was designed to couple the DIP joint with PIP joint. Therefore, the rotation of DIP joint depends on the DIP joint, which decreases the degrees of freedom down to two for the finger. The coupling ratio for joint rotations was designed to approach the human-like joint kinematic dependency, whose ratio is about $1 : 1.1$ for the PIP and DIP joint. The moment arms decided by the constant radii of tendon pathways with respect to each joint dimensions are 9.5 for the MCP, 5.5 for the PIP, and 3.44 mm for the DIP. In order to ensure that the TDMs maintain constant moment arms during the rotations, we created a double groove at the joint along the tendon pathways so that the tendons lie on the different grooves to prevent the overlaps. Fig. 5.7 shows the tendon routing design and direction that tendons pass through the joint. The radii of the pulleys were carefully designed through the whole ranges of joint rotations so as to prevent the tendons from slipping out of the grooves. We also designed a guidance to keep the tendons in place while slacking. The re-directional pulleys for the TDMs were designed to transmit the tendon force and to avoid the change of moment arm at large joint angles.

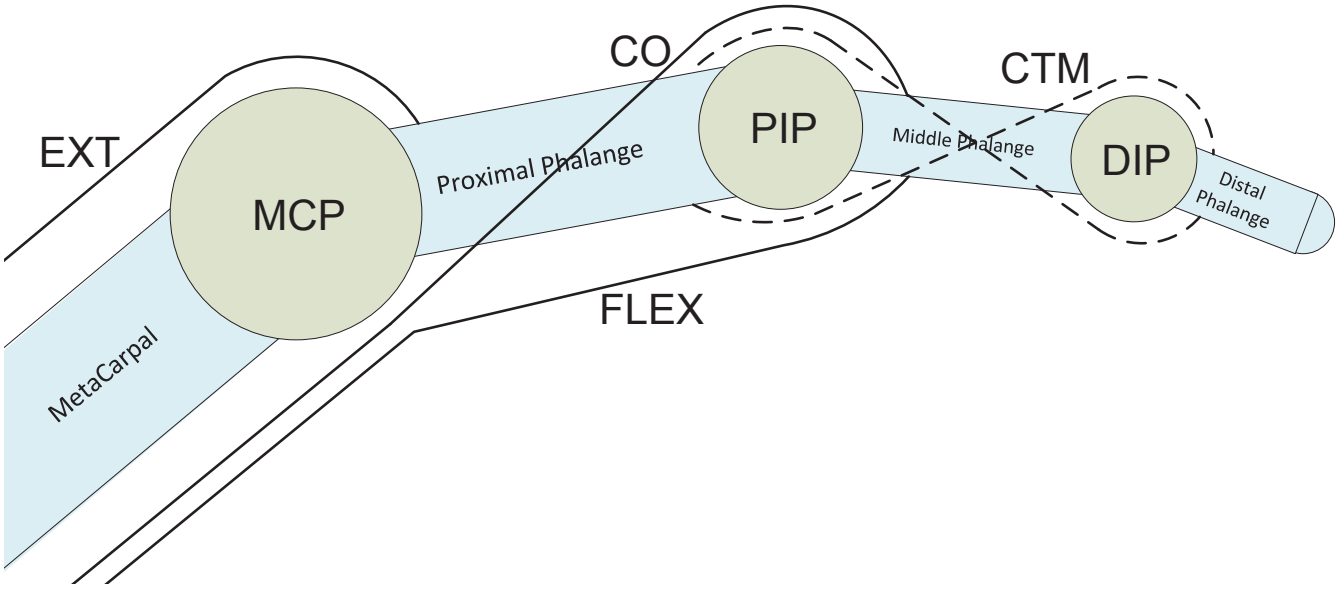

Figure 5.6: The tendon routing for the TDMs.

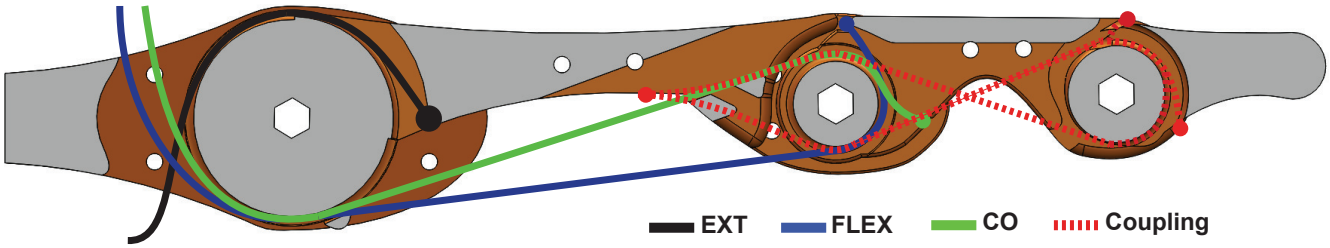

Figure 5.7: The grooves and hollow design of the internal structure for the TDMs. The dot points are the ties' locations.

5.2.6 Additive Manufacturing

The design of the finger takes advantage of the capabilities of fused deposition modeling (FDM) of printing technology (Replicator 2X, Makerbot, NY, USA). Acrylonitrile butadiene styrene (ABS) and dissolvable polystyrene are used to build the finger design simultaneously, because the

design has small dimensions and intricate details in geometry. This improves the ability to print interlocking structures with a great degree of liberty over the shape which allows for a simple and robust design of the manipulator. Also, it allows us to prototype quickly and at a low cost. In order to further improve the design, a novel technique is developed in order to include bearings and non-printed structures into a unified piece. This technique involves programmatically altering the G-code of the print to both create a void in which the bearings are placed, as well as to introduce an operational stop so that the pieces could be assembled before the printing process resumes. The entire process produces a robotic finger that is both strong and lightweight with the minimal backlash. This technique is utilized as the initial stage in manufacturing. The unified finger structure is printed embed with six placed bearings, and it is dissolved in limonene bath. Printed casing which have the added functionality of fixing the elastic elements are attached to the bare structure at each of the three joints.

We choose a nylon spectra fiber as the tendon whose maximal test load is 80 lb (Power pro, Honeywell, MD, USA). The tendons are threaded through the fully assembled robot, and are fixed by using a small brass washer to hold a sintered mass at the end of each length. Each tendon is routed around an idler pulley before wrapping across the motor shafts.

5.2.7 PPC Manipulator

We integrated two PPC fingers with six servo motor(Dynamixel RX-24F, Robotis Inc, Irvine, CA, USA). The overall system is shown in Fig. 5.15. We installed the manipulator on a mount that can be adjusted with different distances between the fingers.

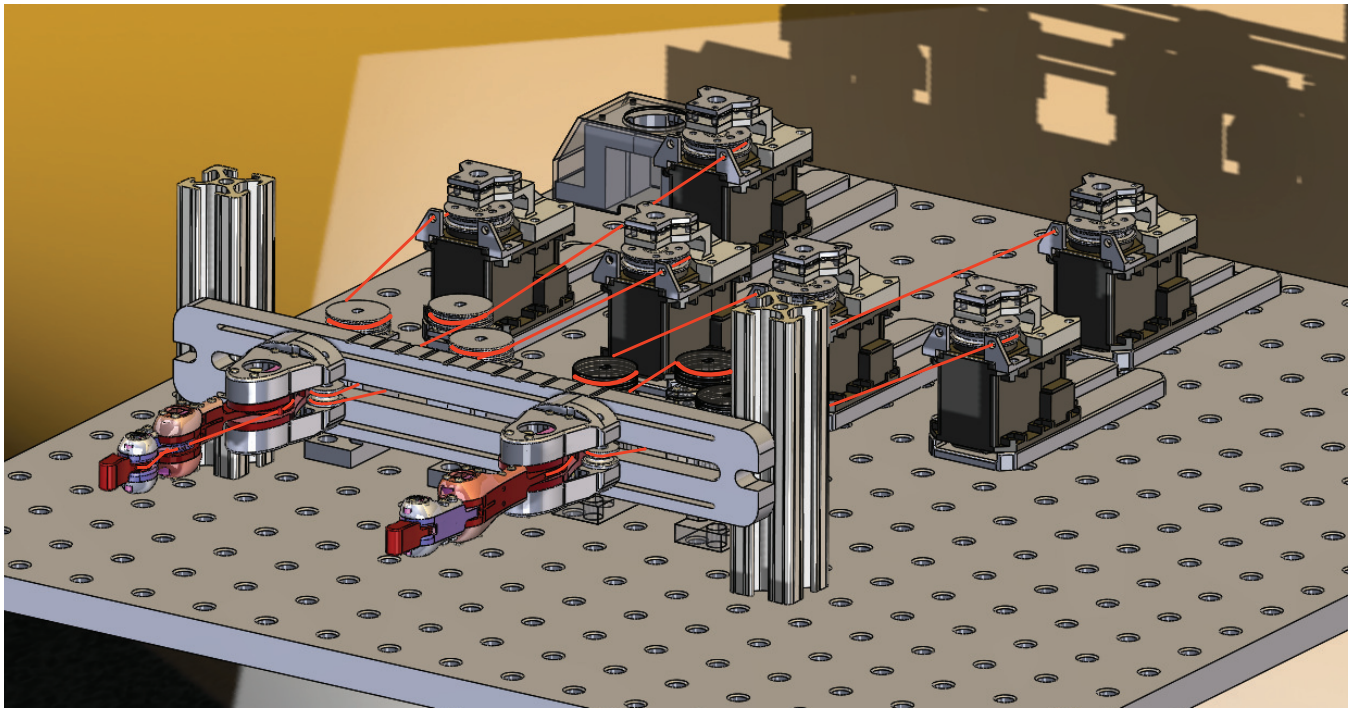

Figure 5.8: CAD design of overall system for the PPC manipulator which includes two fingers, tendon routing, and six SEAs.

5.2.8 Position Control for Grasping and Manipulation

Open-loop position control strategy was used to validate the design in grasping and manipulation tasks. Without any position or force feedback, the manipulator was executed for tasks such as pinch and power grasping, and also a circular manipulation. The finger was controlled by specifying a sequence of tip positions for the finger based on the shapes and dimensions of grasping objects. The trajectory of tip position was transformed by using inverse kinematics to determine the joint angles at the joint space for the MCP and PIP joint. A kinematic mapping from the joint space to the motor angles were carried out by using the moment arm matrix. In order to achieve a smooth motion, intermediate motor velocity are calculated using a central difference.

We validated the robustness of design in grasping and manipulation without position feedback. By using a motion capture system (PhaseSpace Inc, CA, USA), we captured the position data of two finger tips with six active LEDs placed on the MCP, PIP and the tip of two fingers. We compared the desired and measured trajectories of the finger tips for a circular, pinch, sinusoidal, and a rotation motion. We collected two trials for each motion.

5.2.9 Results of Trajectory Tracking

Fig. 5.9 shows that manipulator have great capability to grasp different shapes and sizes of the objects with just a open loop position control. For the pinch grasping, the manipulator can easily hold the objects (i.e. thumb drive to Ping pong ball) by adjusting the distance between two finger tips with the same trajectory. For the power grasping, we adjusted the MCP and PIP joint angles trajectories based on the object's geometries (i.e. tennis ball and square box). Fig. 5.10 shows a circular manipulation for a small pulley. The pulley was manipulated from the resting position to follow a circular path in counter-clockwise direction. The trajectories following with the desired motions were fairly good (Fig. 5.11). The tracking errors in the X and Y direction were less than 1 cm which showed a good trajectory tracking performance. Considering the errors caused from the misplacement of LED markers, mechanical system, and the open loop control without position feedback, the manipulator can still follow the desired position fairly well.

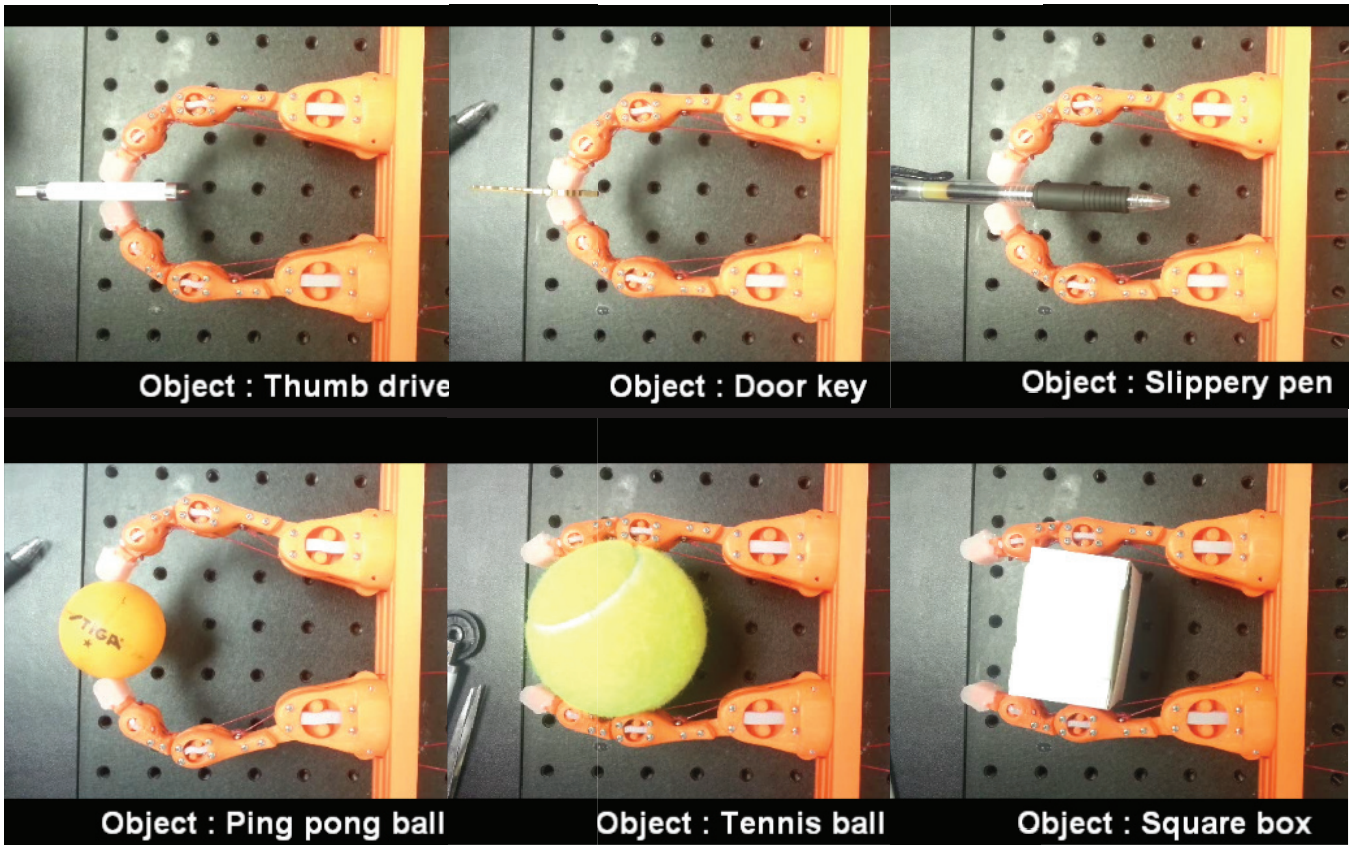

Figure 5.9: A demonstration of grasping with different objects.

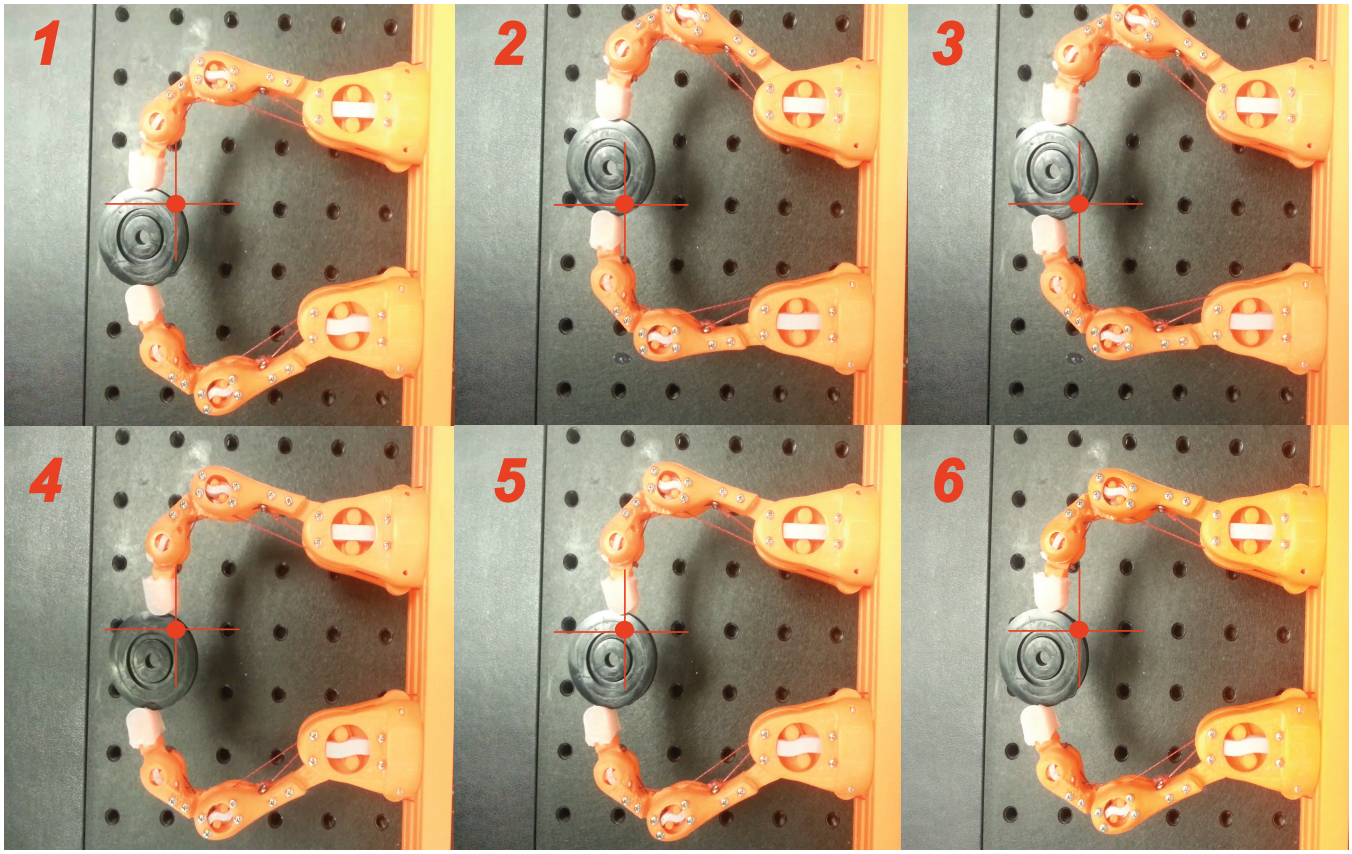

Figure 5.10: A demonstration of a small object manipulation.

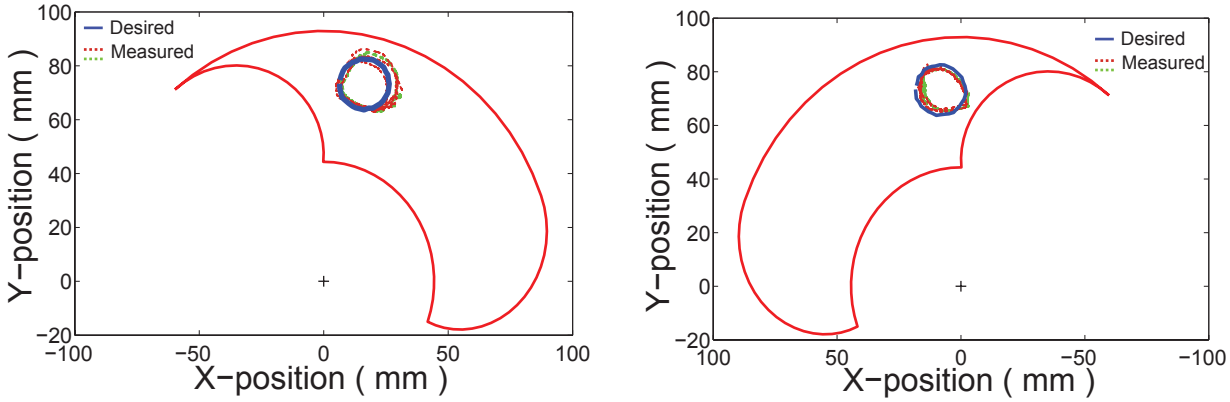

(a) Left finger circle tracking error mean: $\hat{X}_e = 6.7$ and $\hat{X}_e = 4.6$ mm

(b) Right finger circle tracking error mean: $\hat{X}_e = 7.1$ and $\hat{X}_e = 1.2$ mm

Figure 5.11: Comparison between the measured tip trajectories and desired X and Y position in circular manipulation. The red color countours show the areas of workspaces for the PPC manipulator. Two dash lines present the experimental data collected from the motion capture system.

5.3 Design of Series Elastic Actuation (SEA)

For the force control and elastic TDM actuation, we designed a series elastic actuation (SEA) system. The series elastic element consists of a linear spring, nylon fishing line, a servo motor, and 2 rotary potentiometers attached to a steel breadboard, as seen in Fig. 5.12. One potentiometer is mounted in parallel on the top of the servo motor, while the other is connected to an idler pulley. When the tendon is loaded by the system or the actuator at either side of SEA, the spring is stretched, and the differences between the pulleys' rotary angles can be converted to the spring extension as the radii of the pulleys are known.

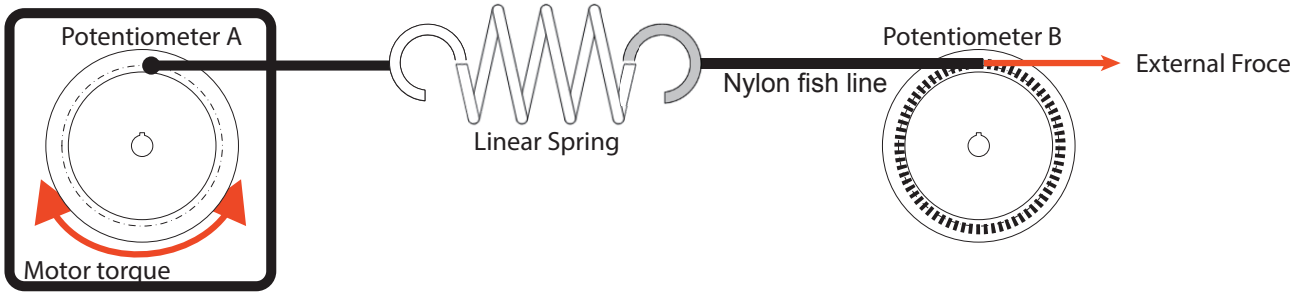

Figure 5.12: Schematic of a single SEA setup.

A CAD design of the SEA is shown in Fig. 5.13. A sandwich structure is designed to clamp down the two potentiometers, and to stabilize the shaft that penetrates through the potentiometers and also connects with the pulleys. We designed a set of tendon guides to keep the tendon on the track of the pulley when the tendon is slack. We developed a sliding mount for the servo motor to adjust the total distance of the SEA (Fig. 5.13 (a)). The radii of the pulley A and B are the same for the conversion of rotational angle to the tension excursion. We installed a bearing at the bottom of the base for the front set (Fig. 5.13 (b))to ensure the pulley can be rotated freely. The pulley has a spiral thread design to prevent the routing tendon from being slippery.

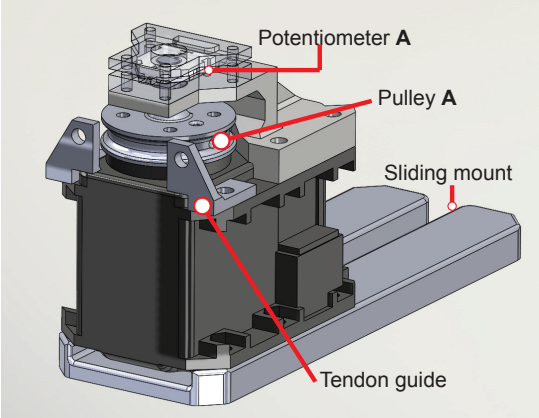

(a) CAD design for the SEA-motor

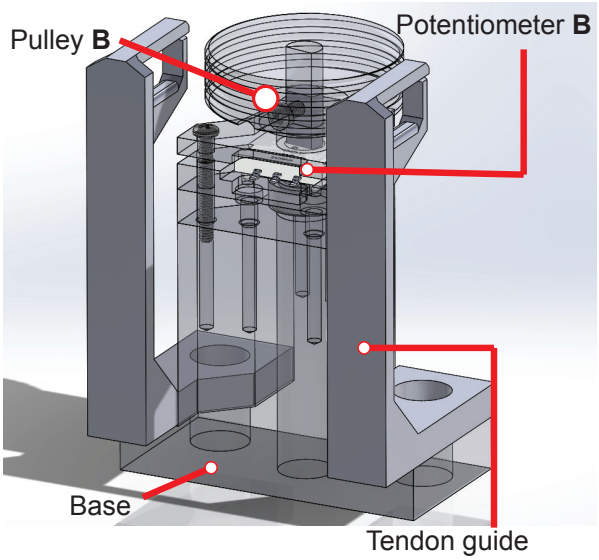

(b) CAD design for the SEA-front

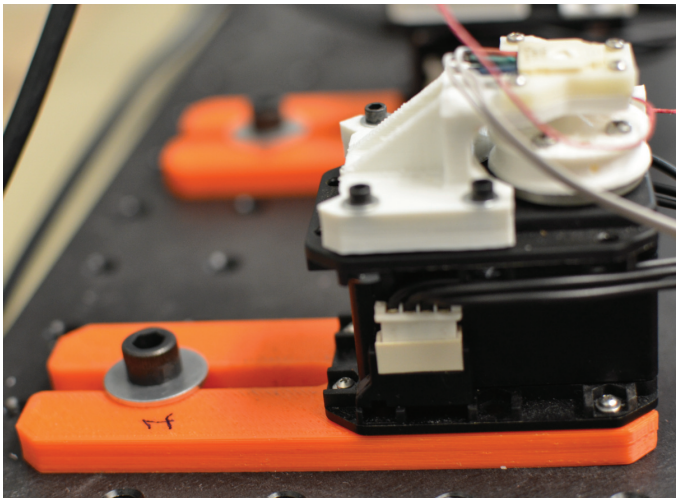

(c) The SEA-motor build

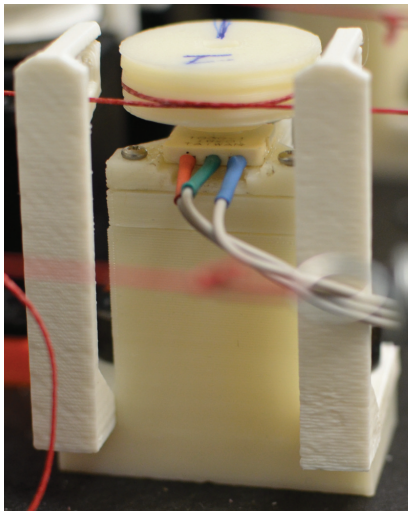

(d) The SEA-front build

Figure 5.13: Parts of SEA design. (a) shows the potentiometer A clamped on the top of the servo motor in parallel. (b) shows the front set of the sencing design for potentiometer B.

5.3.1 Force Control for the SEA Design

To validate the SEA, the output end of the tendon is routed to a fixed multi-axis force sensor (Nano25, ATI, NC, USA). A data acquisition system (USB-6538, National Instruments, TX, USA) is used to collect the voltage signals from the potentiometers. The tendon is preloaded to 2.5 Newton to overcome the spring initial tension provided by the manufactured vendor (Loading rate=1.69 lb/in, Jones Spring Co., KY, USA).

Fig. 5.14 shows a control block diagram for the SEA design. The proportional gain (K_p) is manually tuned to achieve the instantaneous response without overshoot. Three types of force trajectories were generated to test the response of the system: a step input, a sinusoidal input, and a linear chirp. A step input with 5 Newton, and a sinusoidal input with a amplitude 6 Newton with frequencies ranged from 0 to 1.6 Hz are applied to validate the dynamic responses of the SEA actuation. While simultaneously collecting force data from the froce/torque sensor and torque, the program also recorded the estimated forces based on the differential positions of two potentiometers.

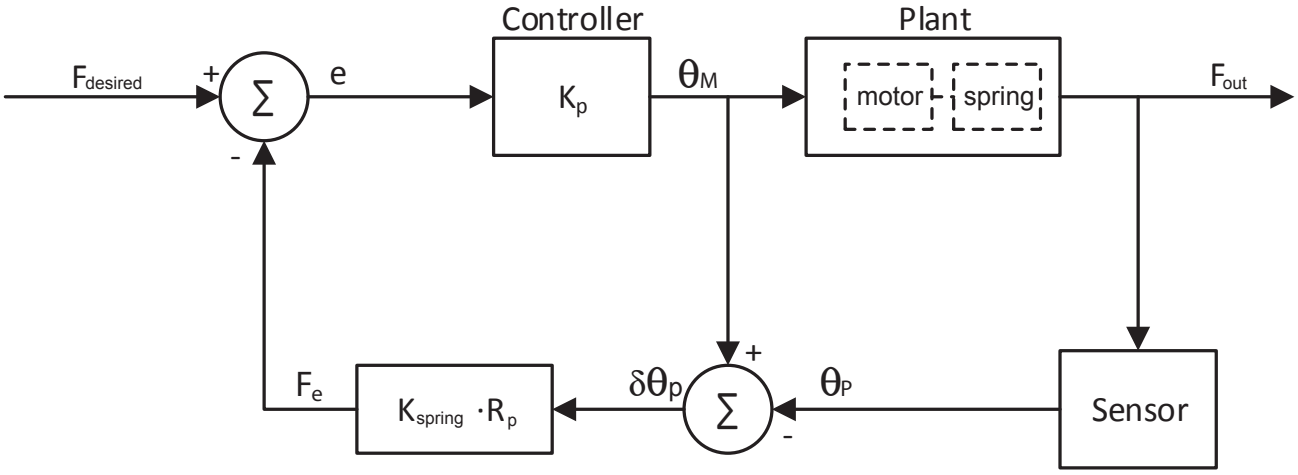

Figure 5.14: The control diagram for the SEA. The analog voltage signals reading from the sensors are converted to the joint joint angles (θ_M and θ_p). The estimated force (F_e) is derived since the spring extension is calculated with the known radii of the pulleys (R_p)).

We integrated the PPC manipulator with six SEA (Fig. 5.15). The arrangement of the SEAs connecting the tendons is based on the operational ranges that the tendons require. The tendon CO needs more excursion than the others so that we installed the CO-SEA behind the others tendon-SEA sets.

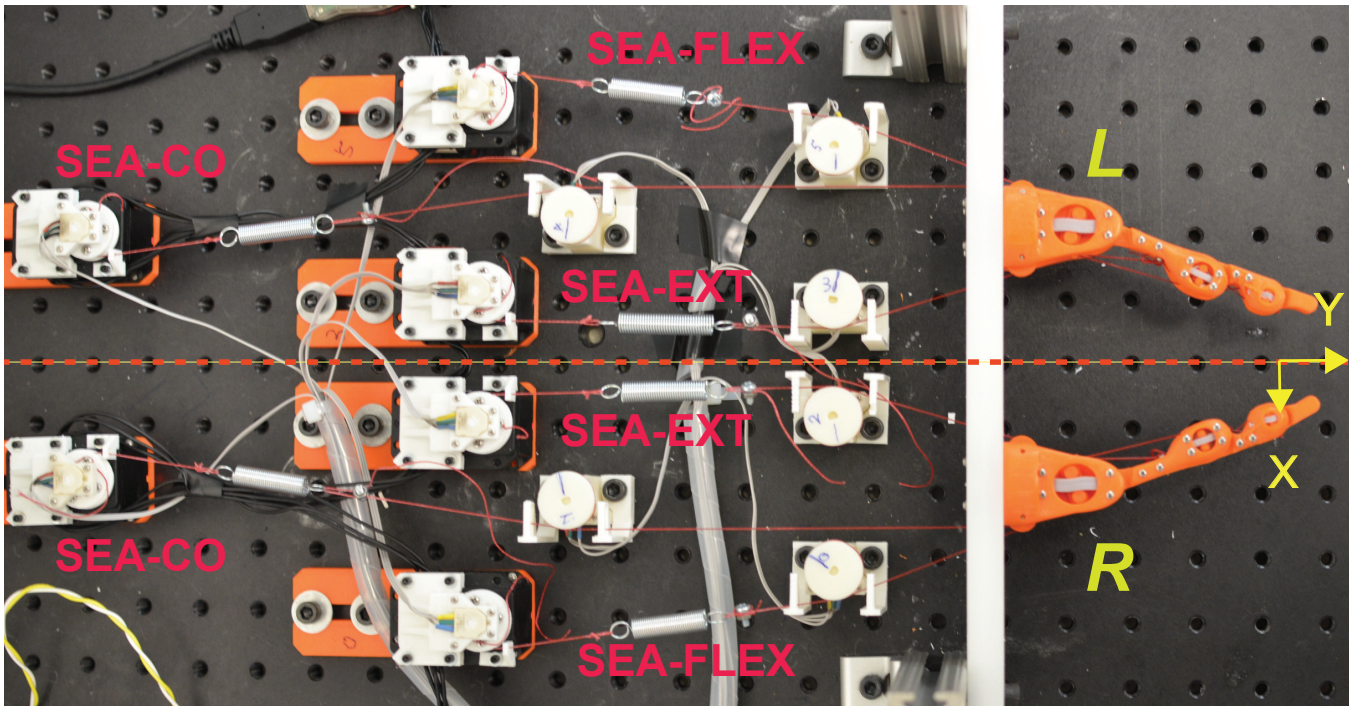

Figure 5.15: The overall system of PPC manipulator.

5.3.2 Results of SEA Validation

Results from the dynamic responses of SEA are promising under different input (Fig. 5.16). For the step input from 0 N to 5 N, which is roughly the maximum step we expected the system to endure, the system reached the desired value in about 0.3 seconds with minimal steady-state error (Fig. 5.16(a)). For the sinusoidal input, there was about 0.3 N of steady error between the measured and estimated force, but the estimated force can track the desired force closely (Fig. 5.16(a)). To test the systems response at higher frequencies, we generated a linear chirp input from 0 to 1.6 Hz (Fig. 5.16(a)). The response indicated that the SEA tracks well until 1.6 Hz, where the amplitude is reduced to about 71% of the nominal value. Therefore, the frequency at 1.6 Hz was considered

the cutoff frequency for this system, and bandwidth for the SEA is from 0 to 1.6 Hz. This results indicated that the SEA was robust to implement into the tendon-driven system, especially for the system such as the PPC manipulator which requires a low bandwidth. We primarily plan to operate the SEA at low frequency range and low magnitude trajectories in grasping and manipulation.

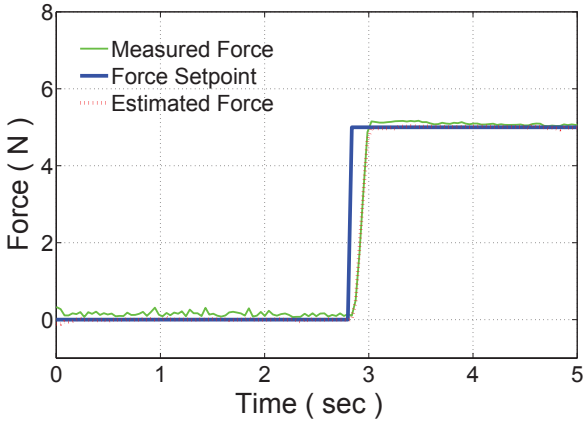

(a) Step response

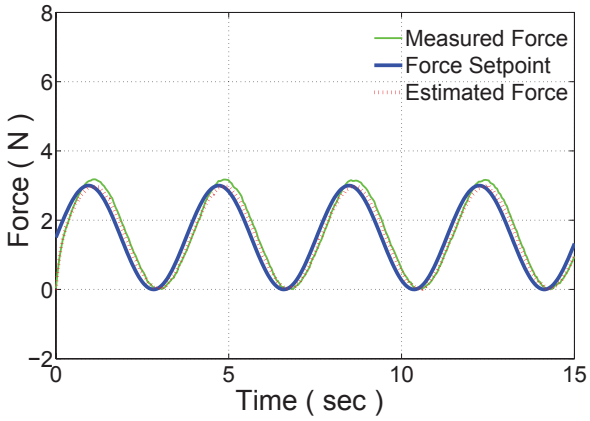

(b) Sinusoidal response

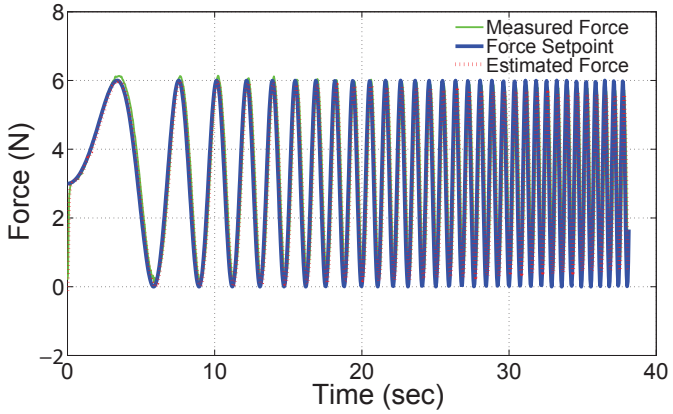

(c) Chirp response

Figure 5.16: Results of SEA validation. 5.16(a) shows the step response with a desired amplitude 5 N. 5.16(b) shows a sinusodial response with a desired amplitude=3 N and frequency=4 Hz. 5.16(c) shows the force tracking with a desired amplitude 6 N and very frequencies ranged from 0.25 to 1.6 Hz

5.4 Stiffness Analysis

We aim to control the grasp stiffness of the manipulator through the force control of SEA tendons. The goal of this section is to demonstrate a model that constructs the mapping from the tendon to the Cartesian space. Therefore, the quantities of the stiffness of grasping can be estimated.

5.4.1 Transformation of Joint and Cartesian Stiffness

The conventional formulation for the mapping of stiffness between Cartesian (K_p) and the joint spaces (K_θ) is with the Jacobin matrix J_θ:

$$K_\theta = J_\theta^T K_p J_\theta \tag{5.1}$$

Therefore, the desired Cartesian stiffness is:

$$K_p = J_\theta^{-T} K_\theta J_\theta^{-1} \tag{5.2}$$

However, this transformation is useful only if no external loading is applied on the end effector (Chen and Kao, 2000). In the case of robotic grasping and manipulation, the Cartesian stiffness at the end effector determines the stability of grasping objects as a desired input in stiffness or impedance control (Kao and Yang, 2004; Kao et al., 1997). The conservative congruence transformation (CCT) has been used to control the robotic manipulator (Chen and Kao, 2000) and to study the human motor control (Hu et al., 2011; McIntyre et al., 1996). The stiffness transformation can be expressed as:

$$K_p = J_\theta^{-T} (K_\theta - K_g) J_\theta^{-1} \tag{5.3}$$

where the K_g presents the effect of configuration-dependent Jacobin matrix (J_θ) and external force (F_{end}) on the Cartesian stiffness, which can be expressed as:

$$K_g = (\frac{\partial J_\theta^T}{\partial \theta})F_{end} = [(\frac{\partial J_{\theta_1}^T}{\partial \theta_1})F_{end}(\frac{\partial J_{\theta_2}^T}{\partial \theta_2})F_{end}...(\frac{\partial J_\theta^T}{\partial \theta_n})F_{end}] \tag{5.4}$$

5.4.2 Transformation of Joint and Tendon Stiffness

The joint stiffness in each finger is formed of the passive parallel stiffness (K_{ppc}) and tendon stiffness (K_t):

$$K_\theta = K_{ppc} + K_t \tag{5.5}$$

Considering the K_{ppc} as a default in the mechanical system, the stiffness due to the tendon driven systems has the formula (McIntyre et al., 1996):

$$K_t = R^T k_t R + \frac{\partial R^T}{\partial \theta} F_t \tag{5.6}$$

where k_t is the tendon stiffness controlled by the motor command and feedback from the SEA sensors (Fig. 5.14). The second term in Eq. 5.6 presents the effect of configuration-dependent moment arm (R) and tendon force (F_t). Since the moment arms have constant values in the design, the changes in moment arms with respect to the changes in joint angles becomes zeros, and the second term goes to zero.

5.4.3 Tendon Stiffness Estimation

Following the deduction from the previous section, the tendon stiffness can be represented as the tendon force (F_t) with respect to the change of the tendon length (δl_t):

$$k_t = \frac{F_t}{\delta l_t} \tag{5.7}$$

where, the tendon force can be derived from the SEA force estimation (Fig. 5.14), which is the multiplication of spring stiffness (k_s) and spring displacement (δl_s) converted to the differential angles and radii of the pulleys ($F_t = k_s \delta l_s = k_s R_p \delta \theta_p$). The change in tendon length can be derived from the angle change of the first pulley and its radius ($\delta l_t = R_p \delta \theta_{p1}$). The $\delta \theta_{p1}$ can be also expressed as a summation of the angle differences between two pulleys and motor angle change:

$$\delta \theta_{p1} \quad = \quad \delta \theta_p + \delta \theta_m \tag{5.8}$$

This leads to the tendon stiffness as:

$$k_t = \frac{k_s \delta \theta_p}{\delta \theta_p + \delta \theta_m} = \frac{k_s}{1 + \delta \theta_m / \delta \theta_p} \tag{5.9}$$

The tendon stiffness in the system not only depends on the spring stiffness but also depends on the angle changes in SEA pulleys and the motor. The following section demonstrates an investigation of changes of Cartesian stiffness and ellipse due to changes of finger configurations and external loads.

5.4.4 Cartesian Stiffness Estimation

We have derived the complete mapping from the tendon to Cartesian space (Eq. 5.2 to Eq. 5.6). Adopting the kinematics and configuration of the single PPC finger and spring stiffness ($k_s = 0.296$ N/mm), we investigated the stiffness ellipses in the Cartesian space under certain conditions. We kept the tendon stiffness the same with spring stiffness, and we computed the Cartesian stiffness at three finger configurations. We also applied a external load to investigate the changes of the stiffness. Fig. 5.17 shows the stiffness differences between with and without PPC. At these three configurations, the PPC contributed to the Cartesian stiffness in the major directions,

and the stiffness ellipse is larger than the one without PPC. This implies that the PPC improved the Cartesian stiffness in the certain directions, and it also depends on the tendon stiffness and applied force direction. There was a slight distortion of stiffness ellipse with PPC, but it was not very significant.

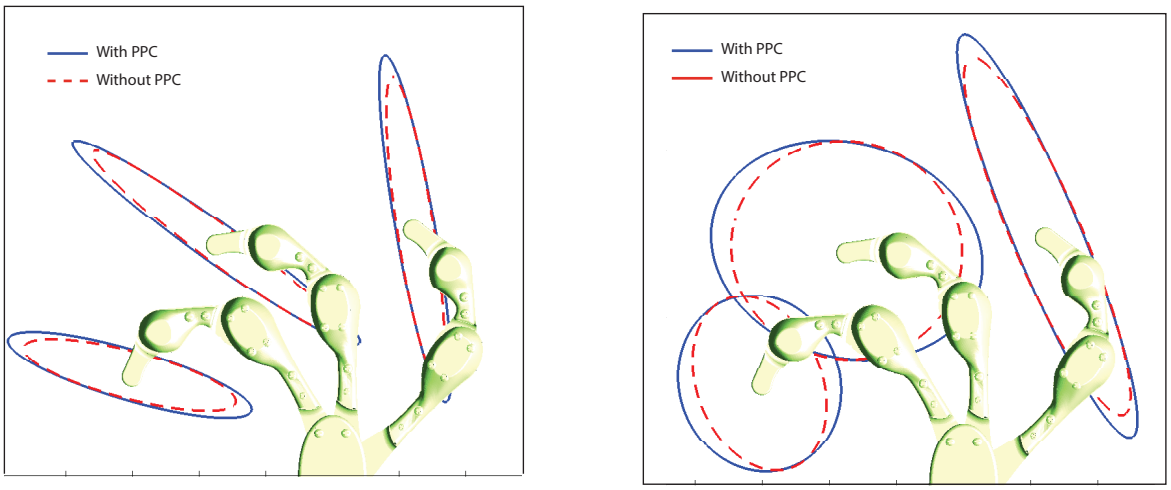

(a) Stiffness ellipse without external loads

(b) Stiffness ellipse with external loads 1.5 N

Figure 5.17: Stiffness analysis for the PPC manipulator. We choose three postures (MCP=$[-45°, 0°, 30°]$, PIP=$[45°, 45°, 45°]$) to investigate the contribution of PPC to the Cartesian stiffness with and without disturbance. The external force is applied for 1.5N at the horizontal direction at the finger tip.

5.4.5 Force Tracking Response

We aim to control the Cartesian stiffness through the low-level force control with SEA. Fig. 5.18 shows a force tracking response through a grasping task. We set a desired force $F_{des} = [3, 3, 1]$ N for the extensor, flexor, and cross-over, respectively. The manipulator was preset to an

initial position before the grasp. A object with a square shape was placed at the middle between the finger tip. There is no sensing feedback for the position or orientation of the object. The manipulator started to grasp the object and to maintain the static status. We applied disturbances at the X and Y direction (Fig. 5.15) along the center of grasping object with unknown force. We set the desired pulling force for two pairs of extensors and flexors to be 3 N. The results showed a great performance with respect to the disturbances (Fig 5.18). During the disturbance, the manipulator did not loose the contact with the object through the whole disturbing time.

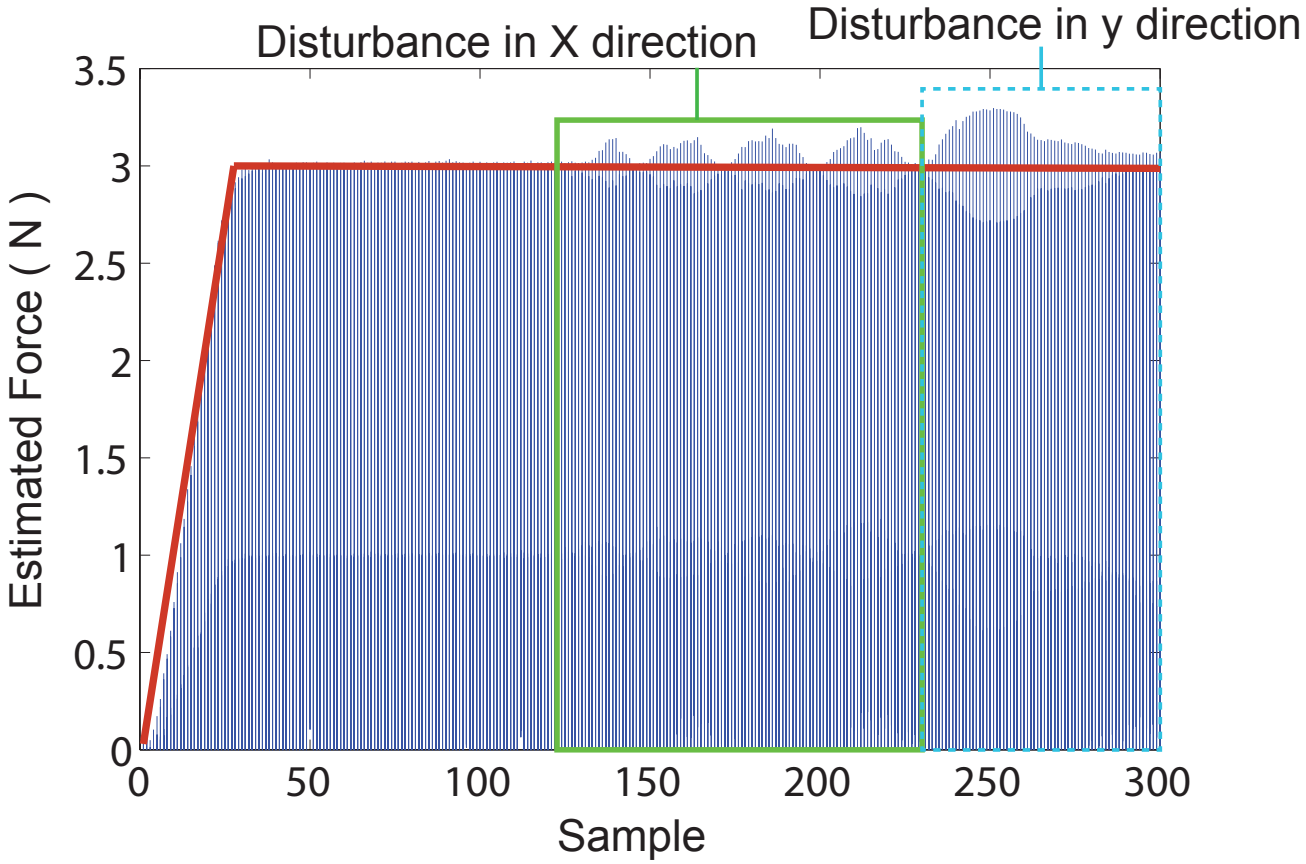

Figure 5.18: The force response due to the disturbance at the X and Y direction. The red color line present a ramp desired force in the grasping task. We applied the disturbace roughly along the cneter of grapsing object.

5.5 Discussion

5.5.1 PPC Finger Design

The design shows a great versatility at the test of manipulation. Most of finger-like robotic manipulator can only execute the grasping motions because of their limited actuation. Our design is based on the $N+1$ robotic finger, which is fully actuated system. As inspired from the kinematic

dependency at the PIP and DIP joint of human hands, we take advantage of a coupling mechanism in the design to achieve a human-like grasping motion with a minimal actuation. The manipulator perform a great deal of precision without any feedback. Open-loop position control allow us to accomplish difficult tasks that most of complicated robotic hands can hardly achieve such as screw and unscrew motion.

The design is extremely compact and light weight (less than 30 gram). The design not only implement the nonlinear compliance joint for each joint but also embed three tendons routed inside the finger. The trick that we have developed to improve the assembly quality decreased the complexity of hardware design and accelerate the manufacturing time. Having the capabilities to manipulate the additive manufacturing process allows us to modify the parts from multiple pieces into one. The manipulator system is low cost. The overall expense of the system which includes six servo motors is extremely low compared with the other existing commercial robotic or prosthetic hands.

5.5.2 SEA Design

As we presented previously, the results of force responses for the step, sinusoidal, and chirp input showed a great tracking capability in SEA. The manipulator can be operated within the bandwidth 1.6 Hz, which is enough for our application. The manipulator also performed a great stability to track the desired forces during the grasping test. The system can quickly respond to the disturbances in different directions.

5.5.3 Compliance and Grasping Stability

The design exhibits great compliance in the grasping tasks. The robot easily adapts any impact and disturbance at various configurations. The joint and tendon compliance compensates the external force and still guarantee the stable grasp for objects. In this study, we modeled the Cartesian stiffness to investigate the effect of nonlinear parallel compliance. The parallel compliance increases the coverage of grasping stiffness which can be observed from the increased areas of stiffness ellipse with PPC. It implies that the PPC could keep the grasping away from instability. For instance, if the grasping stiffness is close to a singular condition, meaning that the stiffness matrix is close to a ill-condition matrix, the grasp then tends to be unstable. Mathematically speaking, either one of two eigenvalues is extremely close to zero, the passive nonlinear compliance will keep the grasping stable since the three joint compliance in our design, as a default in the mechanical system, is formed on the diagonal of the matrix, and they are always positive definite with the configuration-dependent stiffness. This guarantees that even the tendons do not provide appropriate stiffness to the joint and Cartesian space, or the grasping stiffness is extremely stiff, the system can be stabilized depending on the stiffness of the PPC and the robot configuration.

5.6 Conclusion

We have developed a new compliant manipulator, and have carried out a series of validations for each subsystem. We first tested the basic control capability of the manipulator without the SEA by using the open control for the trajectory tracking. We then implemented the SEA so that a low-level of force control can be realized. All the validations shows that the system performs satisfactorily for the open-loop position control and force control. is well designed and is ready for the further tests and applications. The stiffness analysis showed that the presence of PPC improved

the grasping stiffness such that the lower tendon stiffness and hence lower efforts and energy are required to maintain the same stiffness in the Cartesian space. The future work involves carrying out further tests to investigate the effects of passive compliance in manipulation.

Chapter 6

Conclusions and Future Directions

We have used the knowledge gained from the understanding of the nonlinear joint compliance of human hands to design a novel compliant robotic finger. The biomechanical findings and the design concept developed from the framework for the biologically inspired robotic design. We have discovered the nonlinear joint stiffness and damping of the MCP joint at the index finger (Chapter 2 and 3). Inspired by the finding of passive parallel compliance in human hands, we created nonlinear compliant materials to implement passive compliance into a miniaturized robotic joint. Through the validation, the miniaturized joint design exhibits a human-like joint compliance (Chapter 4). A successful new robotic manipulator is finally developed through careful design, and fast prototyping (Chapter 5). There are three major contributions to the biomechanical and robotic areas:

6.1 Model of MCP Joint compliance

We have derived models of the nonlinear joint stiffness of the human hand joints through human experiments and subject-specific modeling. We further determined the relative contributions of muscle-tendon units and capsule-ligament complex. We showed that the parallel compliance is dominant on the passive joint stiffness for a wide range of joint motion, and that it provides a configuration-dependent stiffness to stabilize the limb movements. The insight is useful for biomechanical, clinical, and robotic areas of research.

6.2 Model of MCP Joint Damping

We have developed nonlinear damping models that describe damping property of the MCP joint. We showed that the nonlinear viscous damping depends on the cyclic frequency, and that fluid-like and structural damping also contribute to the energy dissipation of the MCP joint. The new damping model provides an ability to describe a subject-specific damping behavior, and also remain a generality for common behavior through the model reduction process. Biomechanists may adopt more detailed damping models for subject-specific simulation or modeling. The simplified model can be used to implement human-like damping in impedance control or a design of new mechanical damper for robotic hands.

6.3 Novel Designs

6.3.1 Miniaturized Joint Design

Inspired by the unique parallel joint compliance, we developed a novel variable joint mechanism that mimics the human-like passive compliance. Two tuneable mechanisms are designed to adjust joint torque profile. The overall dimension is less than 30 millimeters, and the design exhibits human-like joint compliance. The compact and light weight joint design with custom-made elastic materials allows us to implement the rotary design into robotic hands.

6.3.2 Human-like Manipulator

The design can be used to apply on patient specific prosthetic hands or fingers design. This is one of the reasons we keep the design flexible in such ways that size can be scaled by adopting different materials for different stiffness profiles. The geometry of the joint design is simple, and the framework of computation is straightforward. Instead of using the other expensive manufacturing

process, using the addictive printing technique (plastic extrusion type) accelerate the fabricating time for emerging or low cost purposes.

6.3.3 Finger Testing Mechanism

We have developed one motor-driven mechanism that integrated with EMGs and motion capture system for the human data collection. The challenges of designing this system is to design a environment for different participants to proceed the experiments. The device can be potentially modified for other type of testing and for use as a therapy device.

6.4 Limitations

There are several limitations of the presented work. The most relevant limitation in our biomechanical studies is that we cannot control the patient's muscle activity except EMGs measurement. Effect of stretch reflex could have influences on the data collection during the experiment. However, targeting the EMGs signals for the major muscles passing through the index finger is fairly robust to detect the activity of muscle active contraction or stretch reflex. We discarded the data set whose EMG signals were over the threshold.

For the robotic manipulator, there is no position or force feedback at the joint or Cartesian space so the finger configuration is unknown during controls. The position information is based on the model prediction. Without implementing the SEA, the open-loop position control performed excellently. The SEA angle sensing is prone to error, so it is difficult to gain information of finger kinematics. However, controlling the position is not the main purpose of implementing SEA which are designed for force control.

6.5 Future Works

6.5.1 Implementation of Nonlinear Damping

To date none of the robotic hands possesses human-like damping behavior. The reason is that there is no model available for implementation through control and design of mechanical element in robotic hands. Implementing the nonlinear viscous damping developed in this thesis is a good way to achieve the human-like damping performance. A benefit of adopting the impedance control is that we can avoid adding more mechanical elements into a very limited space in the robotic hands.

6.5.2 Compact Design of SEA

The SEA actuation can be more compact for the real applications. Each SEA has two potentiometers connecting with linear spring, and it occupies large space for the spring to stretch. For the future implementation, we can develop a rotational SEA to reduce the size and space of the SEA.

6.5.3 Development of Robotic Hand

Most of difficult stage for the whole design is to initialize the model. Since we have accomplished and demonstrated the finger design, a novel robotic hand with human-like compliance can be realized by designing the five fingers. We have setup the framework for modeling, computation, and manufacturing of human-like joint properties in robotic hands. A fast prototyping will accelerate the manufacturing time once the design is finalized.

Bibliography

M. E. Abdallah, R. Platt, and C. W. Wampler. Decoupled torque control of tendon-driven fingers with tension management. *The International Journal of Robotics Research*, 32(2):247–258, 2013.

D. Accoto, N. L. Tagliamonte, G. Carpino, F. Sergi, M. Di Palo, and E. Guglielmelli. pvej: A modular passive viscoelastic joint for assistive wearable robots. In *IEEE International Conference on Robotics and Automation*, pages 3361–3366. IEEE, 2012.

A. Albu-Schaffer, O. Eiberger, M. Grebenstein, S. Haddadin, C. Ott, T. Wimbock, S. Wolf, and G. Hirzinger. Soft robotics. *Robotics & Automation Magazine, IEEE*, 15(3):20–30, 2008.

K. Amankwah, R. J. Triolo, and R. Kirsch. Effects of spinal cord injury on lower-limb passive joint moments revealed through a nonlinear viscoelastic model. *Journal of Rehabilitation Research and Development*, 41(1):15–32, 2004.

K. An, Y. Ueba, E. Chao, W. Cooney, and R. Linscheid. Tendon excursion and moment arm of index finger muscles. *Journal of Biomechanics*, 16(6):419–425, 1983. ISSN 0021-9290.

K. An, E. Chao, W. Cooney, and R. Linscheid. Forces in the normal and abnormal hand. *Journal of Orthopaedic Research*, 3(2):202–211, 1985. ISSN 1554-527X.

A. Ananthanarayanan, M. Azadi, and S. Kim. Towards a bio-inspired leg design for high-speed running. *Bioinspiration & Biomimetics*, 7(4):046005, 2012.

N. Ashish, K. Rodrigo, and Z. Li. Finger joint motion generated by individual extrinsic muscles: A cadaveric study. *Journal of Orthopaedic Surgery and Research*, 3, 2008.

D. Beevers and B. Seedhom. A new concept for a metacarpophalangeal prosthesis: consequence on joint biomechanics. *Clinical Biomechanics*, 14(3):166–176, 1999.

N. Berme, J. Paul, and W. Purves. A biomechanical analysis of the metacarpo-phalangeal joint. *Journal of Biomechanics*, 10(7):409–412, 1977.

N. Berme, A. E. Engin, and K. M. C. da Silva. *Biomechanics of normal and pathological human articulating joints*. Number 93. Springer, 1985.

L. Biagiotti, P. Tiezzi, G. Vassura, and C. Melchiorri. *Modelling and Controlling the Compliance of a Robotic Hand with Soft Finger-pads*. Springer, 2005.

C. Bonifasi-Lista, S. P. Lakez, M. S. Small, and J. A. Weiss. Viscoelastic properties of the human medial collateral ligament under longitudinal, transverse and shear loading. *Journal of Orthopaedic Research*, 23(1):67–76, 2005.

J. Borràs and A. M. Dollar. Actuation torque reduction in parallel robots using joint compliance. *Journal of Mechanisms and Robotics*, 6(2):021006, 2014.

C. Borst, M. Fischer, S. Haidacher, H. Liu, and G. Hirzinger. Dlr hand ii: experiments and experience with an anthropomorphic hand. In *IEEE International Conference on Robotics and Automation*, volume 1, pages 702–707. IEEE, 2003.

P. Bose, R. Parmer, and F. J. Thompson. Velocity-dependent ankle torque in rats after contusion injury of the midthoracic spinal cord: time course. *Journal of Neurotrauma*, 19(10):1231–1249, 2002.

P. Brand and A. Hollister. *Clinical Mechanics of the Hand*. Mosby, 1999. ISBN 0815127863.

L. Bridgwater, C. Ihrke, M. Diftler, M. Abdallah, N. Radford, J. Rogers, S. Yayathi, R. Askew, and D. Linn. The robonaut 2 hand-designed to do work with tools. In *IEEE International Conference on Robotics and Automation*, pages 3425–3430. IEEE, 2012.

T. Buchanan. Evidence that maximum muscle stress is not a constant: differences in specific tension in elbow flexors and extensors. *Medical engineering & physics*, 17(7):529–536, 1995. ISSN 1350-4533.

T. Buchanan, D. Lloyd, K. Manal, and T. Besier. Neuromusculoskeletal modeling: Estimation of muscle forces and joint moments and movements from measurements of neural command. *Journal of Applied Biomechanics*, 20(4):367, 2004.

F. Buchthal. *The rheology of the cross striated muscle fibre: with particular reference to isotonic conditions*, volume 21. I kommission hos Munksgaard, 1951.

J. Cadima and I. T. Jolliffe. Loading and correlations in the interpretation of principle compenents. *Journal of Applied Statistics*, 22(2):203–214, 1995.

B. Calvo, A. Ramírez, A. Alonso, J. Grasa, F. Soteras, R. Osta, and M. Muñoz. Passive nonlinear elastic behaviour of skeletal muscle: Experimental results and model formulation. *Journal of Biomechanics*, 2009.

M. Cammarata and Y. Dhaher. The differential effects of gender, anthropometry, and prior hormonal state on frontal plane knee joint stiffness. *Clinical Biomechanics*, 23(7):937–945, 2008.

K. Campbell and M. Lakie. A cross-bridge mechanism can explain the thixotropic short-range elastic component of relaxed frog skeletal muscle. *The Journal of Ppino hysiology*, 510(3):941–962, 2004.

G. Carpino, D. Accoto, M. Di Palo, N. Tagliamonte, F. Sergi, and E. Guglielmelli. Design of a rotary passive viscoelastic joint for wearable robots. pages 1–6, 2011.

J. Carr, R. Beatson, J. Cherrie, T. Mitchell, W. Fright, B. McCallum, and T. Evans. Reconstruction and representation of 3D objects with radial basis functions. In *Proceedings of the 28th annual conference on Computer graphics and interactive techniques*, pages 67–76. ACM, 2001. ISBN 158113374X.

J. Carr, R. Beatson, B. McCallum, W. Fright, T. McLennan, and T. Mitchell. Smooth surface reconstruction from noisy range data. *ACM GRAPHITE*, 3:119–126, 2003.

M. Carrozza, C. Suppo, F. Sebastiani, B. Massa, F. Vecchi, R. Lazzarini, M. Cutkosky, and P. Dario. The spring hand: development of a self-adaptive prosthesis for restoring natural grasping. *Autonomous Robots*, 16(2):125–141, 2004.

E. Cavallaro, J. Rosen, J. Perry, S. Burns, and B. Hannaford. Hill-based model as a myoprocessor for a neural controlled powered exoskeleton arm-parameters optimization. In *IEEE International Conference on Robotics and Automation*, volume 4, page 4514. IEEE; 1999, 2005.

P. Cerveri, N. Lopomo, A. Pedotti, and G. Ferrigno. Derivation of centers and axes of rotation for wrist and fingers in a hand kinematic model: Methods and reliability results. *Annals of Biomedical Engineering*, 33(3):402–412, 2005.

P. Cerveri, E. De Momi, N. Lopomo, G. Baud-Bovy, R. Barros, and G. Ferrigno. Finger kinematic modeling and real-time hand motion estimation. *Annals of Biomedical Engineering*, 35(11):1989–2002, 2007.

D. Chaffin, G. Andersson, B. Martin, et al. *Occupational biomechanics*. Wiley New York, 2006. ISBN 0471601349.

S.-F. Chen and I. Kao. Conservative congruence transformation for joint and cartesian stiffness matrices of robotic hands and fingers. *The International Journal of Robotics Research*, 19(9): 835–847, 2000.

Y. Chen, C. Bauer, O. Burmeister, R. Rupp, and R. Mikut. First Steps to Future Applications of Spinal Neural Circuit Models in Neuroprostheses and Humanoid Robots. In *Proc*, volume 17, pages 186–199, 2007.

Y. Cheng, J. Hootman, L. Murphy, G. Langmaid, and C. Helmick. Prevalence of doctor-diagnosed arthritis and arthritis-attributable activity limitation-united states, 2007–2009. *MMWR Morb Mortal Wkly Rep*, 59(39):1261–1265, 2010.

M. R. Cutkosky and I. Kao. Computing and controlling compliance of a robotic hand. *Robotics and Automation, IEEE Transactions on*, 5(2):151–165, 1989.

M. R. Cutkosky and S. Kim. Design and fabrication of multi-material structures for bioinspired robots. *Philosophical Transactions of the Royal Society A: Mathematical, Physical and Engineering Sciences*, 367(1894):1799–1813, 2009.

F. Danion, S. Li, V. Zatsiorsky, and M. Latash. Relations between surface emg of extrinsic flexors and individual finger forces support the notion of muscle compartments. *European journal of applied physiology*, 88(1):185–188, 2002.

C. W. De Silva. *Vibration damping, control, and design*. CRC Press, 2007.

S. Delp. *Surgery simulation: a computer graphics system to analyze and design musculoskeletal reconstructions of the Lower Limb*. PhD thesis, Stanford University, CA, 1990.

S. Delp, A. Grierson, and T. Buchanan. Maximumisometric moments generated by the wrist muscles in flexion-extension and radial-ulnar deviation. *Journal of Biomechanics*, 29(10):1371–1375, 1996. ISSN 0021-9290.

S. Delp, F. Anderson, A. Arnold, P. Loan, A. Habib, C. John, E. Guendelman, and D. Thelen. Opensim: open-source software to create and analyze dynamic simulations of movement. *Biomedical Engineering, IEEE Transactions on*, 54(11):1940–1950, 2007.

J. Dennerlein. Finger flexor tendon forces are a complex function of finger joint motions and fingertip forces. *Journal of Hand Therapy*, 18(2):120–127, 2005.

J. Dennerlein, E. Diao, C. Mote Jr, and D. Rempel. In vivo finger flexor tendon force while tapping on a keyswitch. *Journal of Orthopaedic Research*, 17(2):178–184, 1999.

A. Deshpande, R. Balasubramanian, R. Lin, B. Dellon, and Y. Matsuoka. Understanding variable moment arms for the index finger MCP joints through the ACT hand. In *2nd IEEE RAS amd EMBS International Conference on Biomedical Robotics and Biomechatronics*, pages 776–782, 2008.

A. Deshpande, J. Ko, D. Fox, and Y. Matsuoka. Anatomically correct testbed hand control: Muscle and joint control strategies. In *IEEE International Conference on Robotics and Automation*, pages 4416–4422. IEEE, 2009.

A. Deshpande, R. Balasubramanian, J. Ko, and Y. Matsuoka. Acquiring variable moment arms for index finger using a robotic testbed. *IEEE Transactions on Biomedical Engineering*, 57(8): 2034–2044, 2010.

A. D. Deshpande, N. Gialis, and Y. Matsuoka. Contributions of the visco-elastic forces during the index finger and wrist movements. *in print Transactions on Biomedical Engineering*, 59:586–594, 2012.

A. D. Deshpande, J. Ko, D. Fox, and Y. Matsuoka. Control strategies for the index finger of a tendon-driven hand. *The International Journal of Robotics Research*, 32:115–128, 2013a.

A. D. Deshpande, Z. Xu, M. V. Weghe, B. H. Brown, J. Ko, L. Y. Chang, D. D. Wilkinson, S. M. Bidic, and Y. Matsuoka. Mechanisms of the anatomically correct testbed hand. *IEEE/ASME Transactions on Mechatronics*, 18(1):238–250, 2013b.

M. Diftler, J. Mehling, M. Abdallah, N. Radford, L. Bridgwater, A. Sanders, R. Askew, D. Linn, J. Yamokoski, F. Permenter, et al. Robonaut 2-the first humanoid robot in space. In *IEEE International Conference on Robotics and Automation*, pages 2178–2183. IEEE, 2011.

M. Diftler, T. Ahlstrom, R. Ambrose, N. Radford, C. Joyce, N. De La Pena, A. Parsons, and A. Noblitt. Robonaut 2–initial activities on-board the iss. In *Proceedings of the IEEE Aerospace Conference, Big Sky, Montana*, 2012.

A. Dollar, L. Jentoft, J. Gao, and R. Howe. Contact sensing and grasping performance of compliant hands. *Autonomous Robots*, 28(1):1–11, January 2010.

A. M. Dollar and R. D. Howe. Simple, robust autonomous grasping in unstructured environments. In *Robotics and Automation, 2007 IEEE International Conference on*, pages 4693–4700. IEEE, 2007.

M. Domalain, L. Vigouroux, F. Danion, V. Sevrez, and E. Berton. Effect of object width on precision grip force and finger posture. *Ergonomics*, 51(9):1441–1453, 2008.

S. Duenwald, R. Vanderby, and R. Lakes. Constitutive equations for ligament and other soft tissue: evaluation by experiment. *Acta mechanica*, 205(1):23–33, 2009a.

S. Duenwald, R. Vanderby, and R. Lakes. Viscoelastic relaxation and recovery of tendon. *Annals of Biomedical Engineering*, 37(6):1131–1140, 2009b.

S. Duenwald, R. Vanderby, and R. Lakes. Stress relaxation and recovery in tendon and ligament: Experiment and modeling. *Biorheology*, 47(1):1–14, 2010.

O. Eiberger, S. Haddadin, M. Weis, A. Albu-Schaffer, and G. Hirzinger. On joint design with intrinsic variable compliance: Derivation of the dlr qa-joint. In *IEEE International Conference on Robotics and Automation*, pages 1687–1694. IEEE, 2010.

B. Elhassan, D. Mcneal, S. Wynn, M. Gonzalez, and F. Amirouch. Experimental investigation of finger dynamics before and after metacarpophalangeal joint arthroplasty. *The Journal of Hand Surgery*, 31(2):228–235, 2006.

A. Engin. On the damping properties of the shoulder complex. *Journal of Biomechanical Engineering*, 106(4):360–363, 1984.

C. English and D. Russell. Implementation of variable joint stiffness through antagonistic actuation using rolamite springs. *Mechanism and Machine Theory*, 34(1):27–40, 1999.

A. Esteki and J. Mansour. An experimentally based nonlinear viscoelastic model of joint passive moment. *Journal of Biomechanics*, 29(4):443–450, 1996.

A. Esteki and J. Mansour. A dynamic model of the hand with application in functional neuromuscular stimulation. *Annals of Biomedical Engineering*, 25(3):440–451, 1997.

H. Fang, M. Rais-Rohani, Z. Liu, and M. Horstemeyer. A comparative study of metamodeling methods for multiobjective crashworthiness optimization. *Computers and Structures*, 83(25-26): 2121–2136, 2005. ISSN 0045-7949.

W. N. Findley and F. Davis. *Creep and relaxation of nonlinear viscoelastic materials*. Courier Dover Publications, 2011.

K. Fok and S. Chou. Development of a finger biomechanical model and its considerations. *Journal of Biomechanics*, 43(4):701–713, 2010. ISSN 0021-9290.

N. Fowler and A. Nicol. Functional and biomechanical assessment of the normal and rheumatoid hand. *Clinical Biomechanics*, 16(8):660–666, 2001.

N. Fowler and A. Nicol. A biomechanical analysis of the rheumatoid index finger after joint arthroplasty. *Clinical Biomechanics*, 17(5):400–405, 2002.

R. Gajdosik. Passive extensibility of skeletal muscle: review of the literature with clinical implications. *Clinical Biomechanics*, 16(2):87–101, 2001.

R. Gay, B. Ilharreborde, K. Zhao, C. Zhao, and K. An. Sagittal plane motion in the human lumbar spine: comparison of the in vitro quasistatic neutral zone and dynamic motion parameters. *Clinical Biomechanics*, 21(9):914–919, 2006. ISSN 0268-0033.

N. Gialias and Y. Matsuoka. Muscle actuator design for the ACT Hand. In *IEEE International Conference on Robotics and Automation*, volume 4, pages 3380–3385. IEEE, 2004.

N. Gialias and Y. Matsuoka. A musculotendon contribution for multijoint hand control. In *Conference proceedings: Annual International Conference of the IEEE Engineering in Medicine and Biology Society.*, volume 1, page 4482, 2006.

C. Gielen and J. Houk. Nonlinear viscosity of human wrist. *Journal of Neurophysiology*, 52(3): 553–569, 1984.

J. P. Gleghorn and L. J. Bonassar. Lubrication mode analysis of articular cartilage using stribeck surfaces. *Journal of Biomechanics*, 41(9):1910–1918, 2008.

R. Gonzalez, T. Buchanan, and S. Delp. How muscle architecture and moment arms affect wrist flexion-extension moments. *Journal of Biomechanics*, 30(7):705–712, 1997.

A. González Rodríguez, J. Chacón, A. Donoso, and A. González Rodríguez. Design of an adjustable-stiffness spring: Mathematical modeling and simulation, fabrication and experimental validation. *Mechanism and Machine Theory*, 46(12):1970–1979, 2011.

D. Gouaillier, V. Hugel, P. Blazevic, C. Kilner, J. Monceaux, P. Lafourcade, B. Marnier, J. Serre, and B. Maisonnier. The nao humanoid: a combination of performance and affordability. *CoRR abs/0807.3223*, 2008.

E. Graesser and C. Wong. The relationship of traditional damping measures for materials with high damping capacity. Technical report, DTIC Document, 1991.

M. Grebenstein and P. van der Smagt. Antagonism for a highly anthropomorphic hand–arm system. *Advanced Robotics*, 22(1):39–55, 2008.

M. Grebenstein, M. Chalon, G. Hirzinger, and R. Siegwart. Antagonistically driven finger design for the anthropomorphic dlr hand arm system. In *International Conference on Humanoid Robots (Humanoids), 2010 10th IEEE-RAS*, pages 609–616. IEEE, 2010.

M. Grebenstein, A. Albu-Schaffer, T. Bahls, M. Chalon, O. Eiberger, W. Friedl, R. Gruber, S. Haddadin, U. Hagn, R. Haslinger, et al. The dlr hand arm system. In *IEEE International Conference on Robotics and Automation*, pages 3175–3182. IEEE, 2011.

T. Greiner. Hand anthropometry of us army personnel. Technical report, , 1991.

S. Haddadin, A. Schäffer, and G. Hirzinger. Safety evaluation of physical human-robot interaction via crash-testing. In *Robotics: Science and Systems Conference (RSS2007)*, pages 217–224, 2007.

A. Z. Hajian and R. D. Howe. Identification of the mechanical impedance at the human finger tip. *Journal of Biomechanical Engineering*, 119(1):109–114, 1997.

M. Halaki, N. ODwyer, and I. Cathers. Systematic nonlinear relations between displacement amplitude and joint mechanics at the human wrist. *Journal of Biomechanics*, 39(12):2171–2182, 2006.

K. Halvorsen, M. Lesser, and A. Lundberg. A new method for estimating the axis of rotation and the center of rotation. *Journal of Biomechanics*, 32(11):1221–1227, 1999. ISSN 0021-9290.

R. v. Ham, T. Sugar, B. Vanderborght, K. Hollander, and D. Lefeber. Compliant actuator designs. *Robotics and Automation Magazine, IEEE*, 16(3):81–94, 2009.

R. Hardy. Multiquadric equations of topography and other irregular surfaces. *Journal of Geophysical Research*, 76(8):1905–1915, 1971. ISSN 0148-0227.

H. Hatze. A new method for the simultaneous measurement of the moment of inertia, the damping coefficient and the location of the centre of mass of a body segmentin situ. *European journal of applied physiology and occupational physiology*, 34(1):217–226, 1975.

K. Hayes and H. Hatze. Passive visco-elastic properties of the structures spanning the human elbow joint. *European Journal of Applied Physiology and Occupational Physiology*, 37(4):265–274, 1977. ISSN 0301-5548.

H. Heger, V. Wank, and R. Blickhan. A quasi-linear viscoelastic model for the passive properties of the human hip joint. *Journal of Mechanics in Medicine and Biology*, 12(01), 2012.

S. Heitmann, N. Ferns, and M. Breakspear. Muscle co-contraction modulates damping and joint stability in a three-link biomechanical limb. *Frontiers in neurorobotics*, 5:5–5, 2010.

T. Herda, N. Herda, P. Costa, A. Walter-Herda, A. Valdez, and J. Cramer. The effects of dynamic stretching on the passive properties of the muscle-tendon unit. 2012.

A. Herrmann and S. Delp. Moment arm and force-generating capacity of the extensor carpi ulnaris after transfer to the extensor carpi radialis brevis. *The Journal of Hand Surgery*, 24(5):1083–1090, 1999. ISSN 0363-5023.

T. Hochkirchen. Modern multivariate statistical techniques: Regression, classification, and manifold learning. *Journal of the Royal Statistical Society: Series A (Statistics in Society)*, 173(2):467–467, 2010.

K. Holzbaur, W. Murray, and S. Delp. A model of the upper extremity for simulating musculoskeletal surgery and analyzing neuromuscular control. *Annals of Biomedical Engineering*, 33(6):829–840, 2005. ISSN 0090-6964.

T. Hsieh, J. Tsai, Y. Wu, I. Hwang, T. Chen, and J. Chen. Time course quantification of spastic hypertonia following spinal hemisection in rats. *Neuroscience*, 167(1):185–198, 2010.

X. Hu, W. M. Murray, and E. J. Perreault. Muscle short-range stiffness can be used to estimate the endpoint stiffness of the human arm. *Journal of Neurophysiology*, 105(4):1633–1641, 2011.

T.-H. Huang, J.-Y. Kuan, and H.-P. Huang. Design of a new variable stiffness actuator and application for assistive exercise control. In *Intelligent Robots and Systems (IROS), 2011 IEEE/RSJ International Conference on*, pages 372–377. IEEE, 2011.

R. Hubbard, K. Chun, et al. Mechanical responses of tendons to repeated extensions and wait periods. *Journal of Biomechanical Engineering*, 110(1):11, 1988.

D. Hunter and J. Spriggs. Investigation into the relationship between the passive flexibility and active stiffness of the ankle plantar-flexor muscles. *Clinical Biomechanics*, 15(8):600–606, 2000.

J. N. Ingram, K. P. Körding, I. S. Howard, and D. M. Wolpert. The statistics of natural hand movements. *Experimental Brain Research*, 188(2):223–236, 2008.

M. Jacobson, R. Raab, B. Fazeli, R. Abrams, M. Botte, and R. Lieber. Architectural design of the human intrinsic hand muscles. *The Journal of Hand Surgery*, 17(5):804–809, 1992.

A. Jafari, N. Tsagarakis, I. Sardellitti, and D. Caldwell. How design can affect the energy required to regulate the stiffness in variable stiffness actuators. In *IEEE International Conference on Robotics and Automation*, pages 2792–2797. IEEE, 2012.

I. Jolliffe. *Principal Component Analysis*. Wiley Online Library, 2005.

S. Kajikawa. Development of a robot hand with an adjuster mechanism for joint compliance. In *Proceedings of the 2008 IEEE International Conference on Robotics and Biomimetics*, pages 1683–1688. IEEE, 2009.

D. Kamper, T. George Hornby, and W. Rymer. Extrinsic flexor muscles generate concurrent flexion of all three finger joints. *Journal of Biomechanics*, 35(12):1581–1589, 2002.

D. Kamper, H. Fischer, and E. Cruz. Impact of finger posture on mapping from muscle activation to joint torque. *Clinical Biomechanics*, 21(4):361–369, 2006.

E. Kandel, J. Schwartz, and T. Jessell. *Principles of Neural Science*. McGraw-Hill/Appleton & Lange, 2000.

I. Kao and F. Yang. Stiffness and contact mechanics for soft fingers in grasping and manipulation. *Robotics and Automation, IEEE Transactions on*, 20(1):132–135, 2004.

I. Kao, M. R. Cutkosky, and R. S. Johansson. Robotic stiffness control and calibration as applied to human grasping tasks. *Robotics and Automation, IEEE Transactions on*, 13(4):557–566, 1997.

A. Kargov, O. Ivlev, C. Pylatiuk, T. Asfour, S. Schulz, A. Gräser, R. Dillmann, and G. Bretthauer. Applications of a fluidic artificial hand in the field of rehabilitation. *Rehabilitation Robotics Wien: I-Tech Education and Publ*, pages 261–86, 2007.

P. Keir, R. Wells, and D. Ranney. Passive properties of the forearm musculature with reference to hand and finger postures. *Clinical Biomechanics*, 11(7):401–409, 1996.

L. Ketchum and D. Thompson. An experimental investigation into the forces internal to the human hand. *Clinical mechanics of the hand, St. Louis, Mosby Year Book*, 275, 1992.

B. Kim and A. Deshpande. Design of nonlinear rotational stiffness using a non-circular pulley-spring mechanism. *Journal of Mechanisms Robotics*, 2014.

S. Kim, J. E. Clark, and M. R. Cutkosky. isprawl: Design and tuning for high-speed autonomous open-loop running. *The International Journal of Robotics Research*, 25(9):903–912, 2006.

S. Kim, M. Spenko, S. Trujillo, B. Heyneman, D. Santos, and M. R. Cutkosky. Smooth vertical surface climbing with directional adhesion. *Robotics, IEEE Transactions on*, 24(1):65–74, 2008.

J. S. Knutson, K. L. Kilgore, J. M. Mansour, and P. E. Crago. Intrinsic and extrinsic contributions to the passive moment at the metacarpophalangeal joint. *Journal of Biomechanics*, 33:1675–1681, 2000.

A. Kociolek and P. Keir. Modelling tendon excursions and moment arms of the finger flexors: Anatomic fidelity versus function. *Journal of Biomechanics*, 44(10):1967–1973, 2011.

J. R. Koza. *Genetic programming: on the programming of computers by means of natural selection*, volume 1. MIT press, 1992.

R. K. Kramer, C. Majidi, and R. J. Wood. Wearable tactile keypad with stretchable artificial skin. In *IEEE International Conference on Robotics and Automation*, pages 1103–1107. IEEE, 2011.

P. H. Kuo and A. Deshpande. Contribution of passive properties of muscle-tendon units to the metacarpophalangeal joint torque of the index finger. In *Proceedings of the International Conference on Biomedical Robotics and Biomechatronics*, 2010.

P.-H. Kuo and A. D. Deshpande. Muscle-tendon units provide limited contributions to the passive stiffness of the index finger metacarpophalangeal joint. *Journal of Biomechanics*, 2012.

P.-H. Kuo and A. D. Deshpande. Novel design of a passive variable stiffness joint mechanism: Inspiration from biomechanics of hand joints. In *ASME Dynamic Systems and Control Conference*, 2013.

P.-H. Kuo, J. Hayes, and A. Deshpande. Design of a motor-driven mechanism to conduct experiments to determine the passive joint properties of the human index finger. In *Proceedings of the ASME International Design Engineering Technical Conference & Computers and Information in Engineering Conference*, 2011.

P.-H. Kuo, J. Hayes, and A. D. Deshpande. Design and performance of a motor-driven mechanism to conduct experiments with the human index finger. *Journal of Mechanisms and Robotics*, 7(3): 031010, 2015.

M. U. Kurse, H. Lipson, and F. J. Valero-Cuevas. Extrapolatable analytical functions for tendon excursions and moment arms from sparse datasets. *Biomedical Engineering, IEEE Transactions on*, 59(6):1572–1582, 2012.

M. Laffranchi, N. Tsagarakis, and D. Caldwell. A compact compliant actuator (compact) with variable physical damping. pages 4644–4650, 2011.

R. Lakes. Viscoelastic materials. *Cambridge University Press*, 2009.

M. Lakie and L. Robson. Thixotropic changes in human muscle stiffness and the effects of fatigue. *Experimental Physiology*, 73(4):487–500, 1988.

A. D. Lantada and P. L. Morgado. Rapid prototyping for biomedical engineering: current capabilities and challenges. *Annual Review of Biomedical Engineering*, 14:73–96, 2012.

M. Latash and V. Zatsiorsky. Joint stiffness: Myth or reality? *Human movement science*, 12(6): 653–692, 1993.

M. K. Lebiedowska and R. J. Fisk. Passive dynamics of the knee joint in healthy children and children affected by spastic paresis. *Clinical Biomechanics*, 14:653–660, November 1999.

H.-M. Lee, J.-J. J. Chen, M.-S. Ju, C.-C. K. Lin, and P. P. Poon. Validation of portable muscle tone measurement device for quantifying velocity-dependent properties in elbow spasticity. *Journal of Electromyography and Kinesiology*, 14(5):577–589, 2004.

H.-M. Lee, J.-J. J. Chen, Y.-N. Wu, Y.-L. Wang, S.-C. Huang, and M. Piotrkiewicz. Time course analysis of the effects of botulinum toxin type a on elbow spasticity based on biomechanic and electromyographic parameters. *Archives of Physical Medicine and Rehabilitation*, 89(4):692–699, 2008.

J. Leijnse, S. Carter, A. Gupta, and S. Mccabe. Anatomic basis for individuated surface emg and homogeneous electrostimulation with neuroprostheses of the extensor digitorum communis. *Journal of Neurophysiology*, 100(1):64–75, 2008a.

J. N. Leijnse, N. H. Campbell-Kyureghyan, D. Spektor, and P. M. Quesada. Assessment of individual finger muscle activity in the extensor digitorum communis by surface emg. *Journal of Neurophysiology*, 100(6):3225–3235, 2008b.

R. Lieber, B. Fazeli, and M. Botte. Architecture of selected wrist flexor and extensor muscles. *The Journal of Hand Surgery*, 15(2):244–250, 1990. ISSN 0363-5023.

R. Lieber, M. Jacobson, B. Fazeli, R. Abrams, and M. Botte. Architecture of selected muscles of the arm and forearm: anatomy and implications for tendon transfer. *The Journal of Hand Surgery*, 17(5):787–798, 1992.

D. Lin and W. Rymer. Damping actions of the neuromuscular system with inertial loads: human flexor pollicis longus muscle. *Journal of Neurophysiology*, 85(3):1059, 2001.

C. Long et al. Intrinsic-extrinsic muscle control of the fingers: Electromyographic studies. *The Journal of Bone and Joint Surgery*, 50(5):973, 1968.

F. Lotti, P. Tiezzi, G. Vassura, L. Biagiotti, G. Palli, and C. Melchiorri. Development of ub hand 3: Early results. In *IEEE International Conference on Robotics and Automation*, pages 4488–4493. IEEE, 2005.

C. Lovchik and M. Diftler. The robonaut hand: A dexterous robot hand for space. In *IEEE International Conference on Robotics and Automation*, volume 2, pages 907–912. IEEE, 1999.

W. MacKay, D. Crammond, H. Kwan, and J. Murphy. Measurements of human forearm viscoelasticity. *Journal of Biomechanics*, 19(3):231–238, 1986.

M. A. Maier and M.-C. Hepp-Reymond. Emg activation patterns during force production in precision grip. *Experimental Brain Research*, 103(1):108–122, 1995.

M. Malhotra and Y. Matsuoka. The Relationship between Actuator Reduction and Controllability for a Robotic Hand. In *International Conference on Biomedical Robotics and Biomechatronics*, 2010.

K. Manal and T. Buchanan. Subject-specific estimates of tendon slack length: A numerical method. *Journal of Applied Biomechanics*, 20(2):195–203, 2004. ISSN 1065-8483.

H. G. Marques, M. Jantsch, S. Wittmeier, O. Holland, C. Alessandro, A. Diamond, M. Lungarella, and R. Knight. Ecce1: the first of a series of anthropomimetic musculoskeletal upper torsos. In *Humanoid Robots (Humanoids), 2010 10th IEEE-RAS International Conference on*, pages 391–396. IEEE, 2010.

Y. Matsuoka and P. Afshar. Neuromuscular strategies for dynamic finger movements: a robotic approach. In *Proc IEEE Engineering in Medicine and Biology Society*, volume 2, pages 4639–4642, 2004.

W. Maurel, D. Thalmann, P. Hoffmeyer, P. Beylot, P. Gingins, P. Kalra, and N. Thalmann. A biomechanical musculoskeletal model of human upper limb for dynamic simulation. In *Proceedings of the Eurographics Computer Animation and Simulation Workshop in Poitiers, France*, pages 121–136, 1996.

S. McFaull and M. Lamontagne. In vivo measurement of the passive viscoelastic properties of the human knee joint. *Human Movement Science*, 17(2):139–165, 1998a.

S. R. McFaull and M. Lamontagne. In vivo measurement of the passive viscoelastic properties of the human knee joint. *Human Movement Science*, 17(2):139–165, 1998b.

J. McIntyre, F. Mussa-Ivaldi, and E. Bizzi. The control of stable postures in the multijoint arm. *Experimental Brain Research*, 110(2):248–264, 1996.

T. McMahon. *Muscles, reflexes, and locomotion*. Princeton Univ Pr, 1984.

P. McNair, E. Dombroski, D. Hewson, S. Stanley, et al. Stretching at the ankle joint: viscoelastic responses to holds and continuous passive motion. *Medicine and Science in Sports and Exercise*, 33(3):354–358, 2001.

P. McNair, D. Hewson, E. Dombroski, and S. Stanley. Stiffness and passive peak force changes at the ankle joint: the effect of different joint angular velocities. *Clinical Biomechanics*, 17(7): 536–540, 2002.

P. J. McNair and S. N. Stanley. Effect of passive stretching and jogging on the series elastic muscle stiffness and range of motion of the ankle joint. *British Journal of Sports Medicine*, 30(4):313–317, 1996.

G. Meyer, A. McCulloch, R. Lieber, et al. A nonlinear model of passive muscle viscosity. *Journal of Biomechanical Engineering*, 133(9):091007, 2011.

S. A. Migliore, E. A. Brown, and S. P. DeWeerth. Biologically inspired joint stiffness control. In *IEEE International Conference on Robotics and Automation*, pages 4508–4513. IEEE, 2005.

T. Milner and C. Cloutier. Damping of the wrist joint during voluntary movement. *Experimental Brain Research*, 122(3):309–317, 1998a.

T. Milner and D. Franklin. Characterization of multijoint finger stiffness: dependence on finger posture and force direction. *IEEE Transactions on Biomedical engineering*, 45(11):1363–1375, 1998a.

T. E. Milner and C. Cloutier. Damping of the wrist joint during voluntary movement. *Experimental Brain Research*, 122(3):309–317, September 1998b.

T. E. Milner and D. W. Franklin. Characterization of multijoint finger stiffness: dependence on finger posture and force direction. *Biomedical Engineering, IEEE Transactions on*, 45(11):1363–1375, 1998b.

A. Minami, K. An, W. Cooney III, R. Linscheid, and E. Chao. Ligamentous structures of the metacarpophalangeal joint: a quantitative anatomic study. *Journal of Orthopaedic Research*, 1 (4):361–368, 1983. ISSN 1554-527X.

A. Minami, K. An, C. WP, R. Linscheid, and E. Chao. Ligament stability of the metacarpophalangeal joint: a biomechanical study. *The Journal of Hand Surgery*, 10(2):255–260, 1985. ISSN 0363-5023.

B. Morrey and K. An. Articular and ligamentous contributions to the stability of the elbow joint. *The American Journal of Sports Medicine*, 11(5):315, 1983.

W. Murray, T. Buchanan, and S. Delp. Scaling of peak moment arms of elbow muscles with upper extremity bone dimensions. *Journal of Biomechanics*, 35(1):19–26, 2002.

R. P. D. D. A. Niehues, D. Taylor. Compliance in parallel to actuators for improving grasping and manipulation in robotic hands. *The International Journal of Robotics Research*, 2014.

A. Nimbarte, R. Kaz, and Z. Li. Finger joint motion generated by individual extrinsic muscles: A cadaveric study. *Journal of Orthopaedic Surgery and Research*, 3(1):1–5, 2008.

A. Nordez, P. McNair, P. Casari, and C. Cornu. Acute changes in hamstrings musculo-articular dissipative properties induced by cyclic and static stretching. *International Journal of Sports Medicine*, 29(5):414–418, 2008.

A. Nordez, P. Casari, J. Mariot, and C. Cornu. Modeling of the passive mechanical properties of the musculo-articular complex: Acute effects of cyclic and static stretching. *Journal of Biomechanics*, 42(6):767–773, 2009a.

A. Nordez, P. McNair, P. Casari, and C. Cornu. The effect of angular velocity and cycle on the dissipative properties of the knee during passive cyclic stretching: A matter of viscosity or solid friction. *Clinical Biomechanics*, 24(1):77–81, 2009b.

A. Nordez, P. McNair, P. Casari, and C. Cornu. Static and cyclic stretching: Their different effects on the passive torque–angle curve. *Journal of Science and Medicine in Sport*, 13(1):156–160, 2010.

C. Oatis. The use of a mechanical model to describe the stiffness and damping characteristics of the knee joint in healthy adults. *Physical Therapy*, 73(11):740, 1993.

C. A. Oatis, E. F. Wolff, M. A. Lockard, L. A. Michener, and S. J. Robbins. Correlations among measures of knee stiffness, gait performance and complaints in individuals with knee osteoarthritis. *Clinical Biomechanics*, 2013.

L. U. Odhner and A. M. Dollar. Dexterous manipulation with underactuated elastic hands. In *IEEE International Conference on Robotics and Automation*, pages 5254–5260. IEEE, 2011.

L. U. Odhner, L. P. Jentoft, M. R. Claffee, N. Corson, Y. Tenzer, R. R. Ma, M. Buehler, R. Kohout, R. D. Howe, and A. M. Dollar. A compliant, underactuated hand for robust manipulation. *The International Journal of Robotics Research*, 33(5):736–752, 2014.

P. Page. Current concepts in muscle stretching for exercise and rehabilitation. *International Journal of Sports Physical Therapy*, 7(1):109, 2012.

H. Palanthandalam-Madapusi, D. Bernstein, and A. Ridley. Space Weather Forecasting-Identifying periodically switching block-structured models to predict magnetic-field fluctuations. *IEEE Control Systems Magazine*, 27(5):109–123, 2007. ISSN 0272-1708.

A. Perotto and E. Delagi. *Anatomical guide for the electromyographer: the limbs and trunk*. Charles C Thomas Pub Ltd, 2005.

F. Petit and A. Albu-Schaffer. State feedback damping control for a multi dof variable stiffness robot arm. In *IEEE International Conference on Robotics and Automation*, pages 5561–5567. IEEE, 2011.

R. Pfeifer, M. Lungarella, and F. Iida. The challenges ahead for bio-inspired'soft'robotics. *Communications of the ACM*, 55(11):76–87, 2012.

M. Pradas and R. Calleja. Nonlinear viscoelastic behaviour of the flexor tendon of the human hand. *Journal of Biomechanics*, 23(8):773–781, 1990.

G. A. Pratt and M. M. Williamson. Series elastic actuators. In *Intelligent Robots and Systems 95.'Human Robot Interaction and Cooperative Robots', Proceedings. 1995 IEEE/RSJ International Conference on*, volume 1, pages 399–406. IEEE, 1995.

B. Prilutsky and V. Zatsiorsky. Tendon action of two-joint muscles: transfer of mechanical energy between joints during jumping, landing, and running. *Journal of Biomechanics*, 27(1):25–34, 1994.

U. Proske, D. Morgan, and J. Gregory. Thixotropy in skeletal muscle and in muscle spindles: a review. *Progress in Neurobiology*, 41(6):705, 1993.

P. Provenzano, R. Lakes, T. Keenan, and R. Vanderby. Nonlinear ligament viscoelasticity. *Annals of Biomedical Engineering*, 29(10):908–914, 2001.

P. Provenzano, R. Lakes, D. Corr, and R. Vanderby. Application of nonlinear viscoelastic models to describe ligament behavior. *Biomechanics and Modeling in Mechanobiology*, 1(1):45–57, 2002.

C. Pylatiuk, S. Mounier, A. Kargov, S. Schulz, and G. Bretthauer. Progress in the development of a multifunctional hand prosthesis. In *Engineering in Medicine and Biology Society, 2004. IEMBS'04. 26th Annual International Conference of the IEEE*, volume 2, pages 4260–4263. IEEE, 2004.

J. Qin, D. Lee, Z. Li, H. Chen, and J. Dennerlein. Estimating in vivo passive forces of the index finger muscles: Exploring model parameters. *Journal of Biomechanics*, 43(7):1358–1363, 2010.

D. Ranney, R. Wells, and J. Dowling. Lumbrical function: interaction of lumbrical contraction with the elasticity of the extrinsic finger muscles and its effect on metacarpophalangeal equilibrium. *The Journal of Hand Surgery*, 12(4):566, 1987.

R. Riener and T. Edrich. Identification of passive elastic joint moments in the lower extremities. *Journal of Biomechanics*, 32(5):539–544, 1999.

N. Rijnveld and H. Krebs. Passive wrist joint impedance in flexion - extension and abduction - adduction. In *Rehabilitation Robotics, 2007. ICORR 2007. IEEE 10th International Conference on*, pages 43–47, June 2007.

L. Ronnqvist and B. Rosblad. Kinematic analysis of unimanual reaching and grasping movements in children with hemiplegic cerebral palsy. *Clinical Biomechanics*, 22(2):165–175, 2007.

E. J. Rouse, R. D. Gregg, L. J. Hargrove, and J. W. Sensinger. The difference between stiffness and quasi-stiffness in the context of biomechanical modeling. *IEEE Transactions on Biomedical Engineering*, 60(2):562–568, 2013.

Y. Sakagami, R. Watanabe, C. Aoyama, S. Matsunaga, N. Higaki, and K. Fujimura. The intelligent asimo: System overview and integration. In *Intelligent Robots and Systems, 2002. IEEE/RSJ International Conference on*, volume 3, pages 2478–2483. IEEE, 2002.

J. Sancho-Bru, A. Perez-Gonzalez, M. Vergara-Monedero, and D. Giurintano. A 3-D dynamic model of human finger for studying free movements. *Journal of Biomechanics*, 34(11):1491–1500, 2001. ISSN 0021-9290.

A. Schepelmann, K. A. Geberth, and H. Geyer. Compact nonlinear springs with user defined torque-deflection profiles for series elastic actuators. *IEEE International Conference on Robotics and Automation*, 2014.

M. Schmidt and H. Lipson. Distilling free-form natural laws from experimental data. *Science*, 324 (5923):81–85, 2009.

L. Schutte. *Using musculoskeletal models to explore strategies for improving performance in electrical stimulation-induced leg cycle ergometry*. PhD thesis, Stanford University, CA, 1992.

R. Shadmehr and M. Arbib. A mathematical analysis of the force-stiffness characteristics of muscles in control of a single joint system. *Biological Cybernetics*, 66(6):463–477, 1992.

N. Shrivastava, M. Koff, A. Abbot, V. Mow, M. Rosenwasser, and R. Strauch. Simulated extension osteotomy of the thumb metacarpal reduces carpometacarpal joint laxity in lateral pinch1. *The Journal of Hand Surgery*, 28(5):733–738, 2003. ISSN 0363-5023.

A. Silder, B. Whittington, B. Heiderscheit, and D. Thelen. Identification of passive elastic joint moment-angle relationships in the lower extremity. *Journal of Biomechanics*, 40(12):2628–2635, 2007. ISSN 0021-9290.

G. L. Soderberg and Soderberg. *Kinesiology: application to pathological motion*. Williams & Wilkins Baltimore, MD, 1986.

P. L. Srinivasa, S. Nagananda, G. R. Kadambi, R. Hariharan, P. Shankpal, and S. Shankapal. Development of two degree of freedom (dof) bionic hand for below elbow amputee. In *Electronics, Computing and Communication Technologies (CONECCT), 2013 IEEE International Conference on*, pages 1–6. IEEE, 2013.

S. Sueda, A. Kaufman, and D. Pai. Musculotendon simulation for hand animation. *ACM Transactions on Graphics (TOG)*, 27(3):83, 2008.

K. Suzumori. Elastic materials producing compliant robots. *Robotics and Autonomous Systems*, 18 (1):135–140, 1996.

K. Tamai, J. Ryu, K. An, R. Linscheid, W. Cooney, and E. Chao. Three-dimensional geometric analysis of the metacarpophalangeal joint. *The Journal of Hand Surgery*, 13(4):521–529, 1988. ISSN 0363-5023.

D. C. Taylor, J. D. Dalton, A. V. Seaber, W. E. Garrett, et al. Viscoelastic properties of muscle-tendon units the biomechanical effects of stretching. *The American Journal of Sports Medicine*, 18(3):300–309, 1990.

F. J. Thompson, C. R. Browd, P. M. Carvalho, and J. Hsiao. Velocity-dependent ankle torque in the normal rat. *Neuroreport*, 7(14):2273–2276, 1996.

M. Tian, P. Hoang, S. Gandevia, L. Bilston, and R. Herbert. Stress relaxation of human ankles is only minimally affected by knee and ankle angle. *Journal of Biomechanics*, 43(5):990–993, 2010.

M. Tian, P. Hoang, S. Gandevia, R. Herbert, and L. Bilston. Viscous elements have little impact on measured passive length–tension properties of human gastrocnemius muscle–tendon units¡ i¿ in vivo¡/i¿. *Journal of Biomechanics*, 44(7):1334–1339, 2011.

E. Todorov and Z. Ghahramani. Analysis of the synergies underlying complex hand manipulation. In *Engineering in Medicine and Biology Society, 2004. IEMBS'04. 26th Annual International Conference of the IEEE*, volume 2, pages 4637–4640. IEEE, 2004.

N. Tsagarakis, M. Laffranchi, B. Vanderborght, and D. Caldwell. A compact soft actuator unit for small scale human friendly robots. In *IEEE International Conference on Robotics and Automation*, pages 4356–4362. IEEE, 2009.

L.-W. Tsai. Design of tendon-driven manipulators. *Journal of Vibration and Acoustics*, 117(B): 80–86, 1995.

A. Unsworth, P. Yung, and I. Haslock. Measurement of stiffness in the metacarpophalangeal joint: the arthrograph. *Clinical Physics and Physiological Measurement*, 3:273–281, 1982.

F. Valero-Cuevas, F. Zajac, and C. Burgar. Large index-fingertip forces are produced by subject-independent patterns of muscle excitation. *Journal of Biomechanics*, 31(8):693–704, 1998.

F. J. Valero-Cuevas, H. Hoffmann, M. U. Kurse, J. J. Kutch, and E. A. Theodorou. Computational models for neuromuscular function. *Biomedical Engineering, IEEE Reviews in*, 2:110–135, 2009.

A. Van den Bogert, K. Gerritsen, and G. Cole. Human muscle modelling from a user's perspective. *Journal of Electromyography and Kinesiology*, 8(2):119–124, 1998.

G. Venture, Y. Nakamura, K. Yamane, and M. Hirashima. A painless and constraint-free method to estimate viscoelastic passive dynamics of limbs joints to support diagnosis of neuromuscular diseases. In *Engineering in Medicine and Biology Society, 2007. EMBS 2007. 29th Annual International Conference of the IEEE*, pages 5362–5365, 2007.

L. Vigouroux, F. Quaine, A. Labarre-Vila, and F. Moutet. Estimation of finger muscle tendon tensions and pulley forces during specific sport-climbing grip techniques. *Journal of Biomechanics*, 39(14):2583–2592, 2006.

M. Vrahas, R. Brand, T. Brown, and J. Andrews. Contribution of passive tissues to the intersegmental moments at the hip. *Journal of Biomechanics*, 23(4):357–362, 1990. ISSN 0021-9290.

M. Weghe, M. Rogers, M. Weissert, and Y. Matsuoka. The ACT hand: design of the skeletal structure. In *Proceedings of the 2004 IEEE International Conference on Robotics and Automation*. IEEE, 2004.

D. Werner, S. Kozin, M. Brozovich, S. Porter, D. Junkin, and S. Seigler. The biomechanical properties of the finger metacarpophalangeal joints to varus and valgus stress1. *The Journal of Hand Surgery*, 28(6):1044–1051, 2003.

T. Wickiewicz, R. Roy, P. Powell, V. Edgerton, et al. Muscle architecture of the human lower limb. *Clinical orthopaedics and related research*, (179):275, 1983.

D. Wilkinson, M. Weghe, and Y. Matsuoka. An extensor mechanism for an anatomical robotic hand. In *IEEE International Conference on Robotics and Automation*, volume 1, pages 238–243. IEEE, 2003.

D. Winter. *Biomechanics and motor control of human movement*. Wiley, 2009. ISBN 0470398183.

S. Wolf and G. Hirzinger. A new variable stiffness design: Matching requirements of the next robot generation. In *IEEE International Conference on Robotics and Automation*, pages 1741–1746. IEEE, 2008.

S. Wolf, O. Eiberger, and G. Hirzinger. The dlr fsj: Energy based design of a variable stiffness joint. In *IEEE International Conference on Robotics and Automation*, pages 5082–5089. IEEE, 2011.

V. Wright and R. J. Johns. Quantitative and qualitative analysis of joint stiffness in normal subjects and in patients with connective tissue diseases. *Annals of the rheumatic diseases*, 20(1):36, 1961.

C.-h. Wu, J. C. Houk, K.-Y. Young, and L. E. Miller. Nonlinear damping of limb motion. *Multiple Muscle Systems*, pages 214–235, 1990.

J. Wu, K. An, R. Cutlip, K. Krajnak, D. Welcome, and R. Dong. Analysis of musculoskeletal loading in an index finger during tapping. *Journal of Biomechanics*, 41(3):668–676, 2008. ISSN 0021-9290.

Y.-N. Wu, B. Hyland, and J.-J. Chen. Biomechanical and electromyogram characterization of neuroleptic-induced rigidity in the rat. *Neuroscience*, 147(1):183–196, 2007.

Z. Xu, E. Todorov, B. Dellon, and Y. Matsuoka. Design and analysis of an artificial finger joint for anthropomorphic robotic hands. In *IEEE International Conference on Robotics and Automation*, pages 5096–5102. IEEE, 2011.

Z. Xu, V. Kumar, Y. Matsuoka, and E. Todorov. Design of an anthropomorphic robotic finger system with biomimetic artificial joints. In *IEEE RAS & EMBS International Conference on Biomedical Robotics and Biomechatronics*, pages 568–574. IEEE, 2012.

D. Yao. High-resolution EEG mapping: a radial-basis function based approach to the scalp Laplacian estimate. *Clinical Neurophysiology*, 113(6):956–967, 2002. ISSN 1388-2457.

F. Zajac. Muscle and tendon: properties, models, scaling, and application to biomechanics and motor control. *Critical Reviews in Biomedical Engineering*, 17(4):359, 1989.

F. Zajac, R. Neptune, and S. Kautz. Biomechanics and muscle coordination of human walking: Part i: Introduction to concepts, power transfer, dynamics and simulations. *Gait & posture*, 16 (3):215–232, 2002.

F. Zajac, R. Neptune, and S. Kautz. Biomechanics and muscle coordination of human walking:: Part ii: Lessons from dynamical simulations and clinical implications. *Gait & posture*, 17(1): 1–17, 2003.

V. Zatsiorsky. Kinematics of human movement. *Champaign, IL: Human Kinetics*, 1998.

V. M. Zatsiorsky. On muscle and joint viscosity. *Motor Control*, 1:299–309, 1997.

L. Zhang, G. Portland, G. Wang, C. Diraimondo, G. Nuber, M. Bowen, and R. Hendrix. Stiffness, viscosity, and upper-limb inertia about the glenohumeral abduction axis. *Journal of Orthopaedic Research*, 18(1):94–100, 2000.

W. G. Z. C. S. L. Zhang, L. Q. and W. Z. Rymer. Passive and active mechanical properties of the human knee joint in abduction-adduction. In *19th International Conference - IEEE/EMBS*, 1997.

Vita

Pei-Hsin Kuo received his Bachelor of science degree in Applied Physics from the TamKang University in Taipei, 2000. He received his first Master degree in Sport Science from the University of Taipei in 2003. He served as a Sports Biomechanical Analysist at the National Sports Training Center in Kaohsiung, Taiwan from 2003 to 2006. He decided to pursue his second Master degree in USA in 2006, and he received the degree in Mechanical Engineering from the University of Maine, Orono, in 2008. He enrolled into the PhD program in the following year, 2009. He transferred from the University of Maine to join the Department of Mechanical Engineering at The University of Texas at Austin in 2011. He has been serving as a research assistance in the ReNue Robotics Lab since 2011.

Permanent address: peihsin.kuo.me@gmail.com

This dissertation was typeset with LaTeX[†] by the author.

[†]LaTeX is a document preparation system developed by Leslie Lamport as a special version of Donald Knuth's TeX Program.